INTERACTIONS OF GALACTIC COSMIC RAYS WITH THE LUNAR SURFACE

A DISSERTATION SUBMITTED TO THE GRADUATE DIVISION OF THE UNIVERSITY OF HAWAIʻI AT MĀNOA IN PARTIAL FULFILLMENT OF THE REQUIREMENTS FOR THE DEGREE OF

DOCTOR OF PHILOSOPHY

IN

GEOLOGY AND GEOPHYSICS

MAY 2014

By

Sarah Tinney Crites

Dissertation Committee:

Paul G. Lucey, Chairperson
Peter A.J. Englert
Jeffrey J. Gillis-Davis
G. Jeffrey Taylor
Sven E. Vahsen

Keywords: Moon; Astrobiology; Cosmic rays; Remote sensing; Spectroscopy; Lunar highlands

ACKNOWLEDGEMENTS

I thank Paul Lucey, who has been a stellar advisor and mentor throughout my PhD, for always being ready with advice, knowledge, and assistance when needed, but also knowing when to step back and let me tackle a problem alone. Peter Englert was the first to introduce me to planetary neutron and gamma ray spectroscopy and the remote sensing class he co-taught with Paul can be credited with initiating my first dissertation project. David Lawrence taught me to use MCNPX and opened up the field of planetary radiation modeling and neutron and gamma ray analysis to me, and Eric Pilger and Ethan Kastner's assistance in using the HIGP cluster as well as general computer expertise permitted me to complete my third project in a reasonable amount of time. I thank Jeff Taylor for always being available to share some of his vast knowledge about the Moon with me. Jeff's sense of humor and Paul's kept my dissertation work from ever becoming drudgery. Mark Wood, Taylor Viti, Jessica Norman, and Lance Yoneshige provided engineering and technical assistance with side projects that permitted me to pursue these outside research interests while continuing to make progress on my dissertation work. The Fred M. Bullard Graduate Fellowship provided funding for me to work on one of these side projects that enriched my grad school experience. I thank Rob Wright for giving me the opportunity to spend some of my time working on the SUCHI instrument while I completed my dissertation, and Harold Garbeil, Keith Horton, and HSFL, especially Amber Imai and Jeremy Chan for informative conversations and interesting lab experiences working on that project. I thank Leona Anthony, Vi Nakahara, Grace Furuya, Rena Lefevre, and Susan Vangorder for their administrative support, without which this project could not have been accomplished. I thank Katie Robinson for many helpful conversation s about lunar samples and Myriam Lemelin and David Trang for informative discussions about lunar remote sensing. I am indebted to all of the G&G graduate students for their social and moral support. I thank my family: my dad, without whose advice, encouragement, and unique worldview I would not have ended up where I am; my mom for her constant, unconditional love and support; my sister Abigail for keeping me sane in grad school more than any other person, and for always being available to talk no matter the time difference; and Brian Boston for promising to love me even if I failed comps and being here for me every day since.

ABSTRACT

This dissertation is focused on improving understanding of the composition and structure of the Moon's crust and the processes that have affected it over its history. This is accomplished through integrating remote sensing datasets with models of modifying processes such as basin-forming impacts and galactic cosmic ray radiation. I focus on two areas of active study for the Moon: the nature of the mafic component of the highlands crust, and the unique nature of the Moon's polar regions. The first part of this dissertation integrates three remote sensing data sets: 1) mineral maps derived from ultraviolet-visible spectroscopy from the Clementine mission, 2) neutron counts from the lunar surface from the Lunar Prospector neutron spectrometer, and 3) elemental abundances from the Lunar Prospector gamma ray spectrometer. Systematic discrepancies between the three datasets are identified and resolved, resulting in new abundance maps of the major lunar minerals (olivine, clinopyroxene, orthopyroxene, plagioclase, and ilmenite) and an associated map of magnesium number for the mafic minerals. The second part of this dissertation employs the new mineral maps as constraints on mixing models. The mixing models assess contributions to the current lunar highlands crust of primary magma ocean anorthosites, later igneous products, and ultramafic mantle material excavated by large basins. We conclude that the magma ocean likely did not predominately produce anorthosites containing 15 vol% mafic minerals, and that the combined contribution to the highlands crust of ultramafic mantle material excavated by large basins and post-magma ocean igneous activity is between 15 and 45 vol%. The mixing models also support the conclusion of Weiczorek and Phillips (1999) that the excavation cavities of the largest lunar basins had depth-to-diameter ratios

shallower than 1/10 (ratios between 0.03 and 0.07 are consistent with our mixing models). The final part of this dissertation uses the radiation transport code MCNPX 2.6.0 to model the radiation dose from galactic cosmic rays absorbed at different depths in the lunar regolith. We conclude that if simple ices are present in polar cold traps, they could have accumulated radiation doses equivalent to those used in experiments to stimulate synthesis of complex organic species.

TABLE OF CONTENTS

LIST OF TABLES

LIST OF FIGURES

LIST OF ABBREVIATIONS AND VARIABLES

Abbreviation/Variable	Definition
A_i	atomic mass
An#	molar Ca/(Ca+Na)
BESS	Balloon-borne Experiment with Superconducting Spectrometer
Cpx	clinopyroxene
CRaTER	Cosmic Ray Telescope for the Effects of Radiation
D_{tc}	transient crater diameter
eV	electron volt
FAN	ferroan anorthosite
f_{epi}	epithermal neutron flux
f_i	weight fraction
$f_{thermal}$	thermal neutron flux
GCR	galactic cosmic ray
Gy	gray, 1 gray=1 joule/kilogram
H Lyα	Lyman-alpha spectral line of hydrogen
H_{exc}	crater excavation depth
LCROSS	Lunar Crater Observation and Sensing Satellite
LMO	lunar magma ocean
LP GRS	Lunar Prospector gamma ray spectrometer

LP NS	Lunar Prospector neutron spectrometer
MCNPX	Monte Carlo N-particle eXtended
MESSENGER	MErcury Surface Space ENvironment GEochemistry and Ranging
Mg#	molar MgO/(MgO+FeO)
N_A	Avogadro's number, $6.0221413*10^{23}$
Ol	olivine
Opx	orthopyroxene
ϕ	solar modulation parameter
PAN	"purest anorthosite" containing <2 vol% mafic minerals
Plag	plagioclase
POI	post-magma ocean igneous material
R_i	radius of the sphere representing the crater excavation cavity
R_{mantle}	radius of the lunar mantle
R_{moon}	radius of the Moon
RSICC	Radiation Safety Information Computational Center
σ	standard deviation
Σ_{eff}	macroscopic neutron absorption cross section
σ_i	thermal neutron absorption cross section
SPA	South Pole-Aitken basin

UVVIS	ultraviolet-visible
vol%	volume percent

CHAPTER 1

INTRODUCTION

1.1 Why study the Moon?

The Moon, as an airless body that is not currently geologically active and does not possess a strong a magnetic field, preserves the record of events in the early solar system and provides an analog for ongoing surface processes taking place on airless bodies throughout the solar system. The study of the Moon's surface provides insight into the bombardment history of the early solar system, planetary differentiation and magma ocean crystallization, surface modification processes like regolith formation and space weathering, cold trapping of volatile species in permanently shadowed polar regions, and many other processes. As Earth's nearest neighbor, the Moon provides a relatively accessible natural laboratory to study these processes: it has been visited by a dozen orbiters since 1990, as well as numerous prior orbiting, landed, and roving missions, resulting in a wealth of data that can be used to study its surface and history. It is also the only planetary body other than Earth visited by humans, and the only body for which samples, returned from known locations by the manned Apollo and unmanned Luna missions, can be used to calibrate and validate orbital remote sensing datasets. In this dissertation we leverage the unique datasets available at the Moon to examine its early petrologic history and ongoing surface modification processes that can also shed light on analog surfaces throughout the solar system.

1.2 The lunar highlands

The presence of anorthosite fragments in the first Apollo samples prompted the lunar magma ocean hypothesis which provides a framework for the story of the Moon's early history. In this hypothesis, the early Moon was at least partially molten, and fractional crystallization of the melt led to buoyant plagioclase rising to form the Moon's primary anorthositic highlands crust (e.g. Smith et al. 1970; Wood et al. 1970; Warren and Wasson 1977; Warren 1985; Snyder et al. 1992). The purity of this anorthositic crust has been debated (e.g. Warren, 1990), but recent remote spectral identification of extremely pure anorthosite (<2-3 vol% mafic minerals) (Ohtake et al., 2009; Pieters et al.,

2009a; Cheek et al. 2013) by the Chandrayaan-1 Moon Mineralogy Mapper (M3) and the Kaguya Multiband Imager (MI) and Spectral Profiler (SP) lend support to arguments for a magma ocean that concentrated plagioclase to a high degree. Since the initial formation of the anorthositic primary crust between 4.47 and 4.29 billion years ago (Carlson and Lugmair, 1988; Borg et al. 1999, 2011), it has been modified to by extrusive volcanism and igneous intrusions (e.g. Ryder and Spudis 1980) and has had its surface turned over, modified, and redistributed by impacts at all scales from the 2000-km South Pole Aitken basin to the micrometeorites that still churn the Moon's surface today (e.g. Petro and Pieters 2004).

The most obvious occurrences of post-magma ocean igneous activity are the nearside maria, which range in age from ~4 Gyr to 1.2 Gyr and cover about 17% of the Moon's surface (Head and Wilson, 1992; Hiesinger et al. 2011). However, the Moon's volcanic history was not limited to these nearside extrusive eruptions. Numerous ancient mare deposits known as cryptomaria because they are largely hidden beneath the ejecta blankets of later impacts have been identified in places where impact craters penetrate the overlying highland material to excavate basalt (e.g Schultz and Spudis 1979; Hawke and Bell, 1981; Antonenko et al., 1995). Evidence for ancient volcanism can be found in samples as well: the Apollo collection includes clasts of basalts as old as 3.9-4 Gyr (Ryder and Spudis, 1980), and basaltic clasts in the lunar meteorite Kalahari 009 have radiometric U-Pb ages as old as 4.35 Gyr, revealing that basaltic volcanism began taking place before the end of basin formation (Terada et al., 2007).

The magnesian suite, or Mg-suite, of pristine nonmare rocks in the Apollo collection consists of dunites, gabbroic anorthosites, spinel troctolites, troctolites, and norites that are thought to have formed in moderate-sized plutonic intrusions into the lunar highlands (James and Flohr, 1983) and may be related to overturn of the lunar mantle as a result of density instability caused by magma ocean crystallization (e.g. Ryder, 1991, Jolliff et al. 2000). The Mg-suite rocks have ages ranging from about 4.44 Gyr to about 4.2 Gyr (Taylor and McClennan, 2009) and represent the earliest known post-magma ocean igneous activity. Remote sensing and the sample record confirm that the Moon has a long and varied igneous history; however, deciphering the extent and

variety of ancient lunar volcanism and igneous intrusion is complicated by the intense cratering experienced by the Moon, and much of the surficial and sample evidence for very early volcanism was likely destroyed by the very high impact flux at that time in the Moon's history (e.g. Ryder and Spudis, 1980; Hiesinger et al. 2011).

Impact craters and the products of the cratering process dominate the visible geologic features of the Moon at all scales (e.g. Melosh, 1989). The bombardment of the lunar surface by impactors of all sizes contributed to a large amount of vertical and lateral mixing of crustal material (e.g. Petro and Pieters 2004, 2008). Planetary impacts and subsequent surface modification processes have been intensely studied through theory, models, experiments, and observations (e.g. Stöffler et al. 1975; Gault et al. 1978; Croft, 1980; O'Keefe and Ahrens 1993; Melosh, 1989). However, many questions still remain, particularly with respect to how large basin formation on the Moon affected the composition of the crust through excavation of mafic lower crust or mantle material. 43 large and ancient basins (craters larger than 300 km) are identified in gravity and topography measurements (Wilhelms, 1987; Spudis, 1993; Neumann et al. 1996, 2013). If these basins adhere to the same excavation process that is well understood for smaller craters (Croft, 1980; Housen et al. 1983; Melosh, 1989), and excavated material from a depth equal to 1/10 their transient cavity diameter, many would have penetrated the lunar mantle (e.g. Spudis 1993; Wieczorek and Phillips 1999), and the highlands surface we view today would contain at least a small mantle component in addition to primary anorthositic crustal material and the products of later igneous activity. However, from a remote sensing standpoint there is still some question whether even the 2600-km diameter South Pole-Aitken basin shows evidence of having excavated the lunar mantle (e.g. Pieters et al. 1997; Lucey et al. 1998; Wieczorek and Phillips 1999; Yamamoto et al. 2010).

Chapters Two and Three of this dissertation are focused on improving our understanding of the lunar highlands crust and the processes that have affected it throughout the Moon's history. In Chapter Two we integrate three global remote sensing datasets, leveraging their complementary nature, to create a robust set of global maps of the major lunar minerals (olivine, orthopyroxene, clinopyroxene, plagioclase, and

ilmenite) and the magnesium number of the mafic minerals. These major minerals are tracers for the rocks they make up on the lunar surface, so in Chapter Three we use our mineral maps as constraints on two and three component mixing models of lunar rock types representing three sources of highlands crust material: primary magma ocean anorthosites, post-magma ocean igneous rocks, and ultramafic mantle material excavated by large basins. These mixing models give ranges for the relative abundances of these three components of the highlands crust, and provide constraints on the excavation conditions of the largest lunar basins that would have excavated mantle material. This insight into the nature of magma ocean products, amount of igneous activity, and the excavation conditions of basin-sized impacts is also relevant to bodies beyond the Moon that may have had magma oceans and that experienced impact bombardment, including some asteroids and Mars.

1.3 The poles of the Moon

The near-perpendicularity of the Moon's spin axis relative to the plane of the ecliptic creates a unique environment at the lunar poles. Because sunlight arriving at the poles is glancing, some topographic lows such as crater floors are never lit. This orbital geometry was first described by Urey (1952), who realized that the Moon's vacuum environment would allow these permanently shadowed regions to reach temperatures cold enough to condense and retain volatiles. Watson et al (1961), followed by Arnold (1979), created models of volatile trapping in these regions. In the 1990s modeling of the permanently shadowed regions of the Moon was revisited (Ingersoll et al., 1992; Salvail and Fanale, 1994; Vasavada et al., 1999), and these models predicted temperatures as cold as 50 K in the Moon's polar regions. In 2010 the Diviner Lunar Radiometer confirmed the extremely cold nature of the Moon's poles with measurements of some polar cold traps reaching temperatures as cold as 29 K, cold enough to trap water ice as well as many other volatile species such as SO_2, CH_3OH, NH_4, and CO_2 (Vasavada et al. 1999; Paige et al. 2010).

The first observational evidence indicating the possible presence of water ice at the poles was obtained when the Clementine Bistatic Radar Experiment detected radar return enhancement consistent with the presence of a low-loss volume scatterer like water

ice at the Moon's south pole (Nozette et al. 1996). Further evidence for water ice at the poles of the Moon came from Lunar Prospector, which carried a neutron spectrometer to measure counts of neutrons produced in the lunar surface as a result of galactic cosmic-ray spallation. Because neutrons and the protons that make up hydrogen atoms carry the same mass and thus exchange energy efficiently, a hydrogen-enriched material (such as water ice) creates a distinctive signature of decreased counts of neutrons of moderate energy compared to those with low energy. The Lunar Prospector neutron spectrometer detected this signature, consistent with 200 ppm to 40 wt% H_2O ice in permanently shadowed regions (Feldman et al. 1998; Lawrence et al. 2006), and the LEND neutron spectrometer onboard the Lunar Reconnaissance Orbiter has confirmed the Lunar Prospector hydrogen detection (Mitrofanov et al. 2010). Evidence for the possible presence of water ice in polar permanently shadowed regions has also been reported on the basis of reflectance measurements by the Lunar Orbiter Laser Altimeter (Zuber et al. 2012), anomalous radar signatures in permanently shadowed craters (Spudis et al. 2010), and a 3-micron absorption feature consistent with OH or H_2O that is strongest at high latitudes measured by the Moon Mineralogy Mapper (Pieters et al. 2009b).

Although the search for water ice has been the focus of most lunar polar science investigations, thermal modeling (e.g. Vasavada et al. 1999; Zhang and Paige, 2009; Paige et al. 2010) indicates that a variety of other volatile species including organics could be present. The 2010 LCROSS mission measured the composition of material in a polar cold trap at closer range by directing the impact of the spent Centaur stage of the Lunar Reconnaissance Orbiter's rocket into Cabeus crater The impactor was followed by a shepherding spacecraft equipped with spectrometers to measure the ejecta plume created (Schultz et al. 2010). LCROSS detected water ice as well as several other volatile species including CO_2, CH_4, and CH_3OH in this crater (Colaprete et al. 2010). The detection of a variety of simple compounds used as inputs to experiments that produce complex organics from them through radiation processing (e.g. e.g. Moore et al., 1983, 2001; Delitsky and Thompson, 1987; Johnson, 1989; Delitsky and Lane, 1997; Moore and Hudson, 1998, 2003; Hudson and Moore, 1999; Gerakines et al., 2001) raises the possibility that synthesis of complex organics could be taking place at the Moon's poles.

Recent measurements at Mercury have brought the question of in-situ organic production to the forefront of the study of polar cold traps. The MESSENGER neutron spectrometer observed a strong decrease in epithermal neutron flux at the poles of Mercury, consistent with thick layers of nearly pure water ice (Lawrence et al. 2013). Reflectance measurements of Mercury's permanently shadowed regions by the Mercury Laser Altimeter revealed that while some cold traps show a bright signature consistent with exposed water ice, others are covered with a dark surface deposit that thermal modeling suggests may be composed of complex organics produced by in-situ processing (Neumann et al. 2013; Paige et al. 2013).

The last two decades of direct and indirect measurements of the Moon's polar regions have overturned the Apollo-era paradigm of a bone-dry Moon. Temperature modeling and measurements (Ingersoll et al., 1992; Salvail and Fanale, 1994; Vasavada et al., 1999; Paige et al. 2010) tell us that water ice and other volatiles should be stable at the surface in some areas of the Moon's poles, with potential for much greater abundance of volatiles sequestered in the shallow subsurface. Observations from many different instruments indicate that volatiles, particularly water, are being trapped at the Moon's poles (e.g. Nozette et al. 1996; Feldman et al. 1998; Colaprete et al. 2010; Mitrofanov et al. 2010; Pieter et al. 2009). However, the abundance and distribution of water ice, and the type and source of other volatiles, is still an area of active investigation. The results of these studies have relevance beyond the Earth-Moon system: the Moon's poles are an analog environment for other ice-bearing airless bodies in the solar system including main belt comets, Mercury, and outer solar system moons and comets. The Moon provides us with a relatively close-by natural laboratory to study processes of volatile trapping, sequestration, and in-situ modification that may be taking place on many bodies throughout the solar system. In Chapter 4 of this dissertation we describe our study of the radiation environment at the poles of the Moon using the radiation transport code MCNPX 2.6.0 and discuss implications for the possibility of in-situ organic synthesis at the Moon and Mercury.

CHAPTER 2

REVISED MINERAL MAPS OF THE MOON FROM INTEGRATING RESULTS FROM THE LUNAR PROSPECTOR NEUTRON AND GAMMA RAY SPECTROMETERS WITH CLEMENTINE SPECTROSCOPY

In review for publication in *American Mineralogist* as Crites, S.T. and Lucey, P.G., Revised mineral maps of the Moon from integrating results from the Lunar Prospector neutron and gamma ray spectrometers with Clementine spectroscopy.

Abstract—Mineralogical measurements from spectral remote sensing and remote geochemical measurements from gamma ray and neutron spectrometers are complementary datasets that have been used together successfully to study the distributions of iron, titanium, and rare earth elements on the Moon. We compared neutron and gamma ray datasets from Lunar Prospector and found them in good agreement with each other within the errors of previously developed equations to relate neutron flux with geochemistry, but find small adjustments to the nominal values are warranted. We used the neutron-validated LP GRS oxides to improve Clementine-based global mineral maps. The comparison was enabled by converting the minerals of Lucey (2004) to oxides using stoichiometry and assumptions about Mg#, calcium content of clinopyroxenes, and An#. We found that FeO and Al_2O_3 derived from the maps of Lucey (2004) did not follow the expected negative correlation seen in lunar samples, but could be brought into agreement with samples and with LP GRS oxides by increasing plagioclase in proportion with orthopyroxene abundance, while simultaneously decreasing Mg#. We interpreted this to mean that plagioclase and orthopyroxene exist in rocks together (as in a norite) with the spectrally difficult to detect plagioclase being masked by the strong spectral signature of the orthopyroxene. We generated a revised set of maps of the major lunar minerals and a map of Mg# for the mafic minerals that are consistent with Lunar Prospector neutron and gamma ray spectrometer results and show greatly improved agreement with lunar soil samples over previous global mineral maps from Clementine.

2.1 Introduction

Visible and near-infrared spectroscopy of the Moon provides a tool that is sensitive to both the mineralogy and the mineral chemistry of the major lunar rocks. Minerals revealed through spectroscopy constrain the spatial distribution of rock types that make up the Moon, with the high-calcium pyroxene-rich maria distinct from the plagioclase-rich highlands (e.g. McCord et al. 1981). Spectrally derived mineralogy can play an important role in deciphering the history and evolution of the Moon. For example, the "purest anorthosite" (PAN) detections of Ohtake et al. (2009) and Pieters et al. (2009a) with <2 vol% mafic minerals showed that the lunar magma ocean must have concentrated plagioclase to a high degree in many locations across the Moon. Orbital neutron and gamma-ray measurements (e.g. Feldman et al. 1993) can be compared with spectrally-derived mineralogy using relatively few assumptions to draw robust conclusions about lunar surface mineralogy.

Lucey (2004) produced global maps for the major lunar minerals olivine, orthopyroxene, clinopyroxene, and plagioclase from the Clementine mission's spectral reflectance measurements. However, these maps were not validated against other data sets or by comparison with lunar samples. The Lunar Prospector mission (Binder, 1998) followed Clementine with a gamma-ray spectrometer (GRS) that directly measured elemental abundance (Prettyman et al. 2006) and a neutron spectrometer (NS) to provide a measurement of the weighted sum of the components present in the surface (e.g. Feldman et al., 2000). The Lunar Prospector measurements are independently sensitive to composition, so we perform a direct comparison, achieved through modeling and empirical relationships, to improve understanding of uncertainties in both measurements. We then compare the self-consistent Lunar Prospector datasets against mineral maps from spectral reflectance using simple stoichiometry. We use independent and complementary measurements by the Lunar Prospector neutron and gamma-ray spectrometers to validate and improve the mineral maps, using lunar sample compositional trends as an additional constraint.

2.2 Methods

2.2.1 Lunar Prospector neutron and gamma ray spectrometer reconciliation

The Lunar Prospector mission carried a gamma ray spectrometer and a neutron spectrometer to study the composition of the lunar surface (Feldman et al., 1999). The gamma-ray spectrometer measured gamma rays emitted from the lunar surface as a result of cosmic ray interaction with the major elements or radioactive decay of K, Th, and U. It also measured fast neutrons (E > 500 keV) using its anticoincidence shield (Feldman et al., 1999). The neutron spectrometer measured neutrons created as by-products of cosmic ray bombardment of the lunar surface and moderated to the thermal (E < 0.4 eV) and epithermal (0.4 eV < E < 500 keV) energy ranges. These datasets can be used to validate and improve spectral mineral maps, but for greater robustness we first examined the consistency of the gamma ray and neutron data with each other.

2.2.1.1 Fast neutron and gamma ray reconciliation

Gasnault et al. (2001) determined through modeling of neutron production, transport, and leakage, as well as comparisons to laboratory experiments, a linear relationship between fast neutron leakage flux and the average atomic mass of the constituents of the material producing neutrons. This equation is given by (1), where $\langle A \rangle$ is the average atomic mass in units of amu (atomic mass units), and C is the fast neutron leakage flux in counts (neutrons per second).

$$\langle A \rangle = eC + f$$

$$e = (26 \pm 6) \times 10^{-3}$$

$$f = (11 \pm 3)$$

(1) (Gasnault et al., 2001)

Fast neutron flux can be estimated using the oxides measured by the LP GRS and equation 1. This can then be compared with the measured fast neutron flux. We compared the distribution of fast neutron flux for the Moon, calculated from LP GRS average atomic mass, and measured fast neutron flux, both binned to 2 degree pixels,

shown in Figure 2.1a. The distribution falls off the plotted 1:1 line, with the measured fast neutron flux systematically higher than that estimated from the gamma ray spectrometer data and equation 1. We applied a simple adjustment of the parameters *e* and *f* within their stated errors to minimize the differences between the two datasets and this resulted in an improved fit (Fig. 2.1b) when $e = 25.6 * 10^{-3}$ and $f = 10.6$.

Table 2.1. Thermal neutron absorption cross sections for the major lunar elements and Sm and Gd

Note: [a]The neutron absorption cross sections for isotopes of Sm and Gd vary widely. The values given are the neutron absorption cross sections of the most highly absorbing isotopes; absorption for other isotopes are generally below 1 (NNDC, accessed Dec. 2010).

Element	Thermal neutron absorption cross section (barns)
O	0.00019
Na	0.528
Mg	0.063
Al	0.233
Si	0.16
Ca	0.43
Ti	6.11
Fe	2.59
Sm[a]	56000
Gd[a]	90000

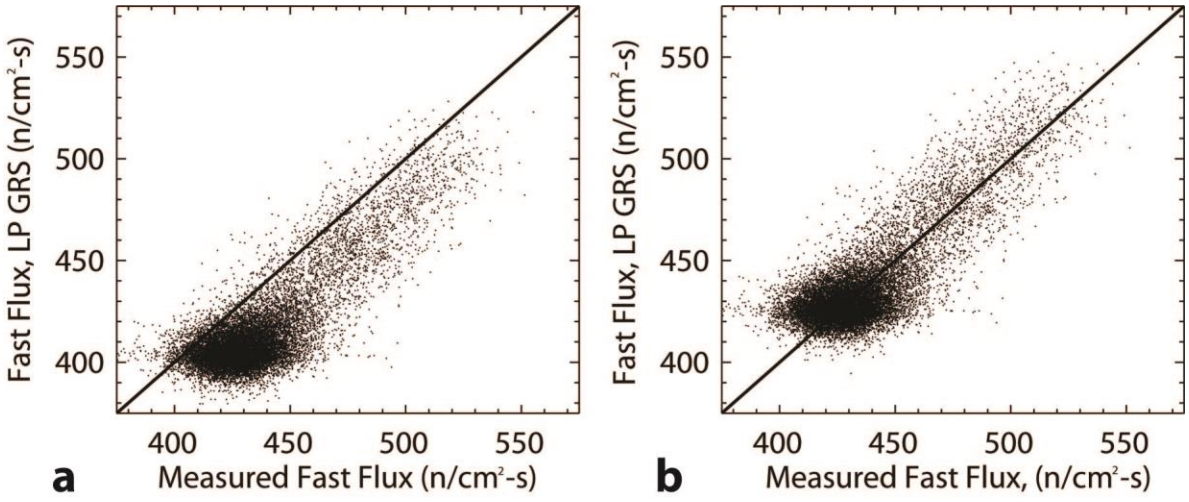

Figure 2.1a): Fast neutron flux calculated from the LP GRS oxides using equation 1 plotted against measured fast neutron flux from the LP NS. **2.1b):** Fast neutron flux calculated from the LP GRS oxides and equation 1 with e = $25.6 * 10^{-3}$ and f = 10.6 compared with the measured fast neutron flux. The solid black line represents where the data points would fall if the two data sets were in perfect agreement.

2.2.1.2 Epithermal and thermal neutron and gamma ray reconciliation

The ability of a material to absorb thermal neutrons is called the macroscopic neutron absorption cross section and is a weighted sum of the thermal neutron absorption cross sections of the constituent elements:

$$\Sigma_{eff} = \sum_i \frac{\sigma_i f_i N_A}{A_i}$$

(2) (Elphic et al., 2000)

where σ_i is the thermal neutron absorption cross section of constituent i, f_i is the weight fraction of i, A_i is the atomic mass of i, and N_A is Avogadro's number (Elphic et al., 2000). All components of the medium contribute to the macroscopic neutron absorption cross section, but those with relatively large cross sections that are present in significant quantities like iron and titanium, have a particularly large effect on the total cross section.

In addition, some isotopes of samarium and gadolinium, though they are present in lunar soil only at the ppm level, have a large contribution to the total cross section because their thermal neutron absorption cross sections are orders of magnitude larger than those of the other constituent elements of lunar soil (Elphic et al., 2000). Table 2.1 gives the thermal neutron cross sections for the major elements as well as the important rare earth elements Sm and Gd. The abundances of Sm and Gd were not measured directly using gamma ray spectroscopy, but they are correlated with each other and with thorium in lunar samples (e.g. Jolliff, 1998, Korotev, 2000) so they can be inferred if assumptions are made about the Sm/Th ratio and the Gd/Sm ratio and the distribution of isotopes.

The flux of thermal and epithermal neutrons from the lunar surface can be related to the macroscopic neutron absorption cross-section of the surface being treated by neutron transport models for the lunar samples (Feldman et al., 2000; Lawrence et al., 2010). Elphic et al. (2000) used a linear approximation for the relationship between macroscopic neutron absorption cross section and the epithermal to thermal neutron ratio given by (3), where f_{epi} and f_{thermal} are the measured epithermal and thermal neutron fluxes, respectively.

$$\Sigma_{eff} = a * \left({f_{epi}}/{f_{thermal}} \right) - b$$

$$a = 5.252 \times 10^{-3}$$

$$b = 1.485 \times 10^{-3}$$

(3) (Elphic et al., 2000)

The elements measured by the LP GRS can be compared with thermal and epithermal neutron data using equations 2 and 3 along with assumptions about Sm/Th and Gd/Sm ratios for the lunar surface using the microscopic neutron absorption cross sections of the elements. We assumed Gd=1.17*Sm (Jolliff, 1998; Korotev, 2000) and, following Gillis et al. (2003) used a beginning assumption of Sm=2.7*Th. The result of a comparison using these assumptions and equations 2 and 3 are shown in Figure 2.2a. This distribution also falls systematically off the 1:1 correlation line. We performed an

optimization varying the parameters of equation 3 within 2σ and allowing the Sm/Th ratio, which has a wide range in lunar samples (Wieczorek et al. 2006), to vary. The two datasets were brought into agreement with minor modifications of the parameters of equation 3 to $a = 5.732 * 10^{-3}$ and $b = 1.386 * 10^{-3}$ and a global Sm/Th ratio of 2.39. Table 2.2 summarizes the modified parameters for equations 1 and 2 resulting from our neutron and gamma ray reconciliation.

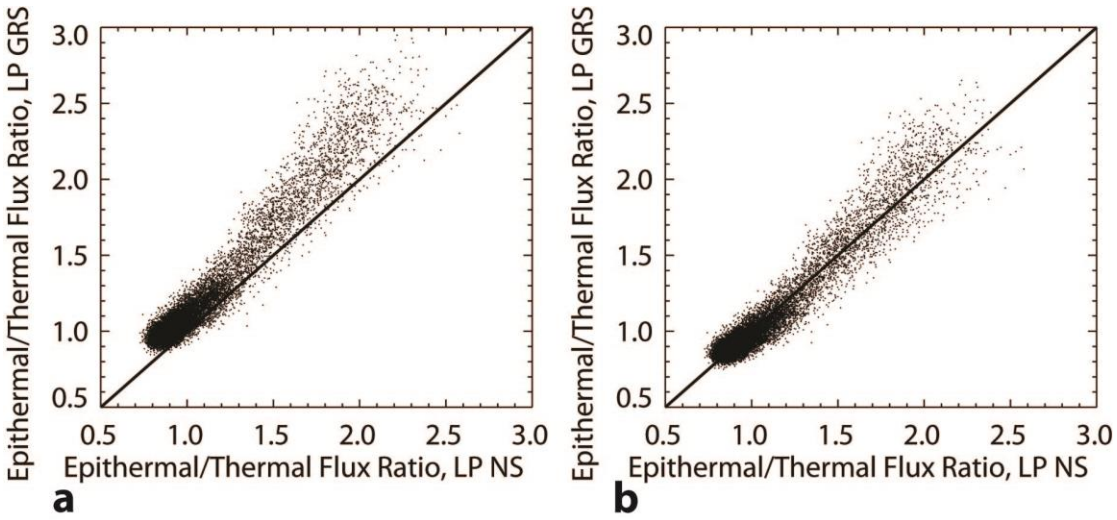

Figure 2.2a): Measured epithermal to thermal neutron flux from the LP NS plotted against the predicted epithermal to thermal neutron flux as calculated using equations (2) and (3) from LP GRS oxides with Sm=2.7*Th (Gillis et al., 2003) and Gd=1.17*Sm (Jolliff, 1998; Korotev, 2000). **2.2b):** Measured epithermal to thermal neutron flux from LP NS plotted against predicted epithermal to thermal neutron flux ratio from LP GRS calculated using equation (2) and (3) with $a = 5.732 * 10^{-3}$ and $b = 1.386 * 10^{-3}$ with Sm=2.39*Th and Gd=1.17*Sm.

Table 2.2. Comparison of literature values for the constants in equations 1 and 2 for comparing neutron flux with gamma ray elemental abundances with the modified values obtained in this work to bring the two datasets into agreement.

	Parameter	Literature values	This work
Fast neutron and gamma ray reconciliation	e	$26 +/- 6 * 10^{-3}$ (Gasnault et al., 2001)	$25.6 * 10^{-3}$
	f	11 +/- 3 (Gasnault et al., 2001)	10.6
Thermal and epithermal neutron and gamma ray reconiciliation	a	$5.252 * 10^{-3}$ (Elphic et al., 2000)	$5.732 * 10^{-3}$
	b	$1.485 * 10^{-3}$ (Elphic et al., 2000)	$1.386 * 10^{-3}$
	Sm/Th	2.7 (Gillis et al. 2003)	2.39

2.2.2 Reconciliation of Clementine-based mineral maps with Lunar Prospector

2.2.2.1 Mineral-map derived oxides and GRS

The Clementine mission mapped the Moon in 11 multispectral bands at 100-200 m spatial resolution from ultraviolet to near-infrared wavelengths (0.4 to 2.7 microns) (Nozette et al., 1995). Lucey (2004) used radiative transfer modeling to match computed spectra of mixtures of the major lunar minerals olivine, plagioclase, orthopyroxene, and clinopyroxene with observed Clementine spectra of the lunar surface. Because the exposure of the lunar surface to space weathering results in decreased spectral contrast, the optical maturity parameter of Lucey et al. (2000a, 2000b) was used to limit the analysis to fresh exposures. The mineral maps were interpolated to fill the gaps between fresh exposures, resulting in global mineral maps for olivine, plagioclase, orthopyroxene, clinopyroxene, and mafic mineral magnesium number (Mg#) of varying spatial resolution in the final dataset (Lucey, 2004) which we used in this analysis.

The mineral maps can be converted to oxides for direct comparison to the LP GRS oxides using simple stoichiometry along with assumptions about Mg# for olivine

and pyroxene and calcium content for clinopyroxene. Using the Mg# map produced by Lucey (2004) as the Mg# for the mafic minerals, and assuming Wo_{40} for clinopyroxene (Papike et al. 1998) we produced global maps of SiO_2, Al_2O_3, FeO, MgO, and CaO. The abundance of ilmenite was inferred from the TiO_2 abundances of Gillis et al. (2003) and then converted back into TiO_2 and FeO to complete mapping of the major oxides measured by the LP GRS. The mineral map-derived oxides were then sampled at the 2°/pixel resolution of the LP GRS oxides. Figure 2.3a-f shows the correlation between LP GRS oxides and mineral map-derived oxides. There is significant scatter for all of the oxides except iron, for which good agreement is expected because the LP GRS FeO distribution was a constraint in the construction of the mineral maps (Lucey, 2004). For the rest of the oxides, either a poor correlation is present, or the signal to noise ratio in the data sets relative to the variation in the element may obscure a correlation. The relationship between the mineral map and LP GRS aluminum (Fig. 2.3b) is strikingly non-linear and especially merited further investigation.

Al_2O_3 and FeO show a strong negative correlation in lunar samples (e.g. Haskin and Warren, 1991; Korotev et al., 2003). Prettyman et al. (2006) used lunar sample and meteorite data to obtain the relationship $Al_2O_3 = -1.2\ FeO + 32.4$, $R^2=0.95$ and used this trend to adjust the calibration of the LP GRS iron and aluminum data. The resulting trend, shown in Figure 2.4a, contrasts vividly with the nonlinear relationship between FeO and Al_2O_3 obtained from the mineral maps of Lucey (2004), shown in Figure 2.4b. Investigation of the spatial distribution of the low-iron, low-aluminum region of Figure 2.4b revealed a correspondence with high abundance of orthopyroxene (Figure 2.5a,b). The detection of orthopyroxene is robust as this mineral is the most distinct of the lunar minerals (Lucey 2004). However, plagioclase is featureless across the wavelength region used by Lucey (2004), and easily masked by the presence of other minerals. If orthopyroxene were correlated with plagioclase, the plagioclase might be obscured. We postulated that orthopyroxene detections may in fact be rocks of mixed orthopyroxene and plagioclase composition (as in a norite).

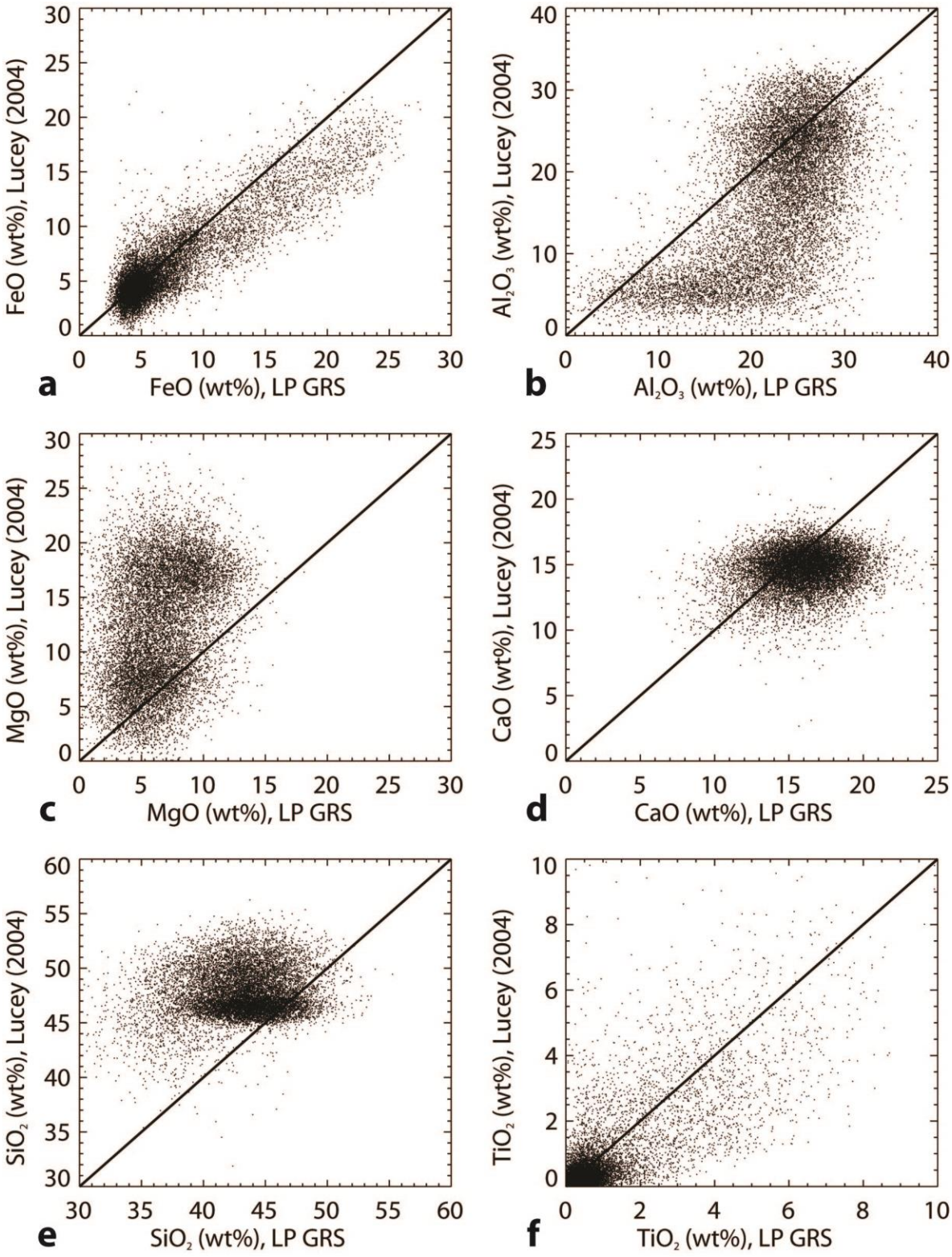

Figure 2.3a): FeO derived from the mineral maps of Lucey (2004) and ilmenite based on the TiO_2 abundance of Gillis et al. (2003) compared with LP GRS FeO; **2.3b):** Al_2O_3;

2.3c): MgO; **2.3d):** CaO; **2.3e):** SiO_2; **2.3f):** Spectrally-derived TiO_2 of Gillis et al. (2003), the basis for our ilmenite estimate, compared with LP GRS TiO_2. The line shown in each plot is that of a 1:1 correlation, where all points would fall if the two data sets were in perfect agreement.

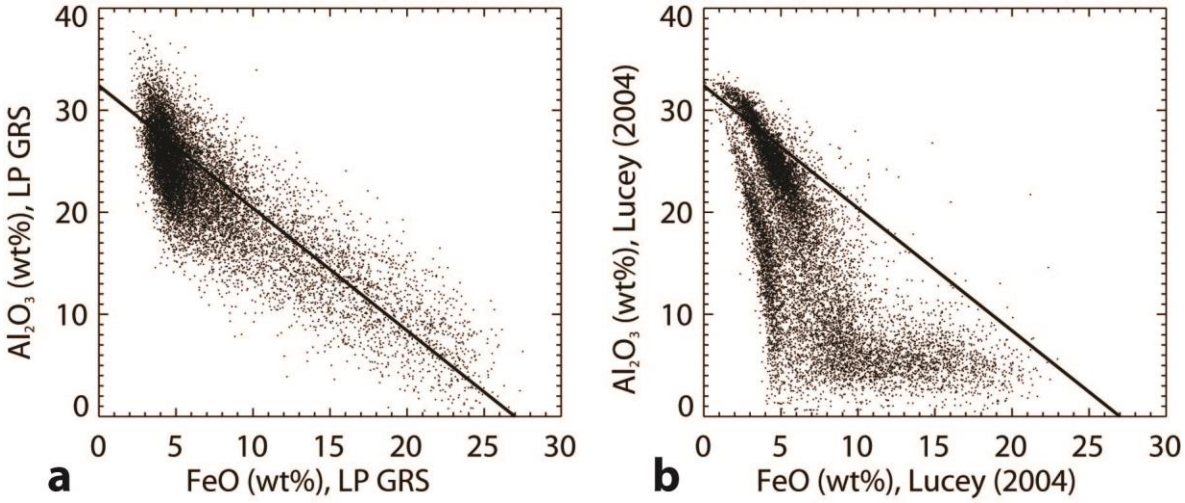

Figure 2.4a): Aluminum and iron oxides from the Prettyman et al. (2006) LP GRS 2 degree dataset; **2.4b):** Aluminum and iron oxides calculated from the mineral maps of Lucey (2004). The solid line in each plot shows the linear relationship between aluminum and iron in lunar samples as determined by Prettyman et al. (2006): $Al_2O_3 = -1.2\ FeO + 32.4$.

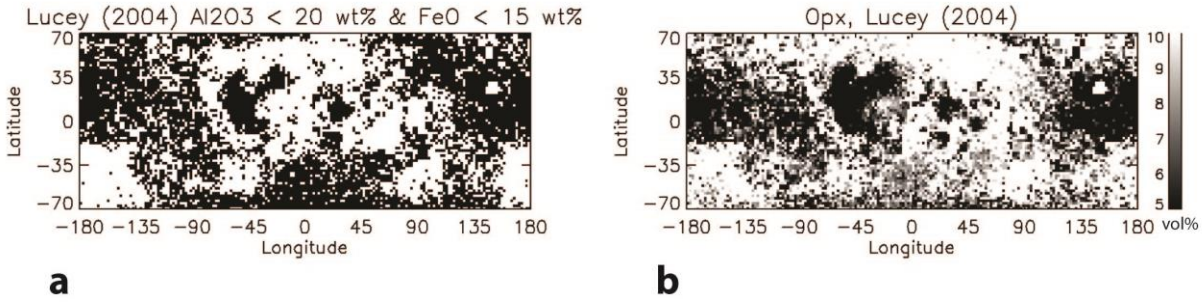

Figure 2.5a): White corresponds with areas of the Moon where FeO derived from the mineral maps of Lucey (2004) is less than 15 wt% and Al_2O_3 derived from the same maps is less than 20 wt% (areas in Fig. 2.4b) that fall well below the expected aluminum-iron trend from lunar samples). **2.5b):** Orthopyroxene map of Lucey (2004),

stretched between 5 and 10 vol% to show a correspondence of the low-aluminum, low-iron regions shown in 2.5a) with higher orthopyroxene abundance.

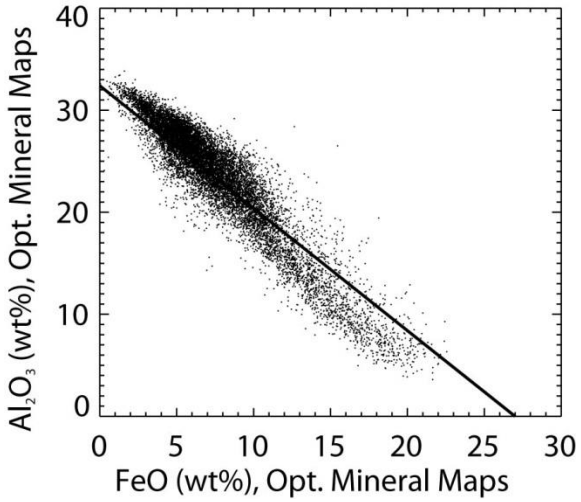

Figure 2.6: Aluminum and iron oxides calculated from the optimized mineral maps. The solid line shows the linear relationship between aluminum and iron in lunar samples as determined by Prettyman et al. (2006): $Al_2O_3 = -1.2\ FeO + 32.4$.

Following this hypothesis, we performed an optimization in which we added plagioclase in proportion with orthopyroxene, renormalizing the minerals to 100% with each step. The metric for improvement was the linear correlation coefficient between FeO and Al_2O_3 from the modified mineral maps. In order to maintain agreement of the new mineral maps with LP GRS iron, it was necessary to decrease Mg# for the mafic minerals for the same pixels, in proportion with orthopyroxene abundance. We constrained the iron abundance calculated from the modified mineral maps to maintain a linear correlation coefficient of 0.73 or better with the LP GRS FeO, with the mean of the modified mineral map FeO constrained to remain within 0.55 wt% of the LP GRS FeO. Figure 2.6 shows the result of this optimization, with the modified mineral maps showing improved agreement with the iron-aluminum trend seen in lunar samples. Figure 2.7 shows a comparison of the major oxides calculated from the optimized mineral maps compared with the LP GRS oxides. The non-linear behavior of the mineral map-derived aluminum was eliminated, and as a secondary result of improving the iron-aluminum

trend by decreasing the Mg# for the mafic minerals, mineral map MgO was also brought into better agreement with the LP GRS oxide.

2.2.2.2 Revised mineral map Mg#

Lucey (2004) modeled mafic mineral chemistry in the form of the magnesium number (Mg# = mole percent MgO/(MgO+FeO)) in order to obtain maps of the major lunar minerals. We used this original Mg# map (Fig. 2.8a) as a starting point for our optimization. After decreasing Mg# relative to orthopyroxene to maintain agreement of our new, higher plagioclase mineral maps with LP GRS iron, we obtained the optimized Mg# map of Figure 2.8b. Prettyman et al. (2006) commented on the difficulty of measuring variations in Mg# with the LP GRS data because of the low precision of the MgO data. Despite this caution, the Mg# values seen in our optimized map ranged from about 40 to 80, generally consistent with the range seen by the LP GRS.

However, the revised Mg# map strongly differs from the Mg# from LP GRS (Fig. 2.8c) in the western maria (outlined in black). The western maria are unique: they are among the youngest mare basalts on the surface of the Moon (e.g. Heisinger and Head, 2011); they are high in iron (e.g. Lucey et al., 2000a; Staid and Pieters, 2001; Elphic et al., 2002; Prettyman et al., 2006); and they have been mapped as olivine-rich on the basis of an unusually strong 1 um absorption combined with weak absorption at 2 um by many authors (e.g. Pieters et al., 1980; Staid and Pieters, 2001; Lucey, 2004; Staid et al., 2011), as well as by this study (Figure 2.11c). If the olivines in this unique region are of a separate origin than the other minerals, for example, if they are mantle phenocrysts, it would be reasonable to decouple the Mg# for olivine from that of the other minerals.

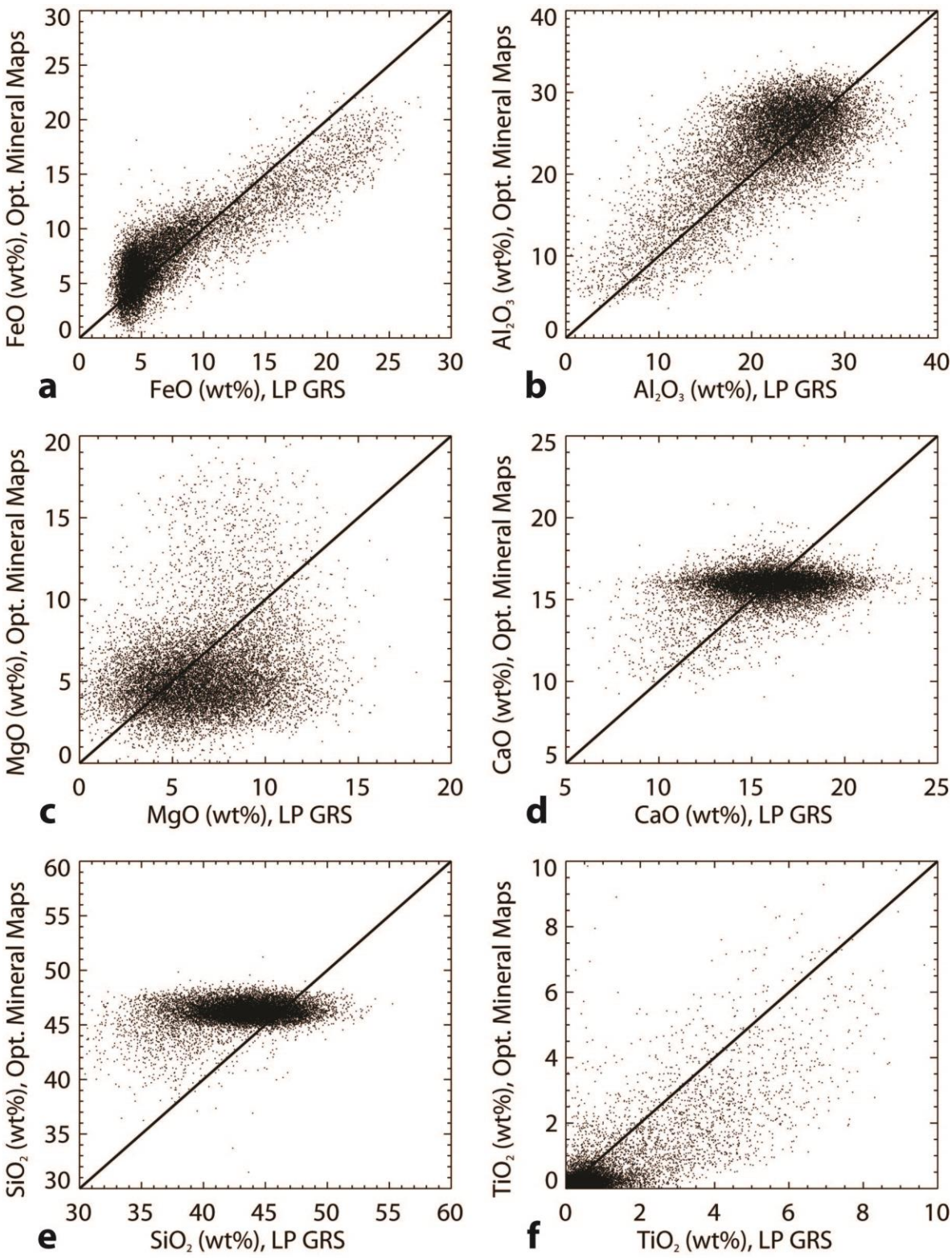

Figure 2.7a): FeO derived from the optimized mineral maps with LP GRS FeO; **2.7b):** Al_2O_3; **2.7c):** MgO; **2.7d):** CaO; **2.7e):** SiO_2; **2.7f):** TiO_2. The line shown in each plot is

that of a 1:1 correlation, where all points would fall if the two data sets were in perfect agreement.

To bring our Mg-number map into better agreement with Lunar Prospector in this region, we decreased Mg# for olivine only in the outlined region of the western maria, maintaining the Mg# for orthopyroxene and clinopyroxene at the values seen in Figure 2.8b, until the mean of the Mg# calculated from the mineral-map derived oxides in that region equaled the mean of the LP GRS Mg# in the same region. An Mg# of 24.3 for olivine in this region was required to reach a mean value equal to the GRS mean Mg# of 39.4. The final Mg# map derived from the mineral maps with modified olivine Mg# is shown in Figure 2.8d. While the overall mean of the LP GRS Mg# is still higher than the mean of our final Mg# map (62 vs. 57), our maps cover the same Mg# range and fall much closer to the LP GRS values than the original Mg# map of Lucey (2004), which had a mean Mg# of 78.

The effect of lowering the overall Mg# in this region was an upturn in FeO abundances above the LP GRS trend for this region (Figure 2.9a). To counter this effect we increased plagioclase in this region, renormalizing the minerals to 100% with each step, until the mean FeO content derived from the mineral maps was equal to the mean FeO from LP GRS. The result of this adjustment, which required a 7 vol% increase in plagioclase on average (after renormalization to 100%), is shown in Figure 2.9b. Figure 2.9c shows the aluminum-iron trend that results after adjusting Mg# and plagioclase content. Our final adjustments resulted in a distinct break in the slope of the aluminum-iron trend. However, some non-linearity is also seen in lunar sample data as a result of soils that are not simple mixtures of mare basalt and feldspathic highland soil as well as the higher FeO/MgO ratio of mare basalts relative to highland samples (Fischer and Pieters, 1995; Lucey et al., 2006). A comparison of FeO+MgO with Al_2O_3 removed nonlinear effects introduced by varying FeO/MgO ratios and revealed general good agreement with the linear trend seen in lunar samples (solid line; Lucey et al., 2006).

Ohtake et al. (2012) reported an Mg# map for the lunar highlands obtained using spectra from the Kaguya Spectral Profiler (Fig. 2.10b). A comparison of our optimized Mg# map with the map of Ohtake et al. (2012) reveals qualitative spatial agreement

between the two maps, with Mg# highest in the farside highlands, and similar mean values (56 from the map of Ohtake et al. (2012), 61 from our optimized map).

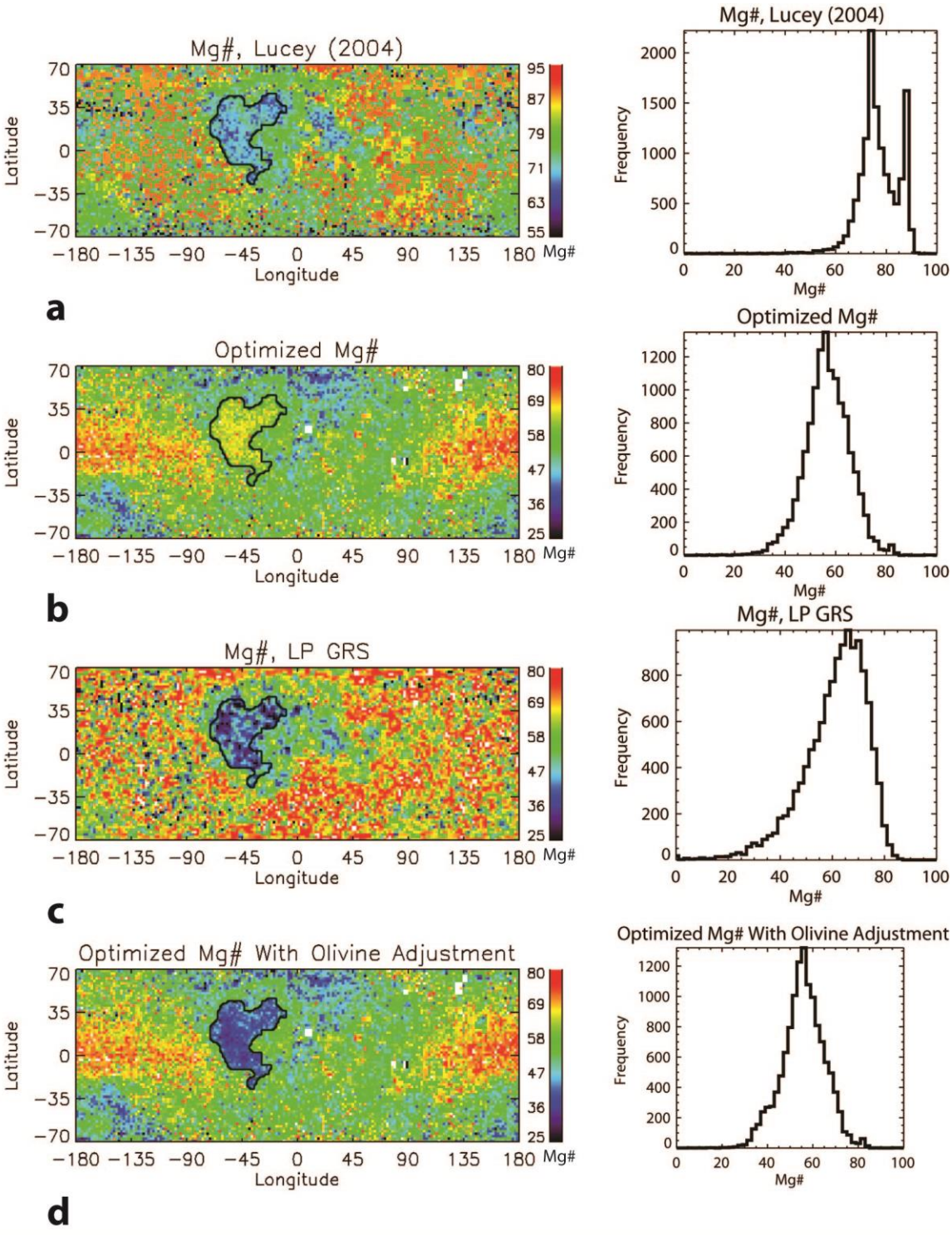

Figure 2.8: Global maps and histograms showing Mg# for the mafic minerals from a) Lucey (2004); b) the optimized Mg# obtained by the method described in the text; c) Lunar Prospector GRS FeO and MgO maps; d) optimized Mg# from 2.8b with adjustments made for the Mg# of olivine in the western maria as described in this section. Black outlines show the olivine-rich western mare region adjusted in 2.8d.

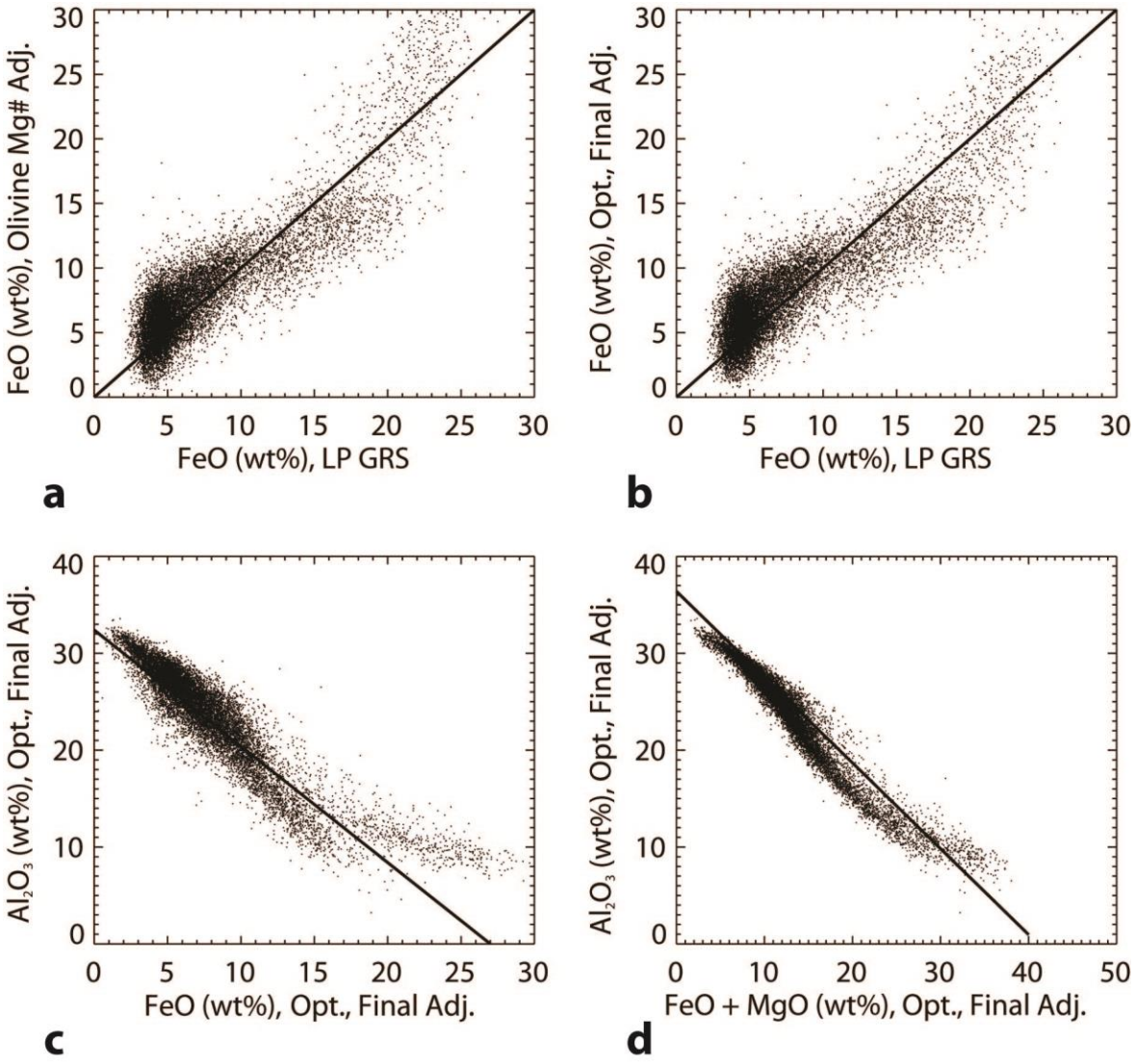

Figure 2.9: FeO abundance in wt% from LP GRS compared with **a):** mineral-map derived FeO with lowered olivine Mg# in the western maria; **b):** mineral-map derived FeO with lowered olivine Mg# and increased plagioclase in the western maria. Solid lines shown in a) and b) are the line of 1:1 correlation. **c):** Al_2O_3 and FeO in wt% calculated from the Mg# map of Fig. 2.8d and the final mineral maps shown in Fig. 2.11.

The solid line shown is the linear relationship between aluminum and iron in lunar samples as determined by Prettyman et al. (2006): $Al_2O_3 = -1.2\ FeO + 32.4$. d) Al_2O_3 plotted against FeO + MgO for the same maps. The solid line shown is the linear trend between Al_2O_3 and FeO+MgO in lunar samples from Lucey et al. (2006): Al_2O_3=-0.886(FeO+MgO)+36.4.

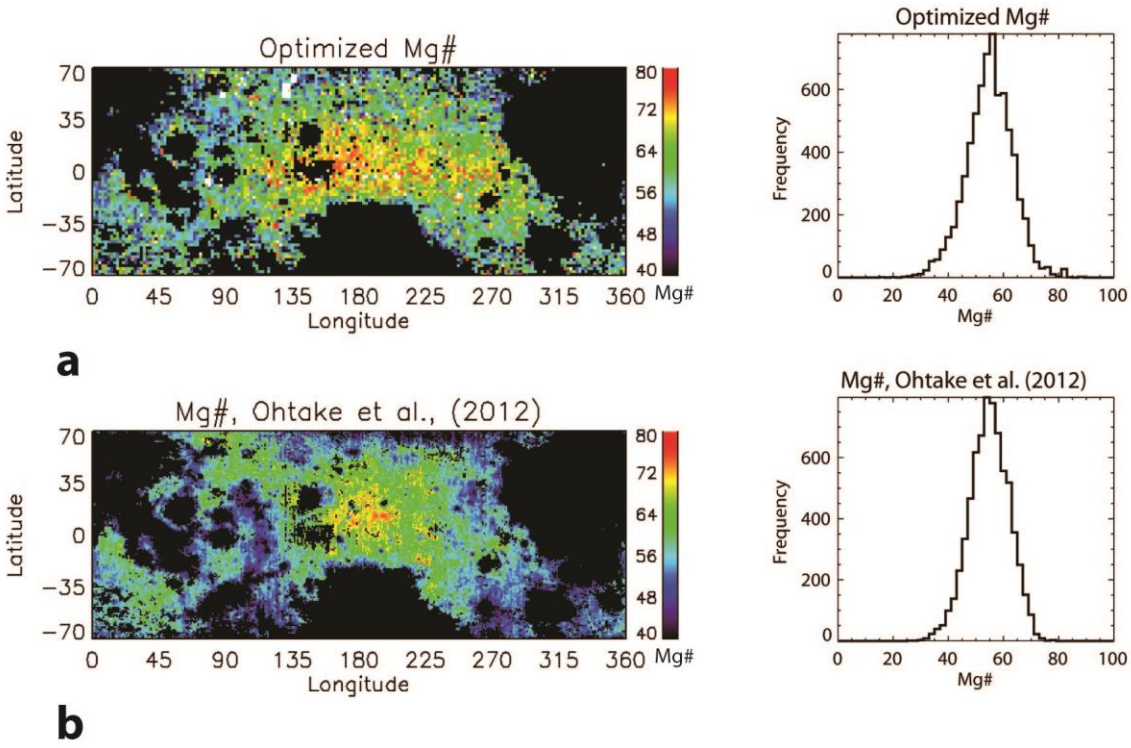

Figure 2.10: Mg# maps and histograms for **a):** optimized Mg# obtained following the procedure described in Section 3.3.1; **b):** Mg# from the SELENE Spectral Profiler, obtained by Ohtake et al. (2012). Black areas were not analyzed by Ohtake et al. so are removed from both maps. Only colored regions are reflected in the histograms. General spatial agreement is seen between the two Mg# analyses.

2.3 Results and Discussion

The result of this study is a new set of global major mineral maps, based on Clementine UVVIS spectra, validated and improved by comparison with global data from Lunar Prospector's neutron and gamma ray spectrometers. The Lunar Prospector-

validated maps of plagioclase, clinopyroxene, orthopyroxene, olivine, and ilmenite are shown in Figure 2.11.

The average plagioclase content of the highlands in the new maps is over 80 vol%, in contrast with an average of 75 vol% in the 2004 maps. Plagioclase remains anti-correlated with clinopyroxene as in the maps of Lucey (2004), reflecting mare-highland differences. Our comparison of mineral-map derived oxides with GRS oxides revealed that plagioclase, easily masked by the strong orthopyroxene spectral signature, is likely to coexist with orthopyroxene across the lunar surface, as in a norite, so in our revision of the mineral maps we have introduced a correlation of plagioclase with orthopyroxene that is visible in the maps.

Clinopyroxene is the dominant mafic mineral in the maria with the exception of the anomalous western maria, where olivine reaches equal proportions. Clinopyroxene is also present at a relatively high level throughout the highlands and accounts for about 50% of the total mafic contribution to the highlands. This is consistent with the detection of high-calcium pyroxene in fresh craters with diameters between 8 and 24 km throughout the lunar highlands by Ogawa et al. (2011) using Kaguya Spectral Profiler data, and may be evidence for a deep gabbroic layer beneath the anorthositic crust (Ogawa et al. 2011).

The mean of the revised olivine distribution is slightly lower than that estimated by Lucey (2004), near 7 vol% rather than 10 vol%, but some areas of the western maria maintain olivine contents as high as 30-40 vol%. The revised abundance of orthopyroxene is similar to that in the maps of Lucey (2004), with average contents slightly lower (5 vol% rather than 10 vol%). The distribution of ilmenite is almost entirely dependent on the TiO_2 maps of Gillis et al. (2003) and was changed very little by the optimization.

Throughout this study we used major-element relationships from lunar samples and gamma-ray spectroscopy to improve our spectroscopy-based mineral maps; lunar sample mineralogy provides another point of reference for our revised mineral abundances. In the proceedings of the first Conference on the Lunar Highlands Crust

Stöffler et al. (1980) proposed a classification scheme for lunar highland rocks based in part on their positions in compositional fields on plagioclase-pyroxene-olivine and plagioclase-orthopyroxene-clinopyroxene ternary diagrams. Although the rock type compositional fields were intended only for the classification of plutonic lunar highland rocks (Stöffler et al. 1980), since the Moon's major mineralogy is largely restricted to plagioclase, olivine, and pyroxene (e.g. Papike et al. 1998), these ternary diagrams provide a useful way to visualize mineralogy of samples and remote sensing data from all areas of the Moon including the maria.

The mineralogy distribution of the Lucey (2004) maps on the plag-pxn-ol ternary of Figure 2.12a includes a field of points that fall outside the outlined field in which the known lunar soils from the Apollo and Luna missions and the feldspathic lunar meteorites plot. Figure 2.12b shows the dramatically improved agreement of the Lunar Prospector-validated mineral maps of this study with the field occupied by lunar samples. Figure 2.12c shows the distribution in mineralogy of the revised maps on the plag-opx-cpx ternary used by Stöffler et al. (1980) for classification of highland rocks, and highlights the presence of clinopyroxene as a major mafic mineral for much of the lunar surface. Mare-highland differences are reflected in Figure 2.12c, in which clinopyroxene is highest where plagioclase is low.

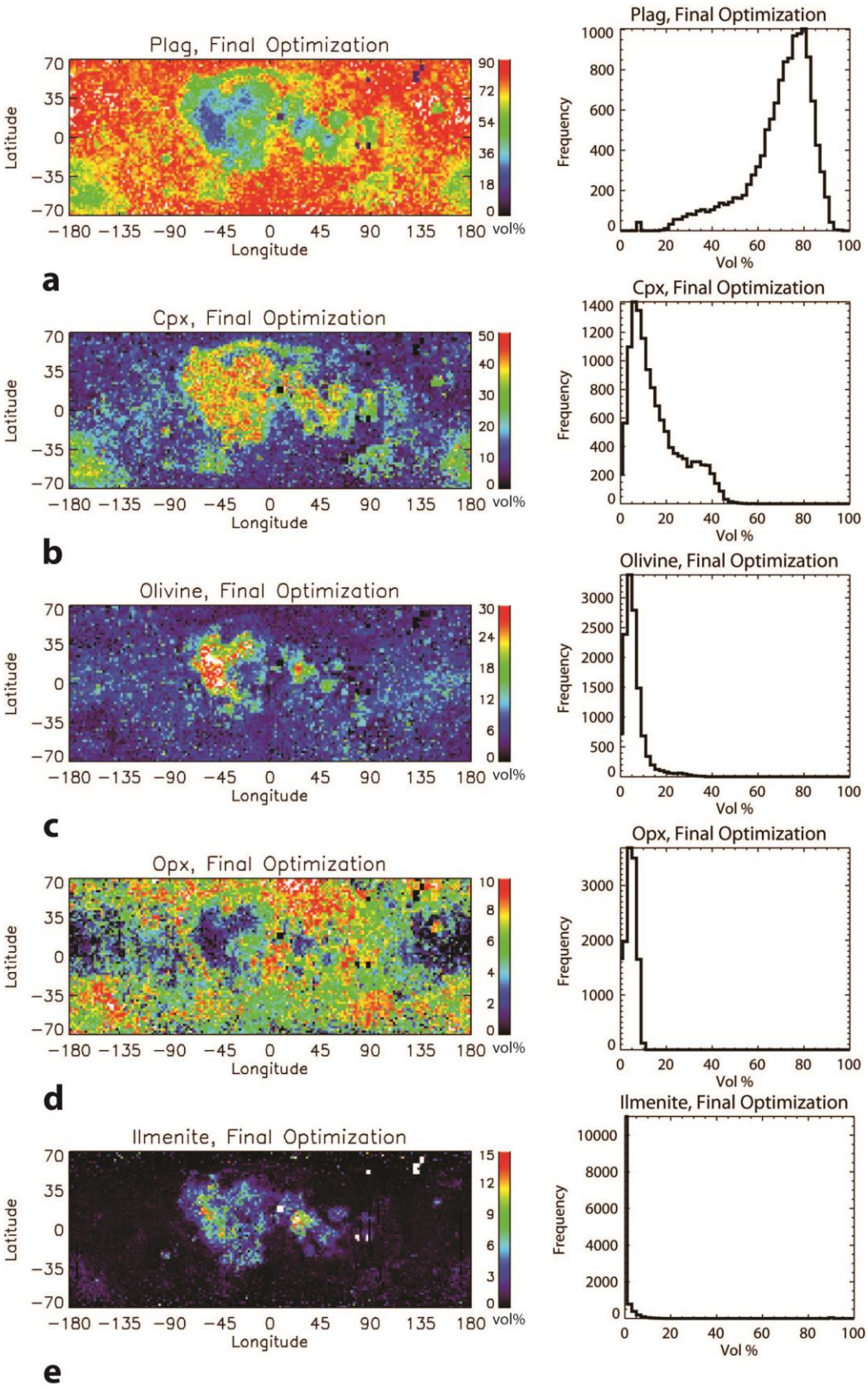
Plag, Final Optimization
Latitude
Longitude
vol%
Frequency
Vol %
a
Cpx, Final Optimization
b
Olivine, Final Optimization
c
Opx, Final Optimization
d
Ilmenite, Final Optimization
e

Figure 2.11: Lunar major mineral global maps based on the maps of Lucey (2004) with optimization performed to bring the datasets into agreement with Lunar Prospector neutron and gamma ray results: **a)** plagioclase; **b)** clinopyroxene; **c)** olivine; **d)** orthopyroxene; **e)** ilmenite. The ilmenite map shown was inferred from the TiO_2 map of Gillis et al. (2003), then compared with LP GRS oxides and optimized along with the mineral maps of Lucey (2004).

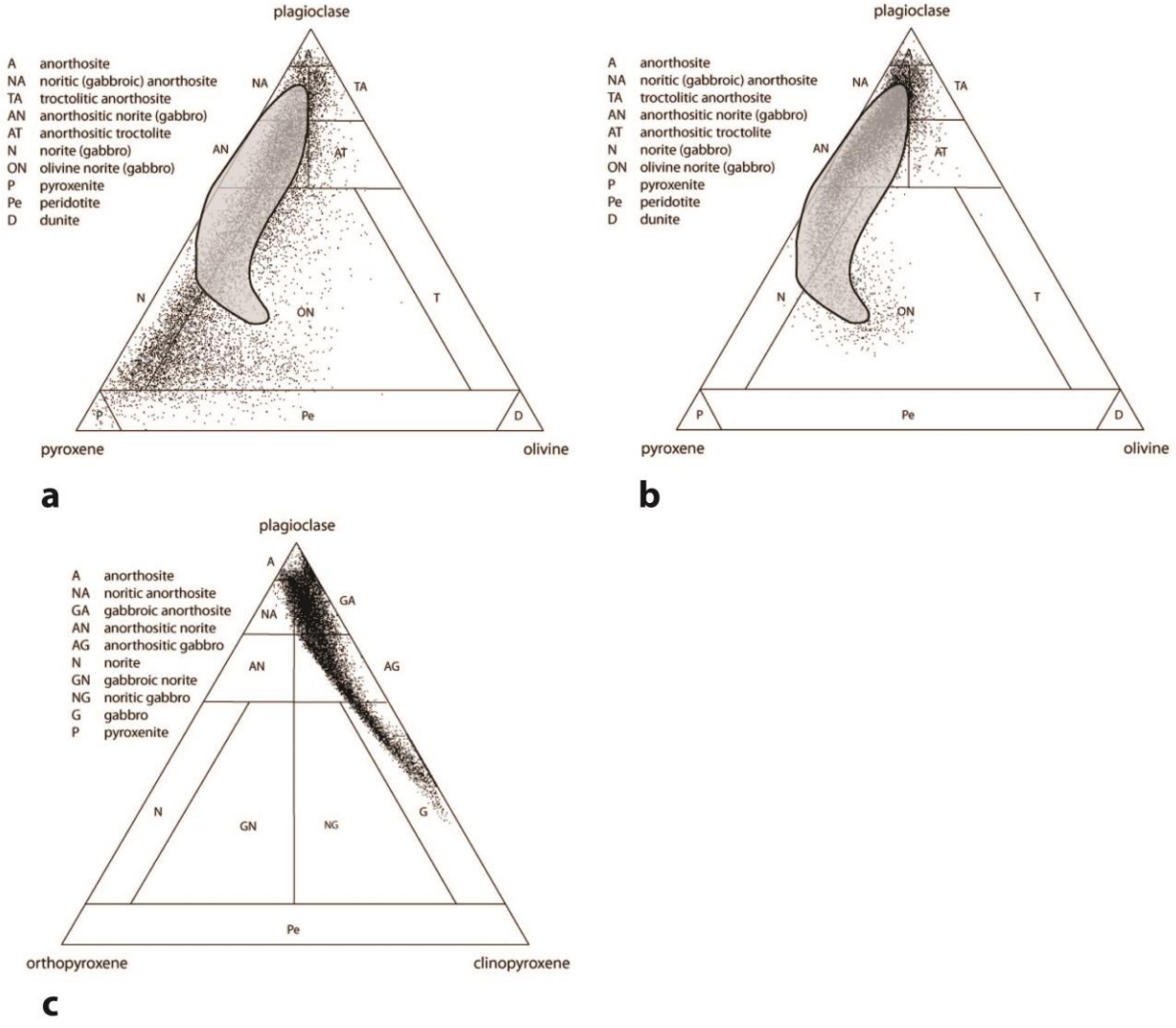

Figure 2.12a): Mineralogy of each pixel of the lunar surface from the maps of Lucey (2004), with olivine, opx+cpx, and plagioclase re-normalized to 100% displayed with the compositional fields for highland rocks defined by Stöffler et al. (1980). The shaded field, based on Fig. 2.3 of Lucey et al. (2006), shows the compositions of lunar soils

samples from the Apollo and Luna missions as well as lunar feldspathic meteorites. **2.12b):** The optimized mineralogy (plagioclase-pyroxene-olivine) obtained through our comparison to Lunar Prospector shows greatly improved agreement with known soils. **2.12c):** Optimized mineralogy from this study plotted on a plagioclase-orthopyroxene-clinopyroxene ternary displayed on the compositional fields defined by Stöffler et al. (1980).

2.4 Implications

We derived a robust set of global mineral maps based on Clementine UVVIS spectroscopy and validated against the self-consistent Lunar Prospector gamma ray and neutron spectrometer datasets. The revised mineral maps are in good agreement with lunar sample mineralogy. The distribution of highlands Mg# measurements in the revised maps are consistent with the Mg# measurements of Ohtake et al. (2012). The plagioclase content of these Lunar Prospector-validated maps is significantly higher than that of the original global mineral maps of Lucey (2004) and shows a pronounced plagioclase high in the central farside highlands that may be the remnant of an anorthositic craton (Jolliff et al. 2000). The revised mineral maps provide a tool that can be used to examine hypotheses of lunar formation and evolution. They also demonstrate the usefulness of LP neutron and gamma ray data as a validation tool for spectral mineral maps and algorithms.

The detections of high-Ca-pyroxene throughout the lunar highlands in our maps agree with observations by Ogawa et al. (2011). Ogawa et al. (2011) suggested this could indicate the presence of a deep gabbroic layer beneath the anorthositic crust or abundant calcium-rich trapped liquid. The work of Lucey et al. (2014) did not detect comparable high-Ca pyroxene abundances in small (<1 km diameter) fresh craters indicating the small crater results may be sampling a different crustal layer than the 8-24 km craters studied by Ogawa et al. (2011). Craters of the size range studied by Lucey et al. (2014) make up only a small percentage of the immature surfaces the mineral maps of this work were based on, so the contrast between the small crater mineralogy of Lucey et al. (2014) and our results are not unexpected. Nevertheless, the origin and vertical distribution of

high-Ca pyroxene in the lunar highlands remains a persistent mystery and a topic for future investigation.

CHAPTER 3

THE MAFIC COMPONENT OF THE LUNAR CRUST: CONSTRAINTS ON THE CRUSTAL ABUNDANCE OF MANTLE AND INTRUSIVE ROCK, AND THE MINERALOGY OF ANORTHOSITES

In review for publication in *American Mineralogist* as Crites, S.T., Lucey, P.G., and Taylor, G.J., The mafic component of the lunar crust: Constraints on the crustal abundance of mantle and intrusive rock, and the mineralogy of lunar anorthosites.

Abstract—Most models of early lunar evolution predict that the anorthositic highlands crust is the result of plagioclase flotation on a magma ocean. However, the lunar highlands crust typically contains 4 wt% FeO and so is more mafic than the strict definition of the anorthosites thought to comprise it. We used new Clementine-based mineral maps of the Moon (Crites et al., 2014) as inputs to a series of mixing models that calculate the abundance and distribution of major highland rock types and shed light on three possible sources of excess mafic material in the lunar highlands: mafic (15 vol% mafic minerals) anorthosites, post-magma ocean igneous activity, and mafic basin ejecta. Mixing models that feature pure anorthosites like the purest anorthosite (PAN) described by Ohtake et al. (2009) and Pieters et al. (2009a) are most compatible with the mineral maps we use to constrain them. They allow us to place an upper limit of 10-20 vol% mantle material that could be mixed with the primary highlands crust. The upper limit on mantle material indicated by the mixing models is significantly lower than the 30-40 vol% mantle material expected from simple geometric calculations of the major lunar basins' excavation cavities based on an excavation cavity depth/diameter ratio of 1/10; this discrepancy allows us to conclude that the excavation cavities of the three largest lunar basins may have been significantly shallower than those predicted from scaling laws based on small craters. Our results are consistent with depth/diameter ratios for these largest basins in the range of 0.035 to 0.06, which agrees with previous gravity measurements by Wieczorek and Phillips (1999).

3.1 Introduction

The magma ocean hypothesis (e.g. Smith et al. 1970; Wood et al. 1970; Warren and Wasson 1977; Warren 1985; Snyder et al. 1992) provides a framework for the story of the Moon's early history: a primary crust of anorthosite making up the lunar highlands formed from floating as a melt differentiated; the nearside maria are the result of relatively recent volcanism (Neil and Taylor 1992). Both samples (e.g. Wood et al. 1970; Korotev et al. 2003; Warren 1990) and remote sensing (e.g. Hawke et al. 2003; Prettyman et al. 2006; Ohtake et al. 2009; Pieters et al. 2009a; Cheek et al. 2013) provide strong support for the magma ocean hypothesis. However, the typical lunar highlands surface contains 4-5 wt% FeO (Korotev et al. 2003; Prettyman et al. 2006) or over 15 vol% mafic minerals, and so is more mafic than strictly defined anorthosites (<10 vol% mafic minerals, Stöffler et al. 1980), and much more mafic than the very anorthositic "purest anorthosites" (PAN) detected ubiquitously in craters larger than 30 km by Ohtake et al. (2009), which contain less than 2 vol% mafic minerals. This raises the question of the source of the excess mafic material in the lunar highlands that may not be associated with magma ocean anorthosites.

Samples and remote sensing reveal the complexity of the lunar crust (e.g. James 1980; Ryder and Spudis 1980; Pieters 1986; Tompkins and Pieters 1999; Warren 1990) and attest to the variety of processes that could lead to the observed elevated mafic content of the lunar highlands. We examined three possible explanations for the elevated abundances of mafic material: 1) the lunar anorthosites are inherently more mafic than the strict definition, as suggested by Warren (1990); 2) magma ocean anorthosites are mixed with mafic post-magma ocean igneous intrusions (POI) or extrusive volcanism (Ryder and Spudis, 1980); and 3) mafic lower crust or mantle material was excavated by large-scale basins and is mixed with the anorthositic upper crust (Ryder and Wood, 1977). We used mineral maps derived from Clementine UVVIS spectra (Lucey, 2004) and improved through reconciliation with Lunar Prospector neutron and gamma ray spectrometer results by Crites et al. (2014, Chapter 2) to examine the consistency of various combinations of these non-mutually exclusive scenarios. We constrain the

probable mafic content of lunar magma ocean anorthosites and plausible contributions of igneous activity and mantle contamination to the lunar highland crust.

3.2 Methods

We use a new set of global mineral maps (Crites et al., Chapter 2) obtained by reconciling the Clementine-based mineral maps of Lucey (2004) with Lunar Prospector gamma ray spectrometer (GRS) 2°/pixel oxide abundances (Prettyman et al. 2006) to obtain estimates of the distributions of the major highland rock types. Lucey (2004) used radiative transfer modeling combined with Clementine UVVIS spectra of immature locations on the Moon to obtain maps of plagioclase, orthopyroxene, clinopyroxene, olivine, and magnesium number. The maps were interpolated between immature locations to create a continuously gridded global dataset. Crites et al. (Chapter 2) identified systematic discrepancies between the major oxides derived from these mineral maps and geochemical trends in lunar samples and Lunar Prospector GRS oxides, then reconciled these differences to obtain a new set of mineral maps consistent with GRS oxides and sample trends. These maps included the four major minerals and magnesium number (Mg#) maps modified from Lucey (2004) as well as ilmenite based on the TiO_2 maps of Gillis et al. (2003).

3.2.1 Rock types representing three sources of mafic material

Using assumptions about rock type compositions along with the newly refined mineral abundances, we produced a series of mixing models and assessed the validity of the results to guide our conclusions about the relative importance of the three sources of mafic material to the lunar highlands. The rock types we included in our mixing model were: anorthosite, the major crustal magma ocean product; norite, troctolite, and gabbro or mare basalt, used to represent post-magma ocean igneous intrusive or extrusive volcanism and mare basalt contamination; and dunite and pyroxenite, ultramafic rock types representing the lunar mantle. We used dunite and pyroxenite to represent mantle compositions, but locations where both are present in our model results are also consistent with peridotite.

Most magma ocean models agree that the anorthosite in the lunar highlands crust likely formed by flotation of plagioclase crystals on a dense melt (e.g. Snyder et al. 1992), but the extent to which magma ocean processes isolated plagioclase to the exclusion of mafic minerals in anorthosite is uncertain. Warren (1990) concluded from models of anorthosite flotation on a dense melt that the overall resulting suite of anorthosites should contain approximately 15 vol% mafic silicates. Anorthosites in the sample collection show a wide range of mafic contents ranging from the mafic anorthosite of Warren (1990) to the remote sensing-based "purest anorthosite" (PAN, <2 vol% mafics) of Ohtake et al. (2009), with an average mafic content of 7 vol% (Wieczorek et al. 2006). Spectral measurements by the Kaguya Spectral Profiler and Multiband Imager (Ohtake et al. 2009; Yamamoto et al. 2012) and the Moon Mineralogy Mapper (Pieters et al. 2009a) showed that nearly pure exposures of anorthite are common across the lunar surface showing that this variety of anorthosite is not uncommon. In the study of anorthosites exposed at Orientale, Cheek et al. (2013) found that the Inner Rook Ring was almost entirely dominated by extremely low mafic content anorthosites. More mafic feldspathic material is principally found elsewhere in the basin in locations more susceptible to mixing. The observations of Cheek et al. (2013) strongly suggest that LMO anorthosites, at least in the vast Orientale region, have inherently low mafic contents and the mafic anorthosites suggested by Warren are the exception, not the rule. Despite this, mafic anorthosites do occur in the sample collection, so we explored the effect on our mixing models of varying anorthosite mafic content. In order to cover the full range of solutions, we calculated rock type abundances based on pure anorthite (0 vol% mafics), the PAN of Ohtake et al. (2009) with 2 vol% mafics, anorthosites with the lunar sample-based average 7 vol% mafic component, and the 15 vol% mafic anorthosites of Warren (1990).

In addition to defining the total amount of mafic silicates present in anorthosites, the mixing analysis required assumptions about the relative abundances of the three mafic minerals olivine, orthopyroxene, and clinopyroxene in anorthosites. We calculated the average composition of the lunar samples classified as anorthosites catalogued by Cahill and Lucey (2007) and from this average composition (93.3% plagioclase, 3.6% olivine, 2.1% orthopyroxene, and 0.9% clinopyroxene) we obtained these relative abundances of

the minerals: 1:0.6:0.2 ol:opx:cpx. We maintained these relative abundances of mafics when incorporating the mafic minerals into anorthosites regardless of the total mafic content assumed, though it is important to note that the relative abundances of the mafic minerals vary widely across ferroan anorthosite suite samples (Warren, 1990; Cahill and Lucey 2007) so our choice of these proportions is arbitrary.

The mafic minerals olivine, orthopyroxene, and clinopyroxene are present in many mixed highland rock types other than anorthosites. For our analysis we simplified the major mafic-bearing rocks to simple binary mixtures of plagioclase and one of the three major mafic minerals. We categorized the rock types into three groups: post-magma ocean highland igneous rocks (POI rocks: norite, troctolite, gabbro); mantle ultramafics (dunite, pyroxenite); and mare basalt. We used the lunar samples catalogued by Cahill and Lucey (2007) as a guide and averaged the major mineral compositions for all samples in each class. For example, the average of the major mineral composition of sample norites is 47.9% plagioclase, 49.3% orthopyroxene, 0.67% clinopyroxene, and 1.6% olivine. We then simplified each rock type to its two main constituent minerals (for example, norite = plagioclase + orthopyroxene) and obtained the average abundance of the two main constituents relative to each other (for norite, 49% plagioclase and 51% orthopyroxene). Table 3.1 shows the simplified rock compositions obtained by this method.

The assignment of clinopyroxene to lunar rock types presents a special complication. The dominant clinopyroxene-bearing rock in lunar samples is mare basalt (Papike et al. 1998). The mixed clinopyroxene and plagioclase highland rock type defined by Stöffler et al. (1980) is gabbro, but high-Ca pyroxene is not common in highland rocks samples (James 1980; Taylor et al. 1991), despite recent remote spectral measurements by Ogawa et al. (2011) that suggest that high-Ca pyroxene may be more abundant in the highlands than previously suspected. Furthermore, as a result of the heavy bombardment of the lunar surface, mare basalt fragments are present in nearly all regolith breccia lunar meteorites, including in feldspathic meteorites that may originate from the farside highlands, so at least some mixing of mare rocks with the highlands surface is certain (Korotev et al. 2006). For most of our calculations we therefore

assigned clinopyroxene to mare basalt contamination rather than to the POI rock gabbro. We averaged the compositions of mare basalts from Taylor et al. (1991), and, making the assumption that clinopyroxene dominates over orthopyroxene, simplified to plagioclase and clinopyroxene, then calculated the relative abundances of these two minerals. The result of this calculation is shown in Table 3.1.

Table 3.1. Compositions defined for non-endmember rock types.
Notes:
[a]Percent total mafic minerals in anorthosite is varied in our mixing models (0, 2, 7, or 15 vol%)
[b]Based on the composition and rock type interpretation of Mg-suite rocks catalogued by Cahill and Lucey (2007)
[c]Based on compositions of mare basalts from Taylor et al. (1991)
[d]Orthopyroxene and Clinopyroxene go into pyroxenite in the unique proportions in which they are present in each pixel

	% Plagioclase	% Olivine	% Opx	% Cpx	Origin
Anorthosite[a]	N	.54*(100-N)	.32*(100-N)	.14*(100-N)	Primary crust
Norite[b]	49	0	51	0	POI
Gabbro[b]	41	0	0	59	POI
Mare basalt[c]	32	0	0	68	POI
Troctolite[b]	53	47	0	0	POI
Dunite	0	100	0	0	Mantle
Pyroxenite[d]	0	0	OPX + CPX = 100		Mantle

In addition to primary magma ocean rocks (anorthosites), post-magma ocean highlands igneous activity (POI rocks, norite, gabbro, and troctolite), and mare basalt contamination, the mafic minerals can by carried by ultramafic mantle rocks. The Moon has experienced a violent bombardment history and several of the largest basins may have penetrated through the lunar crust to excavate mantle material (e.g. Spudis 1993; Lucey et al. 1998; Wieczorek et al. 2013). We simplified the endmember ultramafic rock types defined by Stöffler et al. (1980) to their primary constituents so that dunite was composed entirely of olivine and pyroxenite was composed of orthopyroxene and clinopyroxene in the proportions in which they were present in each pixel. In some runs of the mixing model we excluded clinopyroxene from the mantle in order to assess its effect on our mantle volume estimates; in these cases, pyroxenite consisted entirely of orthopyroxene.

3.2.2 Limits on the volume of mantle excavated

The mineral maps, along with the assumed rock type compositions, allowed us to calculate endmember cases in which all excess mafic minerals not in anorthosites were assigned either to norite, troctolite, and gabbro/mare basalt, or to the mantle ultramafics dunite and pyroxenite. However, the reality likely falls between the endmember cases, with some of the excess mafic material being contributed by large basin ejecta and some contributed by post-magma ocean igneous activity. These intermediate cases required an independent estimate of the relative abundance of crust and mantle. An estimate of the quantity of basin ejecta and percentage of mantle material can be calculated for the known lunar basins and this quantity used as an upper limit for mixing models. We used the geometric model described by Spudis (1993) to calculate the volume of mantle ejected by lunar basins. A number of assumptions including the depth to diameter ratio of lunar basin excavation cavities, the crustal thickness, and the appropriateness of applying proportional scaling to multiring basins affect the estimate of mantle volume excavated, so we performed mixing models using a range of assumptions that resulted in a range of mantle volumes excavated.

Spudis (1993) modeled the ejection cavities of five lunar multiring basins as the intersection of a spherical Moon with a hemispherical cavity penetrating to a depth of one-tenth its diameter based on the model of Croft (1981). The volume of mantle excavated was calculated as the intersection of the hemispherical ejection cavity with a smaller sphere with a radius equal to the difference between the average radius of the Moon and the original crustal thickness at the basin location (Spudis 1993) (that is, a sphere defined by the crust-mantle boundary). We followed the method of Spudis (1993) to calculate the total volume ejected by all 42 multiring basins defined by Spudis (1993) and also included the basin South Pole-Atiken (SPA). The transient crater diameter defined the circle of intersection of the sphere of the Moon with the sphere of the excavation cavity. We used transient crater diameter estimates from Table 2 of Petro and Pieters (2004). The excavation cavity depth was obtained by multiplying the diameter of the transient cavity by an excavation cavity depth/diameter ratio. We used a depth/diameter ratio of 0.1 for our initial calculations (e.g. Croft 1980, O'Keefe and

Ahrens 1993, Wieczorek and Phillips 1999), and later varied this ratio to obtain mantle volume percentages consistent with our observations. Simple geometry was used to obtain the radius of the sphere that defined the excavation cavity from the transient cavity diameter and the excavation depth, as shown in Figure 3.1. We calculated the total volume of ejecta and the volume of mantle ejected from all basins in two cases, using average crustal thicknesses of 34 and 43 km from the Gravity Recovery and Interior Laboratory (Wieczorek et al. 2013). Table 3.2 shows these calculations, which resulted in a total volume of 259 $x10^6$ km^3 excavated by the 43 basins, with 32 vol% (crustal thickness 43 km) to 40 vol% (crustal thickness 34 km) of this made up of mantle material.

The signature of this basin ejecta may have been detected in remote sensing data. Ohtake et al. (2009) found highly anorthositic basement rocks ubiquitously exposed in craters of diameters greater than 30 km in the lunar highlands, indicating that craters larger than 30 km in diameter begin to penetrate a pure anorthosite crust through a mixed layer that is by inference approximately 3 km thick (Ohtake et al. 2009). The volume of this hypothesized 3 km mixed layer is 116 x 10^6 km^3, roughly consistent with the total volume of ejecta calculated according to the Spudis (1993) method and suggesting that the upper several km of the Moon could be largely composed of basin ejecta and contain several tens of percent mantle material.

These estimates indicate that the upper several km of the Moon's surface could be composed of basin veneer and provide an upper limit on the amount of mantle present in this layer. However, other authors have arrived at lower estimates for the total volume of ejecta from the lunar basins. Petro and Pieters (2008) used two models (Pike 1974 and Housen et al. 1983) to calculate that cumulative basin ejecta from the 41 lunar multiring basins, excluding SPA, covers the Moon to thicknesses between 100 and 1000 m. These thicknesses are equivalent to a total volume of 3.8 to 38 x 10^6 km^3 of basin ejecta, excluding the contribution of SPA. In order to compare directly to our estimates we calculated the contribution of SPA to the total ejecta volume (SPA contributes 55% of the total basin ejecta volume in our estimate based on the method of Spudis (1993)) and added this proportion back in to the ejecta volume calculated from the thicknesses of

Petro and Pieters (2008) for a total basin ejecta volume ranging from 5.88 to 58.8 x10^6 km^3. These numbers are significantly smaller than those we calculated using the method of Spudis (1993) and are one to two orders of magnitude smaller than the 3 km mixed zone implied by the Ohtake et al. (2009) observations. This allows for the possibility that the upper 3 km zone is not just composed of basin veneer but is instead basin ejecta mixed with a substantial portion of preexisting local crustal material.

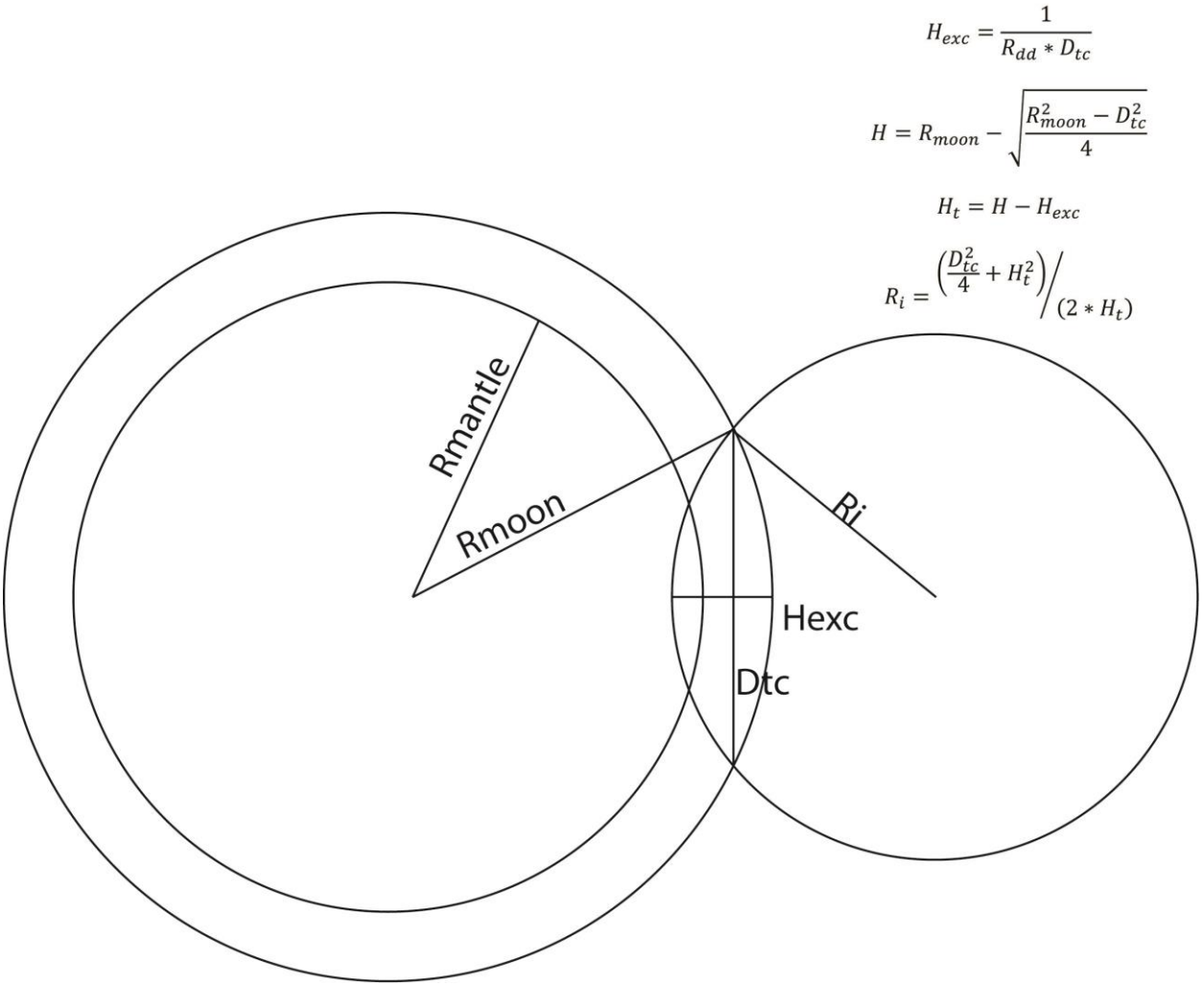

Figure 3.1: Geometry of the excavation cavity as approximated by Spudis (1993). The excavation cavity diameter is defined by the transient cavity diameter (D_{tc}) taken from Petro and Pieters (2008). The depth of excavation, H_{exc}, is defined by an assumed depth/diameter ratio and the transient cavity diameter. The radius of the sphere used to calculate the ejected volume is defined by these parameters. Table 3.2 shows the

transient crater diameters used and the following calculations of total ejected volume and mantle fraction for the 43 lunar basins examined by Petro and Pieters (2008).

To estimate the volume of mantle present in the upper 3 km mixed zone in this low basin ejecta volume case, we scaled our total quantity of basin ejecta to the total basin ejecta volumes from each model used by Petro and Pieters (2008) (5.88 and 58.8 x 10^6 km^3). We scaled our mantle volume ejected (for both 34 and 43 km crustal thickness) by the same factor to obtain a scaled-down total volume of mantle present in the crust if the estimates of Petro and Pieters (2008) better represent the total volume ejected from lunar basins. These values, combined with the total volume of the 3 km mixed zone, result in mantle volume percent in the upper 3 km of 1.67 to 16.7 vol% (43 km crustal thickness) or 2.09 to 20.9 vol% (34 km crustal thickness). Because the differences between the two crustal thickness estimates are much less than the order of magnitude range in ejecta thickness from Petro and Pieters (2008), we simplified the range of mantle volume in the upper mixed zone to between 2 and 20 vol%, both derived from scaling our calculations based on the model of Spudis (1993) to the work of Petro and Pieters (2008).

This wide range of estimates for the contribution of mantle material to the upper mixed zone demonstrates that the question of how much mantle material was excavated by the largest lunar basins is only loosely constrained. We applied each calculated estimate for the volume of mantle excavated (40, 30, 20, and 2 vol%) as upper limits to the mantle ultramafics permitted in each highlands pixel in our mixing models and assessed the plausibility of each result.

Table 3.2. Sample basin ejecta volume calculations. Transient crater dimensions from Petro and Pieters (2004) for all basins except SPA; SPA transient crater dimensions from Spudis (1993). Depth of excavation = 1/10*TC diameter (Spudis 1993). Ejected volume is calculated following the method of Spudis (1993) as described in text. Crustal thicknesses from Wieczorek et al. (2013).

					Crustal thickness=34 km	Crustal thickness=43 km
Basin	Main ring diameter (km)	Mean transient crater diameter estimation (km)	Depth of excavation (km)	Ejected volume (10^6 km^3)	Mantle volume ejected (10^6 km^3)	Mantle volume ejected (10^6 km^3)
South Pole-Aitken	2600	1470	147	127.01	74	62.44
Tsiolkovsky-Stark	700	409	40.9	2.7	0.08	0
Insularum	600	330	33	1.42	0	0
Marginis	580	315	31.5	1.24	0	0
Flamsteed-Billy	570	307	30.7	1.14	0	0
Balmer	500	252	25.2	0.63	0	0
Werner-Airy	500	252	25.2	0.63	0	0
Pingre-Hausen	300	95	9.5	0.03	0	0
Al-Khwarizmi-King	590	322	32.2	1.13	0	0
Fecunditatis	690	401	40.1	2.55	0.06	0
Australe	880	550	55	6.56	0.95	0.31
Tranquillitatis	700	409	40.9	2.7	0.08	0
Mutus-Vlacq	690	401	40.1	2.55	0.06	0
Nubium	690	401	40.1	2.55	0.06	0
Lomonosov-Fleming	620	346	34.6	1.64	0	0
Ingenii	315	107	10.7	0.05	0	0
Poincare	325	115	11.5	0.06	0	0
Keeler-Heaviside	500	252	25.2	0.63	0	0
Coulomb-Sarton	440	205	20.5	0.34	0	0
Smythii	740	440	44	3.36	0.17	0

Lorentz	365	146	14.6	0.12	0	0
Amundsen-Ganswindt	335	122	12.2	0.07	0	0
Schiller-Zucchius	335	122	12.2	0.07	0	0
Planck	325	115	11.5	0.06	0	0
Birkhoff	325	115	11.5	0.06	0	0
Freundlich-Sharonov	600	330	33	1.42	0	0
Grimaldi	440	205	20.5	0.34	0	0
Apollo	480	236	23.6	0.52	0	0
Nectaris	860	534	53.4	6	0.79	0.23
Mendel-Rydberg	420	189	18.9	0.27	0	0
Moscoviense	420	189	18.9	0.27	0	0
Korolev	440	205	20.5	0.34	0	0
Mendeleev	365	146	14.6	0.12	0	0
Humboldtianum	650	369	36.9	1.98	0.01	0
Humorum	425	193	19.3	0.28	0	0
Crisium	740	440	44	3.36	0.17	0
Serenitatis	920	581	58.1	7.73	1.32	0.52
Hertzsprung	570	307	30.7	1.14	0	0
Sikorsky-Rittenhouse	310	103	10.3	0.04	0	0
Bailly	300	95	9.5	0.03	0	0
Imbrium	1160	769	76.9	17.9	5.53	3.45
Schrodinger	320	111	11.1	0.05	0	0
Orientale	930	589	58.9	8.05	1.43	0.58
TOTAL				209.14	84.71	67.53
Vol% mantle of total ejecta					40.50	32.29
TOTAL scaled to 0.1 km thick ejecta				5.88	2.38	1.90
Vol% mantle of total mixed surface layer					2.09	1.67

TOTAL scaled to 10 km thick ejecta				58.77	23.80	18.98
Vol% mantle of total mixed surface layer					20.93	16.68

3.2.3 Rock type distribution calculation

The calculations assigning the major lunar minerals to the rocks made up by these minerals were based around the simplified rock type compositions discussed in the previous sections and followed a standard procedure with different paths followed depending on assumptions regarding the presence and abundance of mantle ultramafics, the rock type to which clinopyroxene was assigned, and the mafic content of anorthosites. The flowchart of Figure 3.2 illustrates the method that is described in the following paragraphs, and Table 3.3 shows the input variables for the different scenarios calculated. 48 possible scenarios exist given these variables; we have calculated rock type abundances for a representative 19 of these scenarios. The results of all paths calculated along with rock type abundance maps for these scenarios can be found in the supplementary material.

Table 3.3. Compositional variable values used in models

Anorthosite mafic content	0	Extreme case: pure anorthite
	2	Ohtake et al. (2009)
	7	Mean of Wieczorek et al. (2006)
	15	Warren (1990)
Upper limit on mantle component in crust	0	Extreme case: no mantle excavated
	2	Housen et al. (1983) via Petro and Pieters (2008)
	20	Pike (1974) via Petro and Pieters (2008)
	30	Spudis (1993), thick crust
	40	Spudis (1993), thin crust
	No limit	Extreme case: all excess mafics attributed to mantle
Cpx limit in mantle	No limit	CPX permitted in mantle
	0	All CPX due to mare basalt

We describe here the process of arriving at rock type abundances through any of the branches of Figure 3.2. We first selected whether to put any mafics into mantle material for the scenario being calculated. If the given scenario did not include mantle ultramafics as a source of mafic material to the highlands, a system of simultaneous unmixing equations were solved for the abundances of anorthosite, norite, troctolite, and

gabbro (or mare basalt). If instead the scenario we chose included a mafic contribution from the mantle, the next step was to determine whether an upper limit would be placed on the total mantle volume permitted. Our mantle volume calculations of the previous section were used as upper limits for the total mantle ultramafic rocks permitted in each pixel; however, we also calculated scenarios in which all excess mafics not in anorthosites were of mantle origin to put an upper limit on the total amount of mantle material the measured mineral distributions could support. If there was no limit on the maximum amount of mantle allowed in a scenario (or path), we next chose whether to permit clinopyroxene in the mantle. The simplest scenarios assigned all three mafic minerals to the mantle in the relative abundances in which they were present in each pixel, allowing us to derive an estimate of mantle composition. However, we also calculated rock abundances assuming clinopyroxene did not originate in the mantle. If clinopyroxene was allowed in the mantle, all plagioclase was assigned to anorthosite, which was completed by adding in the appropriate proportions of the mafics, and the remaining mafics were assigned to dunite and pyroxenite. If clinopyroxene was not permitted in the mantle, simultaneous equations were solved to obtain the abundance of mare basalt and anorthosite, and all excess olivine and orthopyroxene was assigned to dunite and pyroxenite.

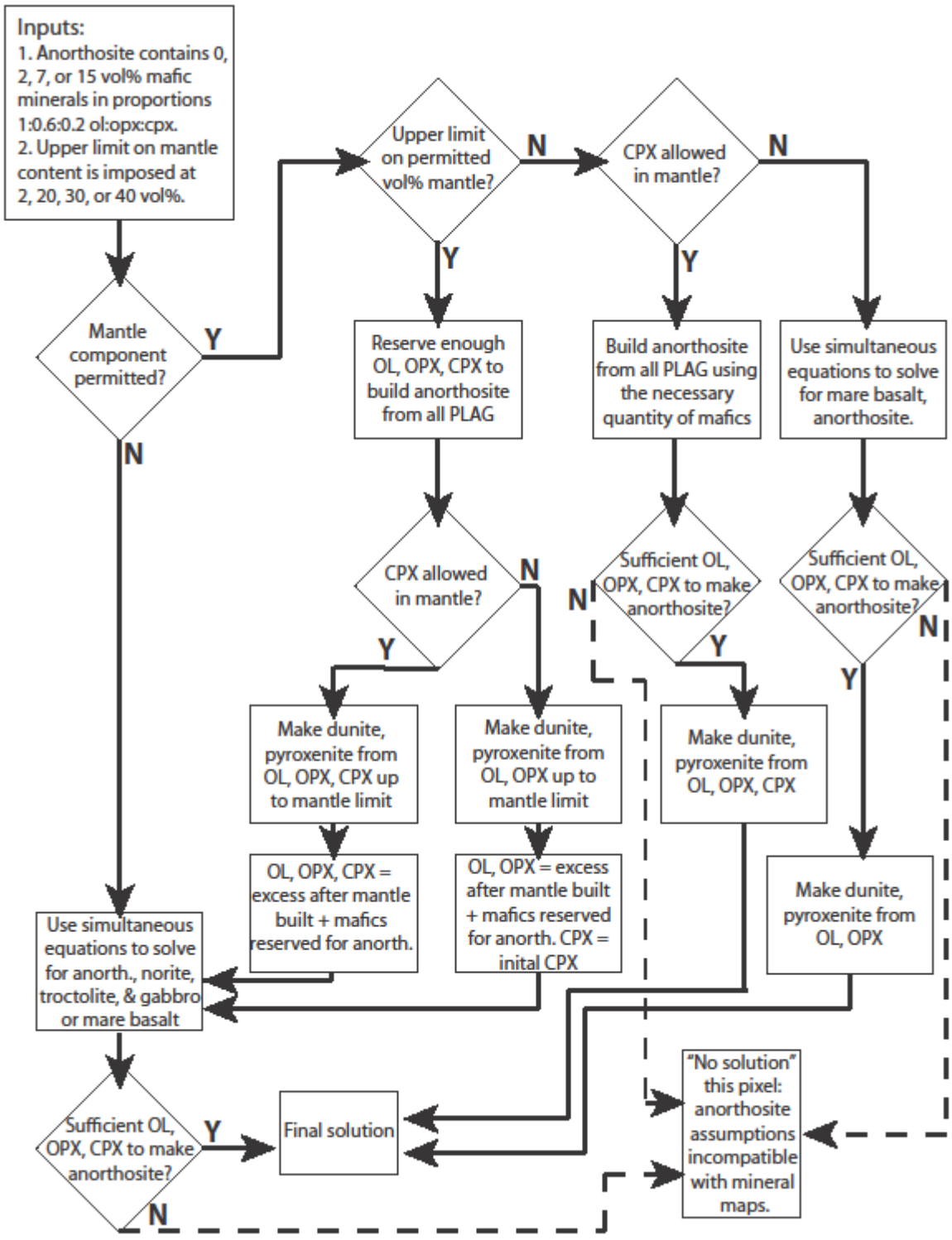

Figure 3.2: Flowchart describing the procedure used to assign detected minerals to

highland rock types for each of the scenarios calculated. A detailed description of the process is located in the accompanying text.

If an upper limit on permitted mantle abundance was imposed (2, 20, 30, or 40 vol% from our basin ejecta calculations), the total amount of mafic material needed to assign all plagioclase to anorthosite of the selected mafic content was subtracted from the mafic material available to work with and reserved. The remaining mafic minerals were incorporated into dunite and pyroxenite up to the upper limit selected. Any excess mafics remaining above the upper limit were added back into the mafic material reserved for anorthosites, and these mafic minerals and the plagioclase abundance were then fed into the system of equations to obtain anorthosite, norite, troctolite, and gabbro (or mare basalt) abundance. If in this scenario clinopyroxene was not permitted in the mantle, all clinopyroxene would be reserved, the mantle would be constructed out of olivine and orthopyroxene, and the excess olivine and orthopyroxene would be incorporated into anorthosite, norite, and troctolite, with the clinopyroxene going into anorthosite and mare basalt.

In every branch of the flowchart, when anorthosite abundance was calculated, any pixel lacking enough of any one mafic mineral to complete the anorthosite (for example, if anorthosites are PAN, any pixel with >98 vol% plagioclase) was assigned "no solution," meaning that the assumptions about anorthosite composition were incompatible with the measured mineral abundances at that pixel. We tracked the percentage and distribution of no-solution pixels for each scenario, as well as the limiting mafic mineral for each pixel, and report only compositions obtained from those pixels where solutions were obtained. It is important to note that while some no-solution pixels were the result of plagioclase abundance too high to permit anorthosite of the mafic content assumed (for example, a pixel containing 95% plagioclase when mafic anorthosites containing 15 vol% mafics are assumed), other no-solution pixels were governed by the relative mafic abundances assumed, so that a pixel with 85% plagioclase could return no solution if olivine, orthopyroxene, and clinopyroxene were not present in the assumed proportions. We calculated the percentage of highland pixels with no-solution results, which provides a measure of how well each set of assumptions about

anorthosite composition agreed with the measured mineral abundances. For the scenarios that included an upper limit on the abundance of mantle material, we calculated percent of pixels in which the mantle abundance fell below the upper limit. This provides a measure of how well each mantle constraint agreed with the measured minerals

3.3 Results and Discussion

Rock abundance maps for one representative scenario are shown in Figure 3.3. For this scenario, anorthosites were assumed to contain 2 vol% mafic minerals ("purest anorthosites" of Ohtake et al. 2009) and the mantle component was limited to a maximum of 2 vol% in keeping with the lower of the basin ejecta estimates of Petro and Pieters (2008) based on the model of Housen et al (1983). Excess mafic material not assigned to anorthosites or mantle was assigned to norite and troctolite in the case of orthopyroxene and olivine, and to mare basalt in the case of clinopyroxene. Only 7% of the highlands surface returned a "no solution" result, indicating that the measured mineralogy of the highlands is generally consistent with anorthosites of PAN composition and with our assumptions about the relative proportions of the mafic minerals in anorthosites. The map of Figure 3.3g) shows the spatial distribution of pixels where our assumptions about anorthosite composition were not in agreement with the mineral maps, as well as the limiting mafic mineral for each pixel (red: orthopyroxene; green: olivine; blue: clinopyroxene). The majority of the "no solution" pixels for this scenario occured in the central farside highlands, which are very plagioclase-rich in the mineral maps of Crites et al. (Chapter 2). The map of Figure 3.3g) demonstrates that in most of the pixels with insufficient mafic minerals to create plagioclase with 2 vol% mafics in the proportions we assume, orthopyroxene was the limiting factor, reflecting an orthopyroxene low in the central farside highlands in the maps of Crites et al. (Chapter 2) that is also apparent in the norite distribution.

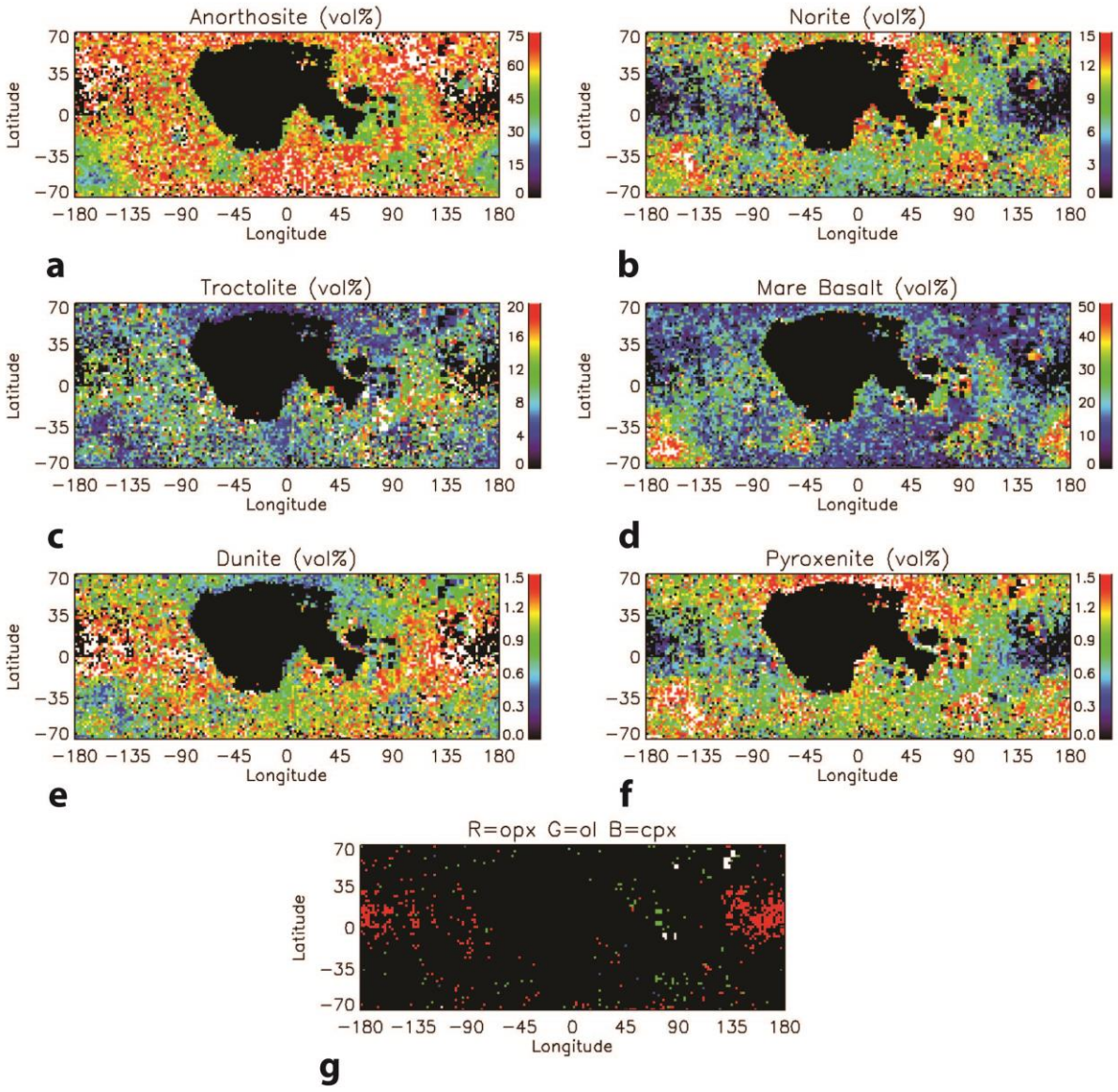

Figure 3.3. Calculated abundances of a) anorthosite; b) norite; c) troctolite; d) mare basalt; e) dunite; f) pyroxenite; g) the limiting mafic mineral for all pixels returning no solution as described in Figure 3.2; for a scenario calculated with purest anorthosites (2 vol% mafic minerals), 2 vol% mantle permitted, and all excess clinopyroxene not assigned to the mantle assigned to mare basalt. The majority of pixels returning no solution were limited by the orthopyroxene required to fulfill our anorthosite mafic composition assumptions in this case. The no-solution pixels were limited to the central farside highlands, an area extremely rich in plagioclase and low in orthpyroxene in the maps of Crites et al. (Chapter 2).

The results of all scenarios taken together are instructive. In particular, in all scenarios that assumed anorthosites contain 15 vol% mafic minerals, 66% or more of highland pixels encounter no-solution, with three-quarters of pixels encountering no-solution in most cases. This suggests that the mafic anorthosites of Warren (1990) are largely not compatible with the measured mineralogy of the highlands, because in the maps of Crites et al. (Chapter 2) many highland pixels contain more than 85 vol% plagioclase.

The average anorthosite abundance was relatively consistent across all scenarios, with the major controlling factor being the rock type containing the mafic minerals. When the majority of mafic minerals were assigned to POI rocks, which require plagioclase, anorthosite abundance was between about 55 and 65 vol%. Alternatively, when the majority of mafics were assigned to the mantle, anorthosite abundance ranged from about 70 to 85 vol%. The total amount of mafic contaminant of the primary magma ocean-derived crust ranged from about 15 vol% if all mafics were in the mantle and anorthosites were mafic, and 45% if all mafics were in post-magma ocean igneous rocks and anorthosites contained little or no mafic material. These results are in good general agreement with the estimate of Warren (1990) that the highlands crust is made up of 45-75% ferroan anorthosite suite rocks, or direct products of the magma ocean, with the rest made up of "Mg-rich" rocks. At present there are few constraints available to differentiate between mantle and igneous rocks for assignment of mafic minerals; however, our basin ejecta calculations provide a starting point for estimating the amount of mafic material that may be assigned to ejected mantle (Figure 3.4).

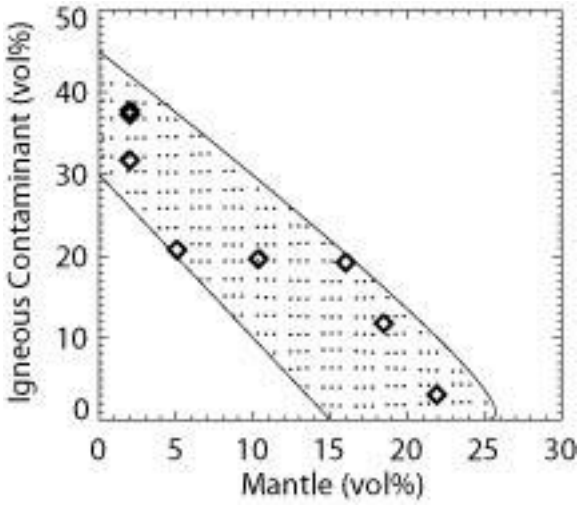

Figure 3.4. Summary of the range of the relative sources of mafic contaminant consistent with the mineral maps of Crites et al. (Chapter 2) (dotted field). Open diamonds show scenarios calculated in this work. "Igneous contaminant" includes the highland rock types norite, troctolite, and gabbro, as well as the mare basalt component assumed in some scenarios.

In the scenarios allowing up to 30-40 vol% mantle (using the Spudis 1993 basin excavation model), from 60 to over 90% of pixels contained less than the maximum amount of mantle allowed, indicating that the data do not support such large proportions of mantle material. The simple ejecta volume calculations based on Spudis (1993) therefore appear to overestimate the amount of mantle excavated compared with the mantle content permitted by measured mineralogy, regardless of other factors such as mafic content of anorthosites. A mantle abundance of about 20 vol% appears more consistent with measured mineralogy: about half of the pixels in these scenarios contained less than 20 vol% mantle. The exception is the case where clinopyroxene was not permitted in the mantle: if the mantle were composed only of olivine and orthopyroxene, very few pixels contained more than 20 vol% mantle. A maximum mantle abundance of 2 vol% (imposed by the lesser basin ejecta thickness model in Petro and Pieters, 2008) required a significant amount of POI and mare basalt rocks in addition to mantle material to account for all mafic minerals, regardless of the mafic content of anorthosites. It is likely that reality reflects some version of this scenario, and the mafic contamination of the lunar highlands is a combination of mantle material, post-magma

ocean igneous rocks, and mare basalt contamination. We have constrained the maximum likely amount of mantle present to less than 20 vol%, or nearer 10 vol% if clinopyroxene is not present in the mantle. With these constraints in mind, we summarize the most plausible mixing model results in Table 3.4.

The percent of mantle material most consistent with the highlands mineralogy is closer to the range of basin ejecta volume calculations based on the ejecta thicknesses of Petro and Pieters (2008) than to our direct geometrical calculation of ejecta volume based on the model of Spudis (1993) chiefly because the latter model emplaces more mafic mantle material than most of the mineral maps can support. A way of reconciling the two estimates is to adjust the depth/diameter ratio of the excavation cavity used in the geometrical ejecta volume calculation. The depth/diameter ratio of 1/10 used by Spudis (1993) is strongly supported for the smaller multiring basins (e.g. Croft 1980, O'Keefe and Ahrens 1993, Wieczorek and Phillips 1999); however, Wieczorek and Phillips (1999) found that for the three largest lunar basins SPA, Imbrium, and Serenitatis, the excavation cavity is significantly shallower based on gravity measurements. The depth/diameter ratio for Serenitatis and Imbrium was found to be near 0.05; for SPA it was near 0.01. As 70% of the total ejecta volume and over 90% of the mantle volume in our calculations was from these three largest basins, the smaller depth to diameter ratio suggested by Wieczorek and Phillips (1999) would have a significant effect on the total volume of mantle expected. Depth/diameter ratios of 0.035 to 0.06 for the excavation cavities of these basins resulted in a range of 2 to 23 vol% mantle in the surface we mapped, and are in better agreement with the mafic mineral abundances mapped than the originally calculated 30-40 vol%.

Table 3.4. Summary of mixing models most consistent with measured mineralogy of the lunar highlands.							
	Description	Mean anorthosite (vol%)	Mean mare basalt (vol%)	Total POI rocks (vol%)	Mantle material (vol%)	Total non-MO rocks (vol%)	% area no solution
Mafics into POI and/or mare basalt	Pure anorthite; all mafics POI	54.87		45.13	0.00	45.13	0.00
	PAN; excess mafics POI	55.69		44.31	0.00	44.31	6.87
	Anorthosites with 7 vol% mafics; excess mafics POI	60.39		39.61	0.00	39.61	18.52
	PAN; excess ol + opx POI; excess cpx mare basalt	58.77	19.43	21.81	0.00	41.23	6.94
Mafics into mantle and/or mare basalt	Pure anorthite; all mafics mantle	75.73		0.00	24.27	24.27	0.00
	PAN; excess mafics mantle	75.50		0.00	23.50	23.50	7.17
Mafics into mantle up to 40%	PAN; mafics to mantle up to 40%; excess ol + opx POI; excess cpx mare basalt	76.54	0.30	0.09	23.07	23.46	51.12
Mafics into mantle up to 30%	PAN; mafics into mantle up to 30%; excess ol + opx POI; excess cpx mare basalt	75.02	2.16	0.92	21.90	24.98	51.71
Mafics into mantle up to 20%	PAN; mafics to mantle up to 20%; excess ol + opx POI, excess cpx mare basalt	69.75	10.33	4.66	18.47	30.25	36.39
	PAN; ol + opx to mantle up to 20%; excess ol + opx into POI; all cpx to mare basalt	69.99	19.39	0.28	10.34	30.01	7.63
Mafics into mantle up to 2%	PAN; mafics to mantle up to 2%; excess ol + opx POI, excess cpx mare basalt	60.22	18.01	19.77	2.00	39.78	7.59
	PAN; ol + opx to mantle up to 2%; excess ol + opx into POI; all cpx to mare basalt	60.73	19.50	17.77	2.00	39.27	8.18

3.4 Implications for Lunar Crust Formation

Our mixing models built from Clementine-based, Lunar Prospector-validated mineral maps allow us to shed light on three possible sources of excess mafic material in the lunar highlands. The maps of Crites et al. (Chapter 2) indicate a plagioclase-rich crust and across much of the highlands our mixing models are more compatible with a magma ocean that produced the pure anorthosites (<2 vol% mafics) detected widely by spectroscopic methods (e.g. Ohtake et al. 2009; Pieters et al. 2009a; Cheek et al. 2013) rather than the mafic anorthosites (15 vol% mafics) suggested by Warren (1990). About 20% of the highlands surface is incompatible with anorthosites containing the intermediate 7 vol% mafics seen on average in lunar samples indicating that although most of the primary anorthosite crust could contain 7 vol% mafics, a significant portion still requires anorthosites of higher purity.

Simple geometric calculations of the amount of mantle that could have been excavated by the lunar multiring basins permit all of the mafic highland material to be derived from mantle ultramafics. However, the assumption about the nature of high Ca pyroxene has a large impact on the model abundance of mantle. When high Ca pyroxene was attributed to mare basalt contamination rather than mantle material, nearly 20 vol% mare basalt material was required in the lunar highlands, and only 10 vol% excavated mantle contaminant was present in the crust. This low mantle abundance implies that the excavation cavity depth/diameter ratio for the largest lunar basins must be in the range of 0.035 to 0.06, a result consistent with the observation of Wieczorek and Phillips that Serenitatis, Imbrium, and SPA do not conform to the trend of a 1:10 depth/diameter ratio seen in smaller basins. These conclusions including the high mare basalt abundance are the result of high clinopyroxene abundance in the maps of Crites et al. (Chapter 2). Lucey et al. (2014) report very little high Ca pyroxene in the lunar highlands, which would eliminate the need for extensive mare basalt contamination in the highlands.

Our mixing models allow us to bracket the average mafic contamination of the primary anorthosite crust to between 15 vol% (if the mafic contamination is entirely composed of ultramafic mantle ejecta) and 45 vol% (if the mafic contamination is a result of post-magma ocean igneous activity producing troctolites, norites, and gabbros or mare

basalt). Figure 3.4 shows the field of mafic contaminant sources consistent with our mineral maps. While mineral abundances permit us to put an upper limit of 10-20 vol% on the amount of mantle material that could reasonably be present in the lunar highlands, additional constraints are needed to determine whether a lower limit can be placed on the mantle contribution (that is, whether any mantle material was excavated) so that the relative contributions of mantle vs. post-magma ocean igneous material can be better understood.

CHAPTER 4

PROTON FLUX AND RADIATION DOSE FROM GALACTIC COSMIC RAYS IN THE LUNAR REGOLITH AND IMPLICATIONS FOR ORGANIC SYNTHESIS AT THE POLES OF THE MOON AND MERCURY

Published as Crites, S.T., Lucey, P.G., and Lawrence, D.J. (2013) Proton flux and radiation dose from galactic cosmic rays in the lunar regolith and implications for organic synthesis at the poles of the Moon and Mercury. Icarus, 226, 1192-1200. doi: 10.1016/j.icarus.2013.08.003

Abstract— Galactic cosmic rays are a potential energy source to stimulate organic synthesis from simple ices. The recent detection of organic molecules at the polar regions of the Moon by LCROSS (Colaprete et al., 2010), and possibly at the poles of Mercury (Paige et al. 2013), introduces the question of whether the organics were delivered by impact or formed in situ. Laboratory experiments show that high energy particles can cause organic production from simple ices. We use a Monte Carlo particle scattering code (MCNPX) to model and report the flux of GCR protons at the surface of the Moon and report radiation dose rates and absorbed doses at the Moon's surface and with depth as a result of GCR protons and secondary particles, and apply scaling factors to account for contributions to dose from heavier ions. We compare our results with dose rate measurements by the Cosmic Ray Telescope for the Effects of Radiation (CRaTER) experiment on Lunar Reconnaissance Orbiter (Schwadron et al., 2012) and find them in good agreement, indicating that MCNPX can be confidently applied to studies of radiation dose at and within the surface of the Moon. We use our dose rate calculations to conclude that organic synthesis is plausible well within the age of the lunar polar cold traps, and that organics detected at the poles of the Moon may have been produced in situ. Our dose rate calculations also indicate that galactic cosmic rays can induce organic synthesis within the estimated age of the dark deposits at the pole of Mercury that may contain organics.

4.1 Introduction

Galactic cosmic rays (GCR) are energetic charged particles, predominantly protons, which originate outside the solar system and though mediated by the solar

magnetic field retain energies from a few MeV to much greater than 100 GeV per nucleon at the orbit of the Earth (Longair, 1992). When these particles encounter the regolith of an airless body like the Moon, they interact with the surface materials and release cascades of secondary particles including neutrons and gamma rays that exit the surface and are diagnostic of the surface composition. Neutron and gamma ray spectrometers have made use of this process to study the surface composition of many bodies including the Moon (e.g. Feldman et al., 1999; Mitrofanov et al., 2010), Mars (e.g. Boynton et al., 2004), Mercury (Goldsten et al., 2007), and Vesta (Prettyman et al., 2003). Experiments have also shown that proton irradiation can stimulate organic synthesis in simple C, H, O, and N-bearing ices, and as a result GCR protons have been cited as a possible energy source for organic production on comets, icy satellites, and interstellar ices (e.g. Moore et al., 1983; Hudson and Moore, 1995; Moore and Hudson, 1998, 2003; Gerakines et al., 2001).

It has also been suggested that GCR proton irradiation could provide an energy source to stimulate organic synthesis at the lunar poles (Lucey, 2000), since many of the same cometary ices studied in experiments may also be present at the lunar polar cold traps (e.g. Zhang and Paige, 2009; Colaprete et al., 2010; Gladstone et al., 2012; Paige et al., 2010). This process is also relevant to Mercury's poles, where extensive water ice deposits are thought to be present at permanently shaded regions, covered in some areas by an organic-rich surface deposit (Lawrence et al., 2013; Neumann et al., 2013; Paige et al., 2013). We investigate the possibility of radiation-induced organic synthesis at the lunar poles by modeling the proton flux within the lunar surface to determine whether the proton flux is high enough to accumulate radiation doses equivalent to those determined experimentally (Moore and Hudson, 1998) to stimulate organic synthesis, within the probable age of the lunar polar cold traps.

4.2 Methods

We use the radiation transport code MCNPX 2.6.0 (Monte Carlo N-Particle eXtended) (Pelowitz, 2008) to model the flux of GCRs at the lunar surface and the resulting radiation dose accumulated in the regolith. MCNPX is a Monte Carlo radiation transport code created by the Los Alamos National Laboratory and is the result of several

decades of development. Monte Carlo methods track the behavior of many individual particles from source to termination to provide information about the average behavior of particles in the system for tallies of interest to the user (e.g. proton flux through a surface or energy deposition in a material). The method is well suited to three-dimensional, time-dependent problems and is especially useful for statistical processes like nuclear interactions with materials. MCNPX has the ability to track the interactions of 34 types of particles including protons, neutrons, light ions up to alpha particles, and 2205 heavy ions up to ^{259}Fm, in three dimensions and at energies up to 1 TeV/nucleon. Stopping power algorithms have been validated against the SRIM software (James et al., 2006; Ziegler et al., 2003). It uses continuous cross-section data to model interactions up to 150 MeV, and physics models for interactions beyond this energy range (Pelowitz, 2008). It is a general-purpose code that is widely used for interpretation of planetary neutron and gamma ray spectroscopy (e.g. Prettyman et al., 2006; Lawrence et al., 2006, 2010), as well as in the fields of medical physics, high-altitude radiation dose modeling, spent nuclear fuel storage, and for many other applications (e.g. Newhauser et al., 2005; Anid et al., 2009; Hordósy, 2005). The code is accessible at no cost from the Radiation Safety Information Computational Center (RSICC) at Oak Ridge National Laboratory (rsicc.ornl.gov).

The MCNPX code includes among its inputs the energy spectrum and flux of the source, in this case, GCRs. The GCR energy spectrum is modified by interactions with magnetic fields created by solar plasma, which varies with solar activity (Castiglioni and Lal, 1980) so we include assumptions about the sun's activity in our calculations. These effects have been described in analytical form by Castagnoli and Lal (1980) and Masarik and Reedy (1996) who incorporate a modulation parameter, ϕ, to describe the energy loss by GCR particles as a result of solar magnetic field effects. In this parameterization, a larger value of ϕ means a more active sun and lower GCR flux. McCracken and Beer (2007) have shown using a combination of cosmogenic ^{10}Be, neutron monitoring, and instrumental cosmic ray data that GCR fluxes and energy levels have been lower on average during the past 50 years of measurement of the GCR flux via neutron monitors than over the previous 580 years, and Castagnoli and Lal (1980) suggest that a solar

modulation parameter as low as ϕ=100 MV would be a conservative estimate for the modulation expected in solar minimum periods. We selected a solar modulation parameter of ϕ=300 MV, the lowest modulation measured by neutron monitors since the 1960s (Castagnoli and Lal, 1980), as an approximate proton flux from GCR at the Moon over solar system history.

The model also requires the source particle type. Galactic cosmic rays consist mostly of protons, but also feature up to 12% alpha particles and a much smaller percentage of heavier nuclei (Simpson, 1983; McKinney et al., 2006). We model the GCR flux as protons alone for our most basic simulations, and scale the proton flux up to account for the contribution of alpha particles for a second set of simulations (Dagge et al., 1991; Masarik and Reedy, 1996; McKinney et al., 2006). For protons alone, since the input energy spectrum is normalized per source nucleon, we scale our input using a proton flux of 5 protons/cm^2-s for ϕ =300 from McKinney et al. (2006). For the simulations including the effects of alpha particles, we followed the procedure described by McKinney et al. (2006) and multiplied the alpha particle flux for ϕ =300 (0.68 alpha particles per cm^2-s, obtained assuming 88% protons and 12% alpha particles and a proton flux of 5 protons/cm^2-s) by 3.8 before adding this number to the proton flux for a final scale factor of 7.6 particles/cm^2-s. The final scale factor was obtained using the equation $flux_{a,protons} = protons + 3.8*alpha_{eff}$, where $alpha_{eff} = protons*12/88$. An additional normalization factor of ¼ was included in both sets of simulations to account for the particularities of defining a 4π source in MCNPX (McKinney et al., 2006). Figure 4.1 shows our input energy spectrum for GCR protons with ϕ =300, compared with measurements of the cosmic ray proton flux from the BESS spectrometer in 1997 with ϕ=491 (Shikaze et al., 2007).

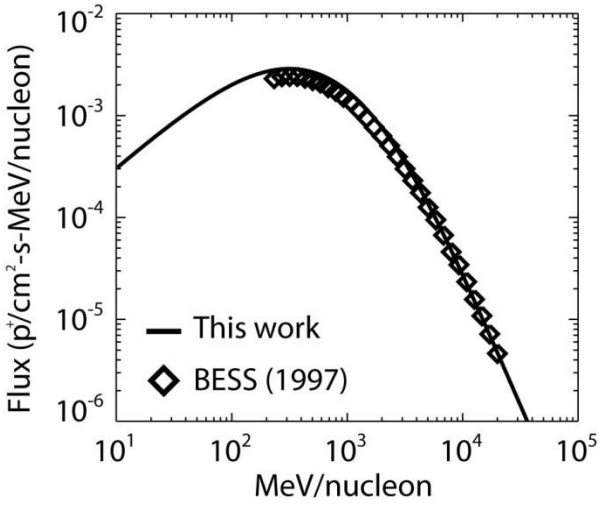

Figure 4.1: Input energy spectrum of protons with ϕ=300 used in our simulations. Boxes indicate the data points for measurements of the energy spectrum of the cosmic ray proton flux by the BESS spectrometer in 1997 (Shikaze et al., 2007). Small differences in the energy spectrum result from the higher modulation (ϕ=491) of cosmic rays at the time of the BESS measurements.

Table 4.1: Elemental abundances for FAN soil composition used in this study	
Element	Weight fraction
O	0.4560
Na	0.004452
Mg	0.005065
Al	0.1763
Si	0.2066
Ca	0.1359
Ti	0.0008
Fe	0.0148

The final model input was the body of the Moon, modeled as a uniform sphere of radius 1737 km composed of ferroan anorthosite (FAN). Table 4.1 shows the chemical makeup used, similar to that used by Lawrence et al. (2006), Elphic et al. (2000), and others. The density of FAN regolith in the simulations was 1.8 g/cm^3, the upper limit of in-situ bulk density at the Apollo 16 site as estimated by Mitchell et al. (1972) from core tube measurements. Results were returned in quantities of flux (protons/cm^2-s) and energy deposition rate per unit volume (MeV/cm^3-s).

4.3. Results

4.3.1 Simulation results

Because the ice content of the lunar polar cold traps is unknown, and because of the known strong effect of water ice on moderation of neutrons (Feldman et al., 1993), we model the effects of GCR on FAN regolith containing percentages of H_2O varying from 0 wt% to 30 wt%. Figure 4.2a-b shows the proton flux in a dry lunar regolith along with two wet cases with 3 wt% and 30 wt% H_2O. Figure 4.2c-d shows similar plots for dose rate in units of centiGrays (cGy) per year (1 Gray= 1 J/kg). The conversion to these units from the MCNPX output in units of MeV/cm^3-s is based on simple stoichiometry and uses the density of the material used in the simulations (1.8 g/cm^3 for FAN, 1.76 g/cm^3 for FAN with 3 wt% H_2O, and 1.45 g/cm^3 for FAN with 30 wt% H_2O) for the medium in which the dose is deposited. We find that the water content of the regolith does not affect the proton flux as it drops off with depth into the regolith significantly. The magnitude and shape of the dose rate profile with depth is also not strongly affected by the water content. However, to capture small effects of water content on dose rate, we will use the dose deposited in ice for a range of regolith water contents to bracket the likely dose experienced by ices present at the lunar polar cold traps.

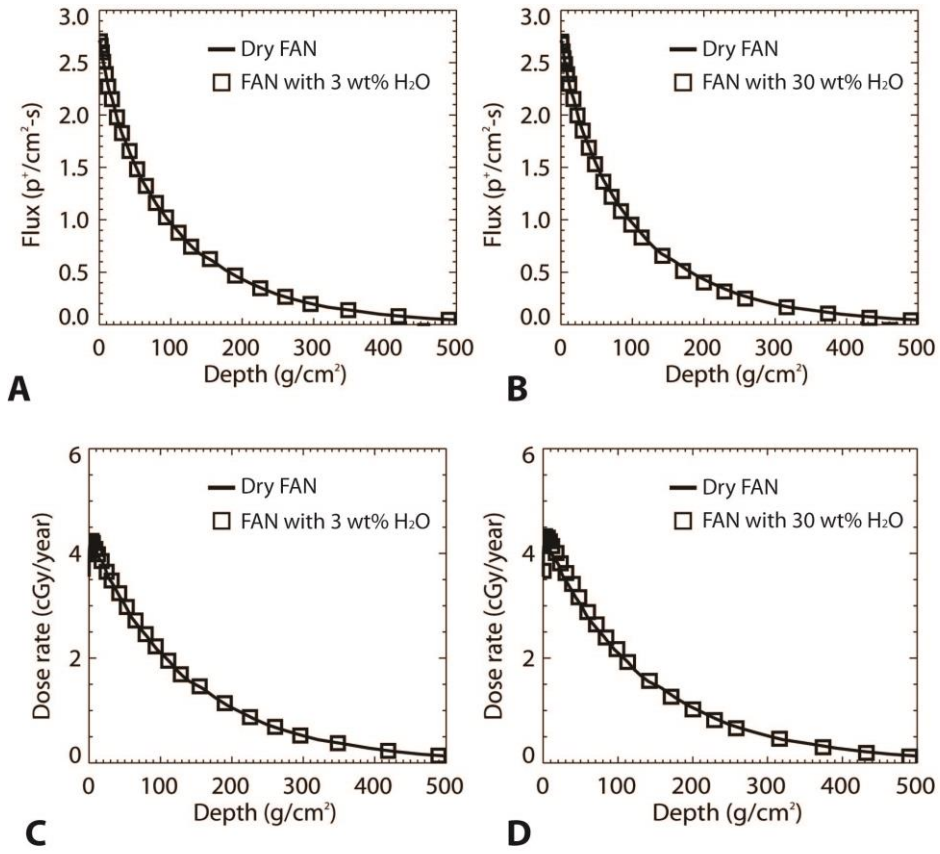

Figure 4.2a,b: Proton flux from GCRs in dry FAN (solid line; density 1.8 g/cm^3) compared with FAN and 3 wt% H_2O (**a**, open boxes; density 1.76 g/cm^3) or FAN and 30 wt% H_2O (**b**, open boxes; density 1.45 g/cm^3). **4.2c,d:** Dose rate from GCR protons in dry FAN (solid line) compared with FAN with 3 wt% H_2O (**c**, open boxes) or FAN with 30 wt% H_2O (**d**, open boxes). Solid lines do not connect the boxes, but show results from separate, water-free models.

In addition to single-layer models of the Moon, we also ran simulations with a two-layer model consistent with that proposed by Lawrence et al. (2006), in which a wet layer containing 200 ppm to 40 wt% H_2O is overlain by a dry FAN layer 10 +/- 5 cm thick, and simulations of cases in which a thin layer with 22 wt% H_2O (the maximum quantity that could be present in the optical surface inside Shackleton Crater, from Zuber et al., 2011) is present in a layer of varying thickness (1 mm to 1 m) at the surface with dry FAN beneath it. We do not consider surface ice layers thinner than 1 mm because of the conclusion of Morgan and Shemansky (1991) that photoionization by H Lyα would

erode surface ice deposits faster than they could accumulate. As Figure 4.3 shows, the effects on the dose rate of varying the geometry of the wet and dry layers is relatively small. However, since dose rate in all cases drops off rapidly with depth in the regolith, the location of the wet layer is important in that an ice buried deeper than about 20 g/cm^2 (about 11 cm assuming a density of 1.8 g/cm^3, or 13 cm assuming a density of 1.45 g/cm^3) is exposed to a lower dose rate than at the surface, and would take longer to accumulate the required dose for organic synthesis.

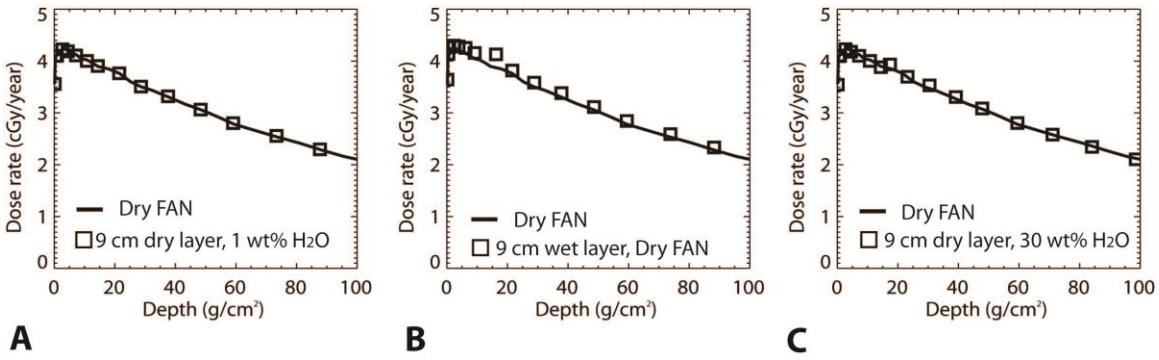

Figure 4.3: Dose rate from protons in dry FAN (solid line; density 1.8 g/cm^3) compared with dose rate from protons in **a:** 9 cm thick dry layer underlain by a wet layer containing 1 wt% H_2O (open squares; density 1.79 g/cm^3). **b:** a 9 cm thick surface layer containing 22 wt% H_2O (density 1.53 g/cm^3) underlain by a dry FAN layer (open squares); and **c:** a 9 cm thick surface dry layer underlain by a layer with 30 wt% H_2O (open squares).

Results were returned for proton flux through a series of concentric spherical shells at increasing depth beneath the Moon's surface in units of protons/cm^2-s, for energy deposition in units of MeV/g-s, and through a more finely spaced spherical mesh beneath the Moon's surface for both flux and energy deposition in units of protons/cm^2-s and energy deposition in units of MeV/cm^3-s, respectively. Spacing for the spherical mesh ranged from 1 mm just below the Moon's surface to 20 cm at depths from 178 to 578 cm. Simulations used 100,000 source particles. Only results with flux errors and energy deposition errors less than 10% were permitted, with most less than 5%.

For a comparison to prior measurements discussed in section 4.3.2, Figure 4.4 shows dose rates including both primary and all types of secondary particles in dry FAN

from simulations beginning with a GCR source consisting of protons only and from simulations scaling source protons to account for the contribution of alpha particles, both in units of centiGrays (cGy) per year (1 Gray= 1 J/kg).

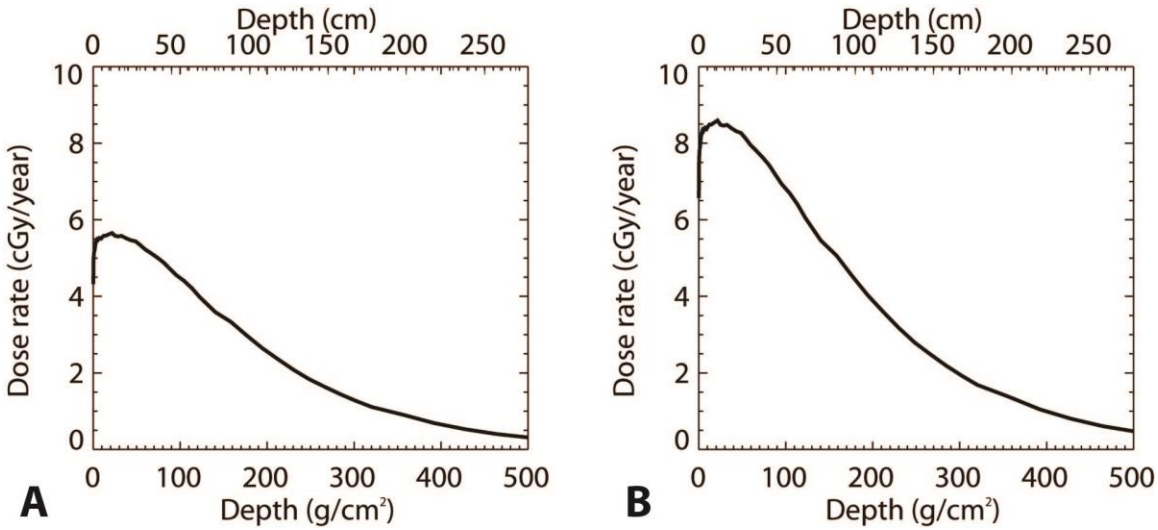

Figure 4.4a: Dose rate in units of cGy/year (1 Gy = 1 J/kg) as a function of depth in dry FAN (density 1.8 g/cm^3), taking into account GCR protons and all secondary particles. **4.4b:** Dose rate (cGy/year) from GCR protons, alpha particles, and secondary products.

4.3.2 Validation of particle transport model

The Cosmic Ray Telescope for the Effects of Radiation (CRaTER) experiment on Lunar Reconnaissance Orbiter measured GCR dose rates at the Moon in order to characterize its biological impact (Spence et al., 2010). These results provide a measurement with which to compare our simulation results. CRaTER's measured maximum dose rate of 11.7 cGy/yr (Schwadron et al., 2012) includes contributions from all species with the possible exception of neutrons and is altitude-adjusted to the lunar surface (Spence et al., 2010). For comparison to CRaTER measurements, we scale the dose rate at the lunar surface obtained from our simulations to take into account the contribution from heavy ions as well as that of protons and alpha particles. GCR heavy ions are much less abundant than protons, but because the energy loss of charged particles is proportional to Z^2 (the square of the atomic number) iron alone deposits up to 24% as much dose as protons, with the other heavy ion species together (i.e. C, N, O, Ne,

Mg, Si) depositing approximately as much as iron (Hayatsu et al., 2008). We therefore include an approximation of the contribution of heavy ions by scaling the surface dose rate from protons (4.32 cGy/yr from Figure 4.4a) by 50% and adding this number to the surface dose rate from protons and alpha particles (6.57 cGy/yr from Figure 4.4b) for a dose rate from all GCRs and secondary particles of 8.73 cGy/yr. Our surface dose rate is lower than the CRaTER result, and falls slightly outside the standard deviation from the average from CRaTER. These differences may stem from our simple scaling to include heavy ions, which does not necessarily account for all the physical processes related to heavy ion interactions in the lunar soil. However, our results are within 25% of the CRaTER results and suggest that MCNPX can be applied to studies of the general radiation environment at the Moon over lunar history when the modest difference between measurement and model is taken into account.

4.4. Discussion

4.4.1 Synthesis of modeling results with experiments

The poles of the Moon and Mercury are unique environments. Urey (1952) was the first to point out that topographic lows in the lunar polar regions would be permanently shaded from sunlight because of the small lunar obliquity and could reach temperatures cold enough to condense and retain volatiles. Watson et al. (1961) developed a model of volatile transport and trapping in these permanently shadowed regions, a concept revisited and expanded by Arnold in 1979. In the 1990s more detailed temperature models were developed for shaded craters at the lunar poles that predicted temperatures below 50 K in some of these regions (Ingersoll et al., 1992; Salvail and Fanale, 1994; Vasavada et al., 1999). In 2010 the Diviner Lunar Radiometer confirmed the extreme cold of polar permanently shadowed regions on the Moon, measuring daytime surface temperatures inside some craters as low as 29 K (Paige et al., 2010). The temperatures measured by Diviner make the Moon's permanently shadowed regions some of the coldest locations in the solar system, in the same temperature range as comets, outer solar system moons, and Pluto, sufficiently cold to trap species as volatile as CO_2 (Vasavada et al., 1999). Given the almost certain impact of many comets on the Moon, it is therefore plausible that the simple ices required as an ingredient for

production of organics are present in lunar polar cold traps. Evidence for polar ice continues to accumulate, including radar observations (Nozette et al., 1996; Spudis et al., 2010) and neutron spectrometer results (Feldman et al., 1998; Mitrofanov et al., 2010).

The LCROSS mission detected organic molecules including C_2H_4, CH_3OH, and CH_4 at the lunar polar regions in 2010 (Colaprete et al., 2010), raising the question of the origin of these organics, and recent work suggests that Mercury's poles may also contain organics in the form of dark deposits (Lawrence et al., 2013; Neumann et al., 2013; Paige et al., 2013). Zhang and Paige (2009) previously suggested that organic molecules could be deposited in the polar regions by migration of volatiles from cometary or meteoritic impactors. In-situ production of organics from galactic cosmic ray protons interacting with simple polar ices was suggested by Lucey (2000), but no calculations were presented. By comparing our simulations of proton fluxes at the poles of the Moon with experiments in low-temperature organic synthesis from proton irradiation, we can test whether the flux of cosmic rays is high enough to stimulate organic synthesis on the Moon within the age of the cold traps, assuming the presence of simple cometary ices analogous to the laboratory experiments of Moore and Hudson (1998).

The production of organic compounds by proton irradiation processing has been studied by many researchers (e.g. Moore et al., 1983, 2001; Delitsky and Thompson, 1987; Johnson, 1989; Delitsky and Lane, 1997; Moore and Hudson, 1998, 2003; Hudson and Moore, 1999; Gerakines et al., 2001). Moore and Hudson (1998) performed experiments exploring organic synthesis in mixtures of H_2O ices mixed with simple ices including CH_4, which was one compound identified by LCROSS in the lunar polar regions. They irradiated thinly-deposited ice layers at temperatures below 20 K with a beam of 0.8 MeV protons. Moore and Hudson found that changes to the organic species present occurred after a dose as low as 1 eV/molecule, and after a dose of 10 eV/molecule all of the organic species that would be synthesized in the experiment had begun to appear. Production rates leveled off after a dose of about 17 eV/molecule, or a beam fluence of 1.5×10^{15} p^+/cm^2 (Moore and Hudson, 1998). Moore et al. (2001) note that 9 eV/molecule is a typical radiation dose for laboratory experiments in radiation processing of simple ices to form organics, but IR-visible changes in the molecules

present begin to appear after a dose of only 1 eV/molecule. We will take a dose of 1 eV/molecule to be sufficient to begin to stimulate organic synthesis, but will also report the time required to accumulate a dose of 10 eV/molecule as a more conservative estimate.

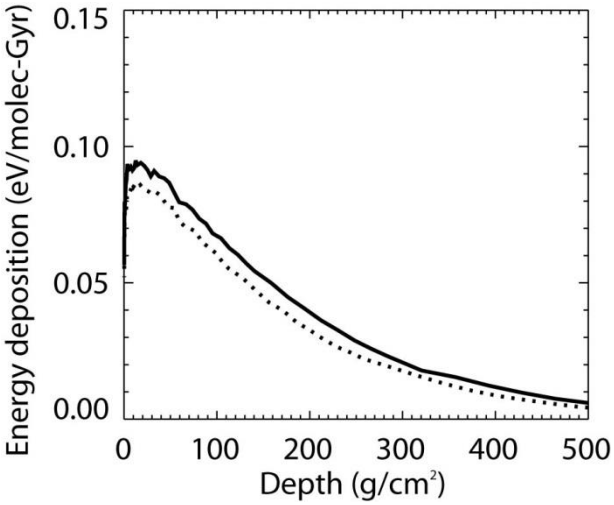

Figure 4.5: Energy deposition by protons in water ice falling in the energy range 0.1 to 1 MeV for a regolith containing 0.1 wt% H_2O (solid line; density 1.8 g/cm^3) and a regolith containing 30 wt% H_2O (dotted line; density 1.45 g/cm^3). This energy band of protons is used to compare directly to organic synthesis experiments by Moore and Hudson (1998) using a 0.8 MeV proton beam.

Our simulations calculate the dose rate per unit volume of regolith with varying water contents. These calculations allow us to determine the time that would be required to accumulate a dose per unit volume which would be sufficient to stimulate organic synthesis if the volume studied is composed of ice of the proper composition. In order to compare directly to experiments, we calculate the energy deposition from protons in the lunar regolith in a band of protons of energies between 0.1 and 1 MeV (to approximate the 0.8 MeV proton beam of Moore and Hudson's experiments). Figure 4.5 shows energy deposition with depth by the protons in this energy range in units of eV/molecule-Gyr, assuming deposition in water ice. Because the actual water content of the regolith in the lunar cold traps is unknown, we show dose deposited for two endmember cases, that of a regolith with 0.1 wt% water ice and that of a regolith with 30 wt% water ice. We

obtain the dose deposited solely in the water ice present by multiplying the dose rate per unit volume by the ratio of the density of water ice (1 g/cm^3) to the average density of the water-bearing regolith (1.45 g/cm^3 for 30 wt% H_2O and 1.8 g/cm^3 for 0.1 wt% H_2O). We then multiply this dose per unit volume of water ice by the inverse of the density of water ice (1 g/cm^3), a conversion factor from g to amu (1 g = 1.6022e23 amu), and assume 18 amu per water molecule. We convert to eV per molecule of water in order to compare to the doses given by experimenters in eV/molecule. H_2O was the most abundant volatile detected by LCROSS (Colaprete et al., 2010), so we assume that this would be the dominant molecule in any simple ices that would be irradiated at or within the lunar surface.

The peak in energy deposition rate with depth for protons in water in this narrow energy band ranged from 0.095 eV/molecule-Gyr for regolith containing 0.1 wt% H_2O to 0.087 eV/molecule-Gyr for regolith containing 30 wt% H_2O, resulting in a period ranging from 10.5 to 11.6 Gyr needed to accumulate a dose of 1 eV/molecule, or more conservatively, 105 to 116 Gyr to accumulate a dose of 10 eV/molecule. This provides an upper limit for the time needed to stimulate organic synthesis, since it takes into account only the protons with energies near 1 MeV and neglects the much more abundant higher energy protons, as well as alpha particles and heavy ions. Figure 4.6 shows energy deposition from protons of all energies, with peak values of 7.90 eV/molecule-Gyr for regolith containing 0.1 wt% H_2O and 8.07 eV/molecule-Gyr for regolith containing 30 wt% H_2O, which allows us to calculate a best estimate of the time range needed to accumulate 1 eV/molecule and stimulate organic synthesis of 0.124 to 0.127 Gyr. Even after taking into account the 25% uncertainty that may be present due to the mismatch between our model results and the CRaTER measurements discussed in section 4.3.2, this time period is well within the 1-2 Gyr age of the cold traps estimated by Arnold (1979).

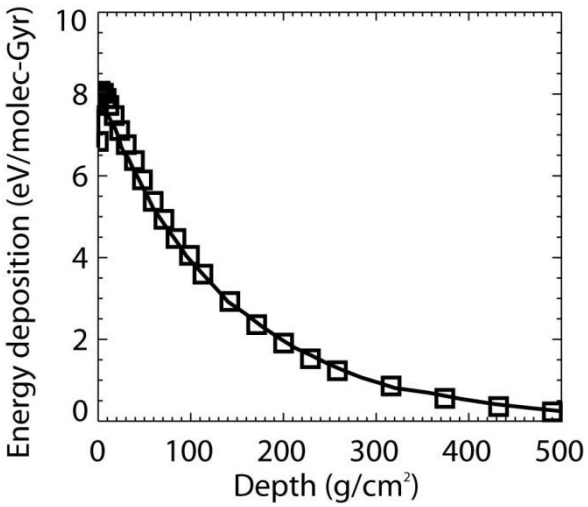

Figure 4.6: Energy deposition in water ice by all protons in the lunar regolith as a result of GCR irradiation for a regolith containing 0.1 wt% H_2O (solid line; density 1.8 g/cm^3) and a regolith containing 30 wt% H_2O (open boxes; density 1.45 g/cm^3). These results can be used to calculate a best-estimate time of 0.124 to 0.127 Gyr required for a dose of 1 eV/molecule to accumulate, enough for organic synthesis to begin taking place at the lunar polar cold traps.

If we take into account the dose contribution from alpha particles in addition to protons, as shown in Figure 4.7, the maximum dose rates increase to 12.0 eV/molec-Gyr for regolith with 0.1 wt% H2O and 12.3 eV/molec-Gyr for regolith with 30 wt% H_2O, requiring only 0.81 to 0.82 Gyr to reach a dose of 1 eV/molecule. Finally, scaling the proton dose by 50% and adding to the dose from protons and alpha particles as described in Section 4.3.2, we can obtain a maximum dose from protons, alpha particles, and heavy ions of 16.0 to 16.3 eV/molec-Gyr, and a time period of only 0.061 to 0.063 Gyr to acquire a dose of 1 eV/molecule and stimulate organic synthesis. However, without experiments to guide our understanding of the organic production by heavy ions, our best estimate for the time required remains in the range of 0.124 to 0.127 Gyr from the maximum energy deposition of 7.90-8.07 eV/molec-Gyr from protons alone. Table 4.2 summarizes the energy deposition rates and times required to accumulate key doses for organic synthesis. The mismatch between our model and the measurements from CRaTER discussed in section 4.3.2 indicate that an uncertainty of about 25% should be applied to our time estimates.

The depth at which ice is present influences the exposure durations needed for organic synthesis, but there are constraints on the near surface ice abundance. Lawrence et al. (2006) show that the Lunar Prospector neutron data are consistent with the detected hydrogen being overlain by a H-free layer of approximately 10 cm depth. Gault et al. (1975) suggest that the upper 10 cm would be overturned by micrometeorite bombardment multiple times in 1 Gyr, a conclusion consistent with the Lawrence et al. (2006) result assuming regolith overturn contributes to desiccation of the uppermost layer.

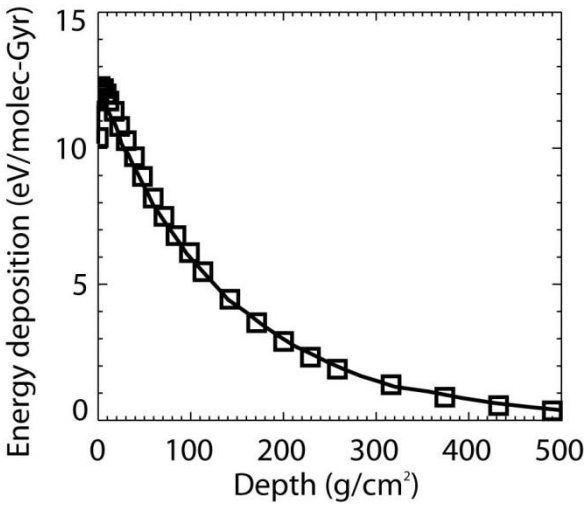

Figure 4.7: Energy deposition in water ice by protons and alpha particles in the lunar regolith as a result of GCR irradiation for a regolith containing 0.1 wt% H_2O (solid line; density 1.8 g/cm^3) and a regolith containing 30 wt% H_2O (open boxes; density 1.45 g/cm^3).

Maximum energy deposition rates lie within this possibly desiccated layer. For the 1 MeV energy band of protons (Figure 4.5) with our minimal ice case of 0.1 wt% H_2O, the maximum deposition occurs 12.6 g/cm^2 below the surface, or about 7 cm for a regolith of density near 1.8g/cm^3; for protons of all energies (Figure 4.6), the peak is shallower at 2.7 g/cm^2 depth (1.5 cm for ρ=1.8 g/cm$^{3)}$. However, dose rates are high enough when including protons of all energies (Figure 4.6) that ice within 59 g/cm^2 of the surface (33 cm for ρ =1.8 g/cm^3) would accumulate a dose of 10 eV/molecule from protons over the estimated 2 Gyr age of the cold traps. Ices within 392 g/cm^2 (218 cm for

ρ =1.8 g/cm^3) could accumulate the minimum dose for organic synthesis of 1 eV/molecule over 2 Gyr. So, while maximum doses occur within the suggested desiccated uppermost layer, doses at greater depths are still sufficient for organic synthesis.

Table 4.2: Summary of maximum energy deposition and time to accumulate key doses for organic synthesis

Source	Regolith water content (wt%)	Maximum energy deposition (eV/molecule-Gyr)	Time to accumulate dose of 1 eV/molecule (Gyr)	Time to accumulate dose of 10 eV/molecule (Gyr)
Protons, 0.1 to 1 MeV	0.1	0.095	10.5	105
	30	0.087	11.6	116
Protons, all energies	0.1	7.90	0.127	1.27
	30	8.07	0.124	1.24
Protons and alpha particles	0.1	12.0	0.082	0.82
	30	12.3	0.081	0.81
Protons, alpha particles, and heavy ions	0.1	16.0	0.063	0.63
	30	16.3	0.061	0.61

4.4.2 Possible organic yields from GCR protons

Most experiments in organic production report the yield, or G-value, with units of product molecules created per 100 eV of energy deposited to describe the efficiency of the conversion process. These values can be used to explore the range of possible products in planetary settings (Delitsky and Thompson, 1987; Delitsky and Lane, 1997, 1998). Following the calculations of Schwadron et al. (2012) and Johnson (1989) and using experimentally determined yields (G, product molecules per 100 eV absorbed) from Moore and Hudson (1998), Hudson and Moore (1995) and Gerakines et al. (2001),

we calculate the fraction of altered material, F, accumulated over time period t (Gyr) with dose rate D (eV/molecule-Gyr) using equation 1:

$$F = 1 - exp(-DGt) \quad (1)$$

Table 4.3 summarizes our calculations for products that could be formed in 1 Gyr by our maximum proton dose rate of 7.9 eV/molecule-Gyr for regolith containing 0.1 wt% H_2O. The results of Table 4.3 demonstrate that up to 6% of source volatile compounds (in this example, H_2O + CO_2 + CH_4 ice) could be converted to organic products (in this case, C_2H_6) during radiation processing of polar cold traps. In other words, for every kg of source ice, 60 g of C_2H_6 would be created in 1 Gyr of irradiation. With possible yields this high, it is clear that in-situ organic synthesis could significantly change the compositional makeup of polar cold traps.

Our comparison to experimental results (Table 4.3) shows that a wide range of organics can be produced from the ingredients detected by LCROSS at Cabeus Crater. A wide variety of organic compounds can be formed even beginning with the assumption that the Moon's polar cold traps contain only relatively simple ices, for example one composed of only water and CO_2 (Delitsky and Lane, 1999). Zhang and Paige (2009) showed that many organic compounds, such as aromatic hydrocarbons, linear amides, and carboxylic acids that could be produced at the lunar poles or delivered by impacts are less volatile than water, and would remain available for continued processing. An even wider range of products can be produced by incorporating a larger number of starting compounds that could be reasonably expected to be cold trapped at the Moon's poles from source considerations (Arnold 1979) and temperature modeling (Vasavada et al., 1999; Zhang and Paige, 2009).

It is important to note that the initial ice composition and relative ratios of components affect the resulting yield of products. Moore and Hudson (1998) found that both the radiation products synthesized and the relative abundances of products were dependent on initial ice composition, so organic abundances in Table 4.3 should be taken as guide to possible species and abundances, not a specific prediction.

Table 4.3: Calculations of some selected potential organic products for the lunar polar cold traps based on doses from this simulation and G-values (in units of molecules altered per 100 eV absorbed) from experiments. Calculations are for our best estimate dose of 7.9 eV/molec-Gyr and an elapsed time period of 1 Gyr. G-values are from: [1]Gerakines et al. 2001; [2]Moore and Hudson 1998; [3]Hudson and Moore 1995. [4]Percent altered is calculated following methods of Schwardron et al., 2012 and Johnson, 1989 using the formula: $\% \, altered = 100 \times [1 - exp(-DGt)]$.

Starting compound	Product	G-value	Percent altered[4]	Grams of product for 1 kg starting ice
$H_2O + CO_2 + CH_4$	CH_3OH	0.1[1]	0.787	7.9
$H_2O + CO_2 + CH_4$	H_2CO	0.04[1]	0.316	3.2
$H_2O + CO_2 + CH_4$	HCO	0.01[1]	0.079	0.8
$H_2O + CO_2 + CH_4$	C_2H_6	0.8[1]	6.124	61.2
H_2O+ CH_4 2:1	C_2H_6	0.22[2]	1.722	17.2
H_2O+ CH_4 2:1	CH_3OH	0.13[2]	1.022	10.2
H_2O+ CH_4 2:1	C_2H_5OH	0.12[2]	0.943	9.4
H_2O+ CH_4 2:1	CH_3CHO	0.01[2]	0.079	0.8
H_2O+ CH_4 2:1	C_3H_8	0.04[2]	0.316	3.2
H_2O+ CH_4 15:1	C_2H_6	0.004[2]	0.032	0.3
H_2O+ CH_4 15:1	CH_3OH	0.02[2]	0.158	1.6
H_2O+ CH_4 15:1	C_2H_5OH	0.007[2]	0.055	0.6
H_2O + CO 5:1	HCO	0.006[3]	0.047	0.5
H_2O + CO 5:1	H_2CO	0.05[3]	0.394	3.9
H_2O + CO 5:1	HCOOH	0.28[3]	2.188	21.8
H_2O + CO 5:1	CH_3OH	0.08[3]	0.630	6.3

H_2O + CO 5:1	CH_4	0.32[3]	2.50	25.0
H_2O + CO 20:1	HCO	0.003[3]	0.023	0.2
H_2O + CO 20:1	H_2CO	0.02[3]	0.158	1.6
H_2O + CO 20:1	CH_3OH	0.006[3]	0.047	0.5
H_2O + CO 20:1	CH_4	0.02[3]	0.158	1.6

The importance of temperature on chemical reactions taking place in cometary or other ices has been debated. Once bonds are broken and radicals form, they need to encounter other molecules so that reactions may occur, a situation that is more likely at warmer temperatures. However, it has been established by numerous experimenters that reactions do happen in the solid state at temperatures as low at 10 K, so temperature cycling is not a requirement (Moore et al., 1983, 2003; Johnson, 1989; Hudson and Moore, 1995, 1999; Moore and Hudson, 1998); however, temperature cycling may encourage reactions, and is therefore a preferred condition for the poles of the Moon if in-situ organic synthesis is to arise. Temperature modeling has shown that even in regions shaded from direct sunlight, reflected light off nearby topographic highs can produce substantial temperature variation in the shallow subsurface (Vasavada et al., 1999). Meteorite impacts on many scales provide an additional source of temporary heating. The Moon therefore meets the condition of sufficient temperature cycling to enhance the ability of radicals produced by irradiation to encounter each other and react.

4.4.3 Implications for Mercury

Recent results from the MESSENGER mission support previous Earth-based radar observations (Harmon and Slade, 1992) that first suggested the possibility of water ice in polar permanently shadowed regions. Neutron spectrometer measurements show decreases in epithermal neutron flux at Mercury's poles consistent with thick layers of nearly pure water ice buried 10 to 30 cm beneath the surface (Lawrence et al., 2013).

Thermal modeling, together with surface reflectance measurements, indicate that in some places these water ice deposits may be covered by a dark surface layer of complex organic materials (Neumann et al., 2013; Paige et al., 2013). Processing of simple cometary organics by high-energy photons and particles trapped in Mercury's magnetic field has been suggested to explain the origins of the dark carbonaceous material observed (Paige et al., 2013). However, since our lunar simulations indicate that a lower limit of only about 60 My are required to accumulate a dose of 1eV/molecule and potentially initiate organic synthesis, and Lawrence et al. (2013) estimate the age of Mercury's water deposits to be in the range of 18 to 70 My, galactic cosmic rays alone could have produced the organic deposits from simple cometary ices without more complex precursors.

4.5 Conclusions

We have shown that galactic cosmic ray protons provide enough energy to stimulate chemistry over the time available for volatiles to be retained in lunar cold traps—1-2 Gyr. Our findings are relevant not only to Earth's Moon but also to other airless bodies that are exposed to a radiation environment similar to that of the Moon. Examples include Mercury, which possesses permanently shadowed regions (Thomas, 1974; Chabot et al., 2012) that appear to contain both abundant water ice and complex organics (Harmon and Slade, 1992; Lawrence et al., 2013; Neumann et al., 2013; Paige et al., 2013), as well as asteroid bodies (e.g., Ceres, main-belt comets) that contain substantive concentrations of water ice and volatiles (Lebofsky et al., 1981; Hsieh and Jewitt, 2006). Our studies of the lunar case indicate that radiation dose from galactic cosmic rays accumulates fast enough to be considered an important energy source for processing of simple organics in Mercury's cold traps in addition to the energetic photons suggested by Paige et al. (2013). In-situ organic synthesis driven by galactic cosmic rays is a process that may be plausibly occurring at the poles of the Moon, Mercury and other silicate bodies, and would have substantial effect on volatile and organic detections by past and future missions.

CHAPTER 5

CONCLUDING REMARKS AND FUTURE STEPS

This dissertation presents new global mineral maps of the lunar surface, a series of two- and three-component mixing models that constrain the source of the mafic component of the lunar highlands, and models of the radiation from galactic cosmic rays in the lunar polar regolith. The mineral maps, together with the mixing models that use them as inputs, demonstrate that the lunar magma ocean likely did not produce very mafic anorthosites on average, and lends support to the argument based on spectral detections of very pure anorthosites by the Kaguya Spectral Profiler and Multiband imager and the Moon Mineralogy Mapper on Chandrayaan-1 that lunar magma ocean anorthosites predominantly contained < 2vol% mafic minerals (Ohtake et al. 2009; Pieters et al. 2009a; Yamamoto et al. 2012; Cheek et al. 2013). The mixing models also contribute to a better understanding of the range of possible combinations of post-magma ocean igneous rocks and ultramafic mantle rocks that could be present in the highlands crust. The maximum amount of mantle material permitted in the highlands crust determined from these models combined with basin ejecta calculations support the conclusion of Wieczorek and Phillips (1999) that the largest lunar basins had depth-to-diameter ratios shallower than 1/10. The final portion of this dissertation concludes based on models of GCR flux at the lunar poles that if simple ices are present in lunar polar cold traps, they would receive high enough radiation doses that in-situ synthesis of complex organics could plausibly be taking place. However, the studies performed in this work have revealed additional areas for research that would further improve our understanding of the questions examined in this dissertation. These opportunities for future work are described below.

Distribution of high-Ca pyroxene in the lunar crust

The abundant high-calcium pyroxene detected in the lunar highlands in the neutron and gamma ray spectrometer-validated spectral mineral maps described in Chapter 2 is qualitatively consistent with observations by Ogawa et al. (2011) of high-Ca pyroxene in craters between 8 and 24 km in size. However, a recent spectral survey of

2700 small, fresh highland craters (<1 km diameter) by Lucey et al. (2014) found no detectable high-Ca pyroxene. An important area of future study is to investigate the apparent discrepancies between these observations and determine what these studies together can tell us about the distribution of high-Ca pyroxene in the lunar crust.

Anorthosite mafic composition

The models of Chapter 3 assume that the relative abundances of olivine, orthopyroxene, and clinopyroxene are fixed at levels obtained by averaging the mafic composition of all Apollo samples classified as ferroan anorthosites. However, there is substantial variation in mafic composition among these samples, so this choice is somewhat arbitrary and may artificially limit the permitted solutions for a given anorthosite mafic abundance. Future models should instead permit the mafic composition of anorthosites to vary to obtain the best agreement with the mineral maps at each pixel.

Additional sources of radiation the Moon's poles

In the radiation study of Chapter 4 we considered only the radiation dose from galactic cosmic rays, neglecting the contribution from the solar wind and solar energetic particles. These radiation sources have much higher flux, though the lower energies of these particles limit their depth of penetration and renders their products susceptible to micrometeorite erosion. A more complete study of the radiation environment of the lunar poles would include contributions from these particles.

The unique radiation environment at Mercury

The radiation dose results calculated for the Moon in Chapter 4 can be extended to Mercury and to other airless bodies in the solar system. However, Mercury has planetary magnetic field that, though weaker than the Earth's, could serve to modify the radiation environment at the poles by entrapping lower energy solar particles discussed above. A thorough study of the unique radiation sources for Mercury and their interactions with its planetary magnetic field could provide additional insight into the source of the dark, possibly organic material described by Neumann et al. (2013).

APPENDIX A

RESULTS OF ALL MIXING MODELS

Table A1. Rock type abundance results for all scenarios calculated. No-solution pixels and maria pixels (defined by all nearside pixels with greater than 15 wt% FeO according to the LP GRS (Prettyman et al. 2006)) are excluded from the mean rock type abundances.

	Description	Mean norite (vol%)	Mean gabbro (vol%)	Mean troctolite (vol%)	Mean dunite (vol%)	Mean pyrox. (vol%)	Mean mare basalt (vol%)	Mean anorth. (vol%)	Mantle Material (vol%)	Total non-MO rocks (vol%)	% area no solution	% area with solution but less than mantle limit
Mafics into POI and/or mare basalt	Pure anorthite; all mafics POI	10.53	21.99	12.61				54.87	0.00	45.13	0.00	n/a
	PAN; excess mafics POI	10.43	22.41	11.47				55.69	0.00	44.31	6.87	n/a
	Anorthosites with 7 vol% mafics; excess mafics POI	8.86	22.34	8.42				60.39	0.00	39.61	18.52	n/a
	PAN; excess ol + opx POI; excess cpx mare basalt	10.40		11.41			19.43	58.77	0.00	41.23	6.94	n/a
	Mafic anorthosites (15 vol%); excess ol + opx POI; excess cpx mare basalt	5.79		6.21			21.30	66.71	0.00	33.29	72.40	n/a

Mafics into mantle and/or mare basalt	Pure anorthite; all mafics mantle				5.93	18.34		75.73	24.27	24.27	0.00	n/a
	PAN; excess mafics mantle				5.18	18.31		75.50	23.50	23.50	7.17	n/a
	Mafic anorthosites (15 vol%); excess mafics mantle				2.45	12.54		85.02	14.98	14.98	73.18	n/a
	Mafic anorthosites (15 vol%); excess ol+opx mantle; excess cpx mare bas.				2.51	2.56	20.77	74.17	5.06	25.83	75.35	n/a
Mafics into mantle up to 40%	PAN; mafics to mantle up to 40%; excess ol + opx POI; excess cpx mare basalt	0.04		0.05	5.25	17.82	0.30	76.54	23.07	23.46	51.12	82.85

	Mafic anorthosites (15 vol%); mafics into mantle up to 40%; excess ol + opx POI; excess cpx mare basalt	0.00		0.00	2.47	12.35	0.00	85.18	14.82	14.82	80.48	93.94
Mafics into mantle up to 30%	PAN; mafics into mantle up to 30%; excess ol + opx POI; excess cpx mare basalt	0.49		0.43	5.29	16.61	2.16	75.02	21.90	24.98	51.71	62.92
	Mafic anorthosites (15 vol%); mafics into mantle up to 30%; excess ol + opx POI; excess cpx mare basalt	0.01		0.03	2.47	10.78	0.17	86.54	13.25	13.46	81.87	73.95
Mafics into mantle up to 20%	PAN; mafics to mantle up to 20%; excess ol + opx POI, excess cpx mare basalt	2.53		2.13	4.55	13.93	7.12	69.75	18.47	30.25	36.39	42.10

	Mafic anorthosites (15 vol%); mafics into mantle up to 20%; excess ol + opx POI; excess cpx mare basalt	4.38		4.52	2.59	13.42	10.33	70.92	16.00	35.24	66.25	44.89
	PAN; ol + opx to mantle up to 20%; excess ol + opx into POI; all cpx to mare basalt	0.09		0.19	5.14	5.19	19.39	69.99	10.34	30.01	7.63	96.40
Mafics into mantle up to 2%	PAN; mafics to mantle up to 2%; excess ol + opx POI, excess cpx mare basalt	9.50		10.28	0.52	1.48	18.01	60.22	2.00	39.78	7.59	10.23
	Mafic anorthosites (15 vol%); mafics into mantle up to 2%; excess ol + opx POI; excess cpx mare basalt	5.17		5.73	0.59	1.40	20.84	66.26	1.99	33.74	78.40	10.50

	PAN; ol + opx to mantle up to 2%; excess ol + opx into POI; all cpx to mare basalt	8.52		9.25	1.01	0.99	19.50	60.73	2.00	39.27	8.18	5.86

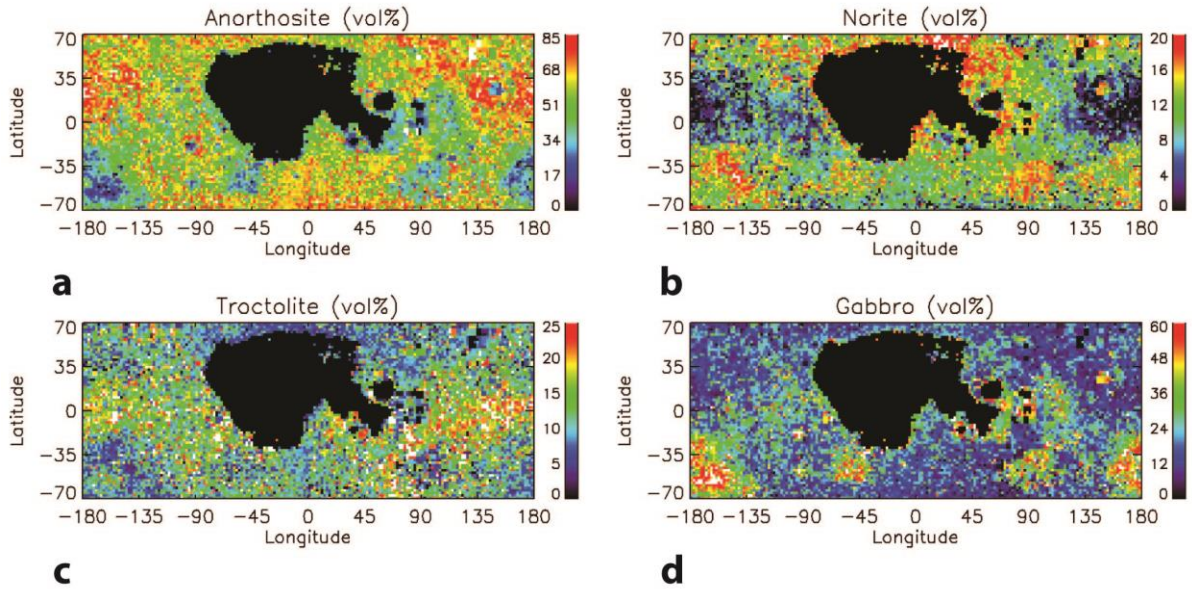

Figure A1. a-d) Rock type abundances calculated assuming pure anorthite and assigning all excess mafics to post-magma ocean igneous products.

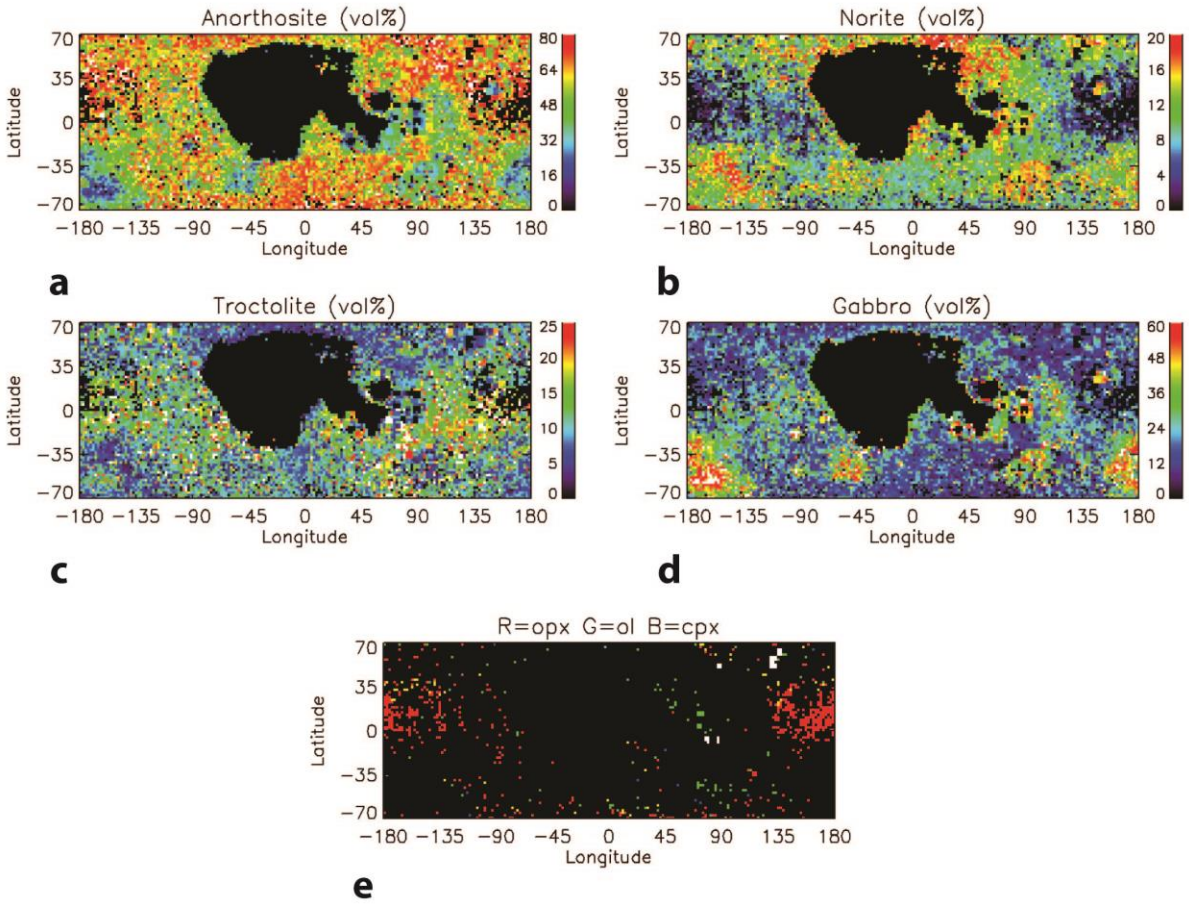

Figure A2. a-d) Rock type abundances calculated assuming PAN (2 vol% mafics) and assigning all excess mafics to post-magma ocean igneous products. e) Map showing the limiting mafic minerals at "no solution" pixels for anorthosites of the assumed mafic abundance and composition.

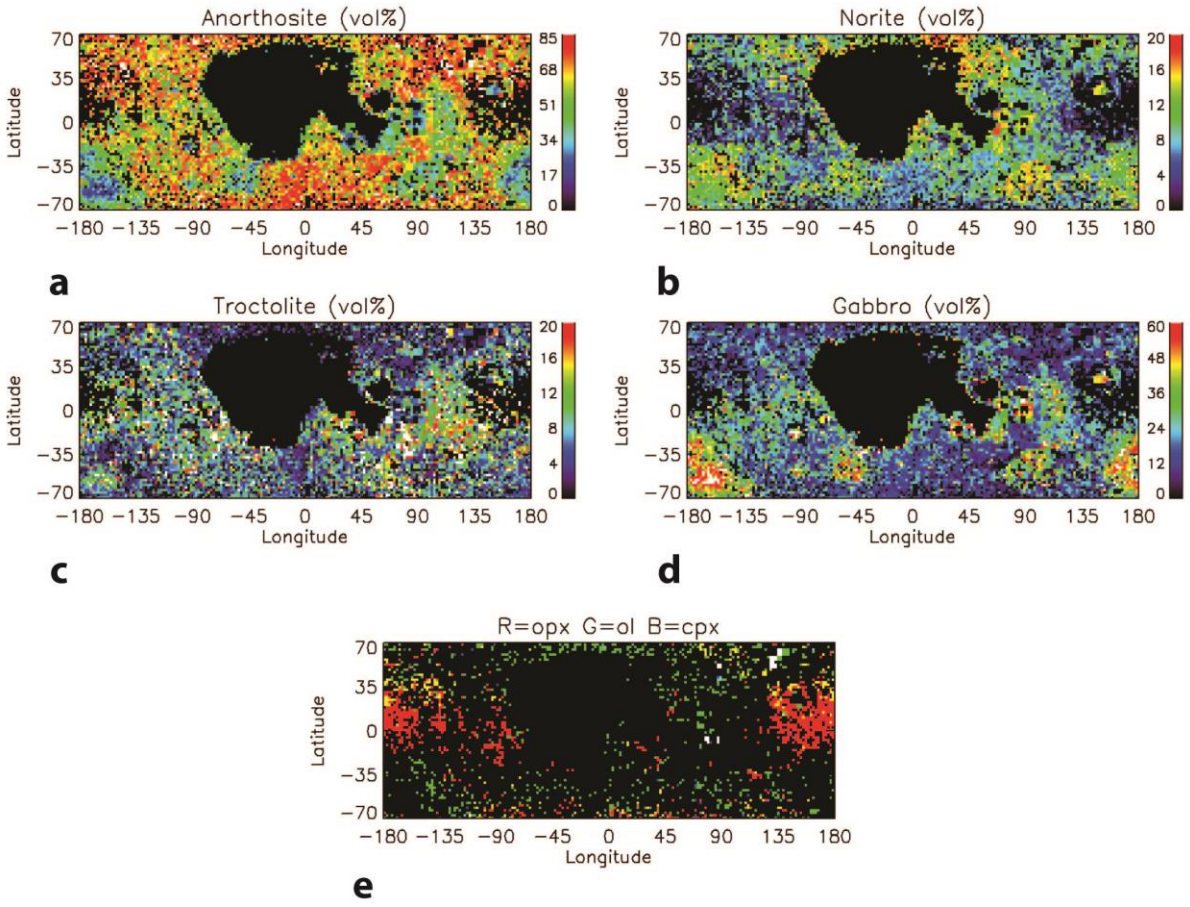

Figure A3. a-d) Rock type abundances calculated assuming 7 vol% mafics and assigning all excess mafics to post-magma ocean igneous products. e) Map showing the limiting mafic minerals at "no solution" pixels for anorthosites of the assumed mafic abundance and composition.

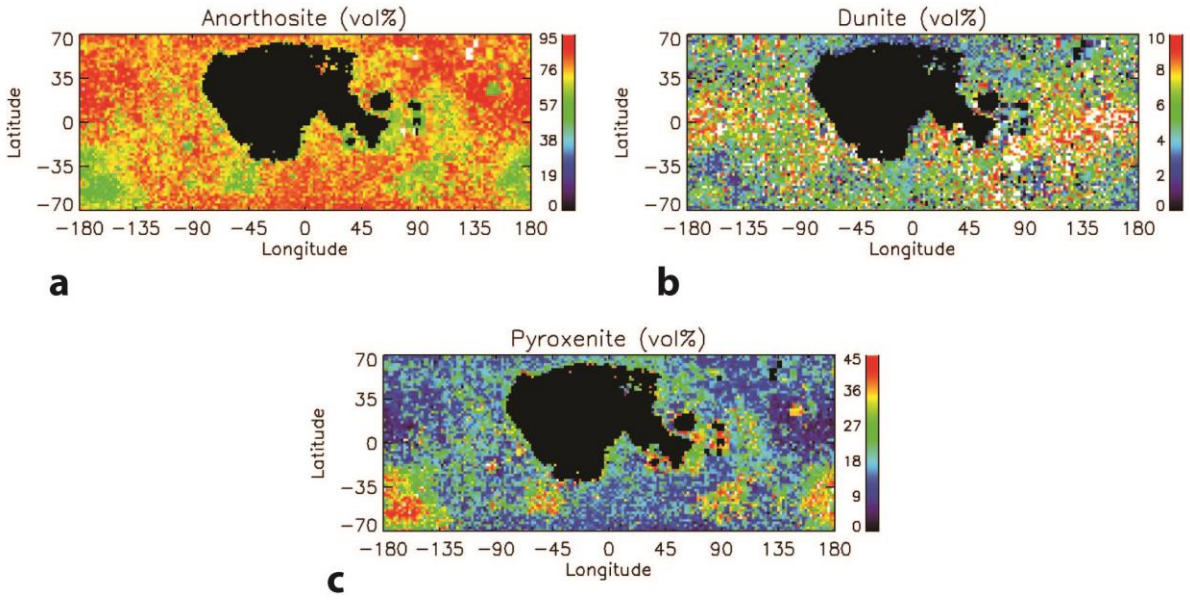

Figure A4. a-c) Rock type abundances calculated assuming pure anorthite and assigning all excess mafics to mantle rocks (dunite and pyroxenite). Pixels where both are present are also consistent with peridotite.

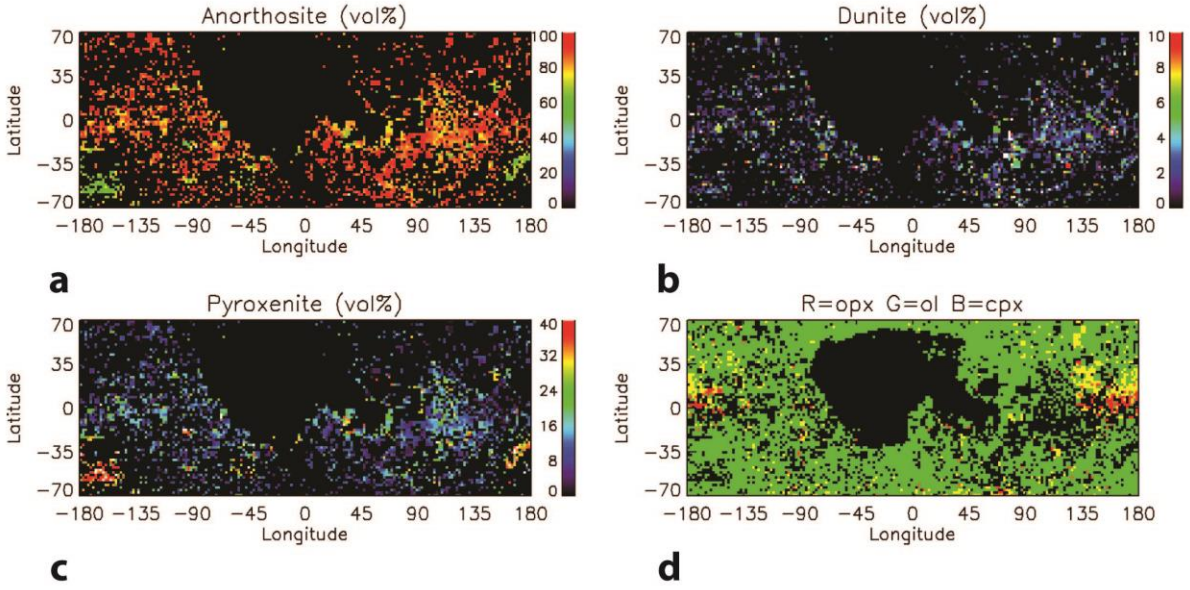

Figure A5. a-c) Rock type abundances calculated assuming 15 vol% mafics and assigning all excess mafics to mantle rocks (dunite and pyroxenite). Pixels where both are present

are also consistent with peridotite. d) Map showing the limiting mafic minerals at "no solution" pixels for anorthosites of the assumed mafic abundance and composition.

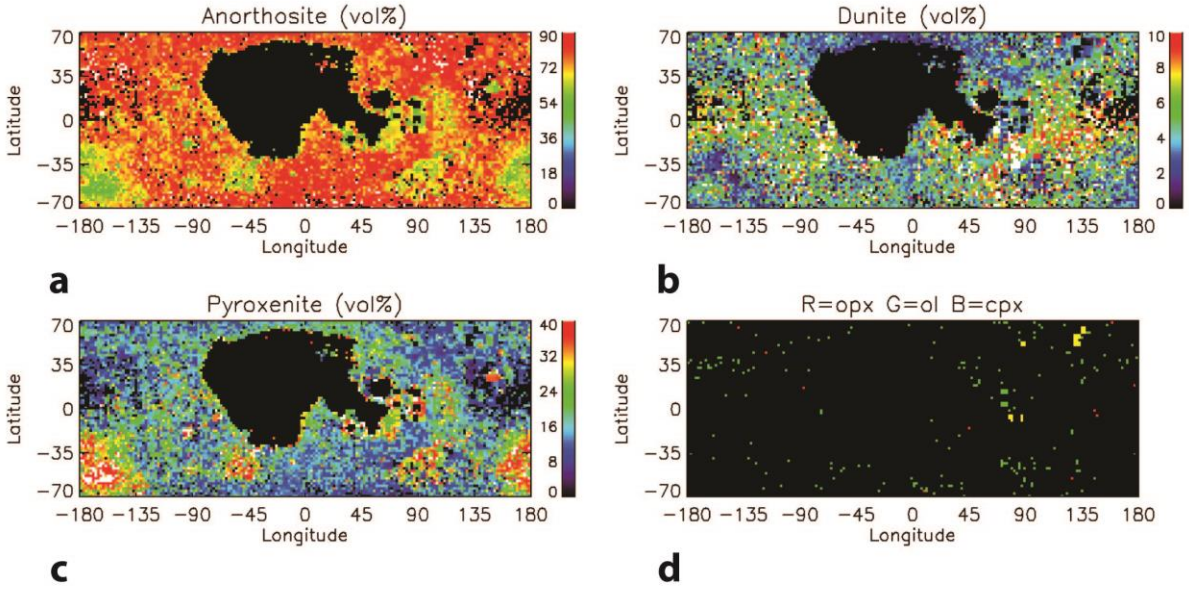

Figure A6. a-c) Rock type abundances calculated assuming PAN (2 vol% mafics) and assigning all excess mafics to mantle rocks (dunite and pyroxenite). Pixels where both are present are also consistent with peridotite. d) Map showing the limiting mafic minerals at "no solution" pixels for anorthosites of the assumed mafic abundance and composition.

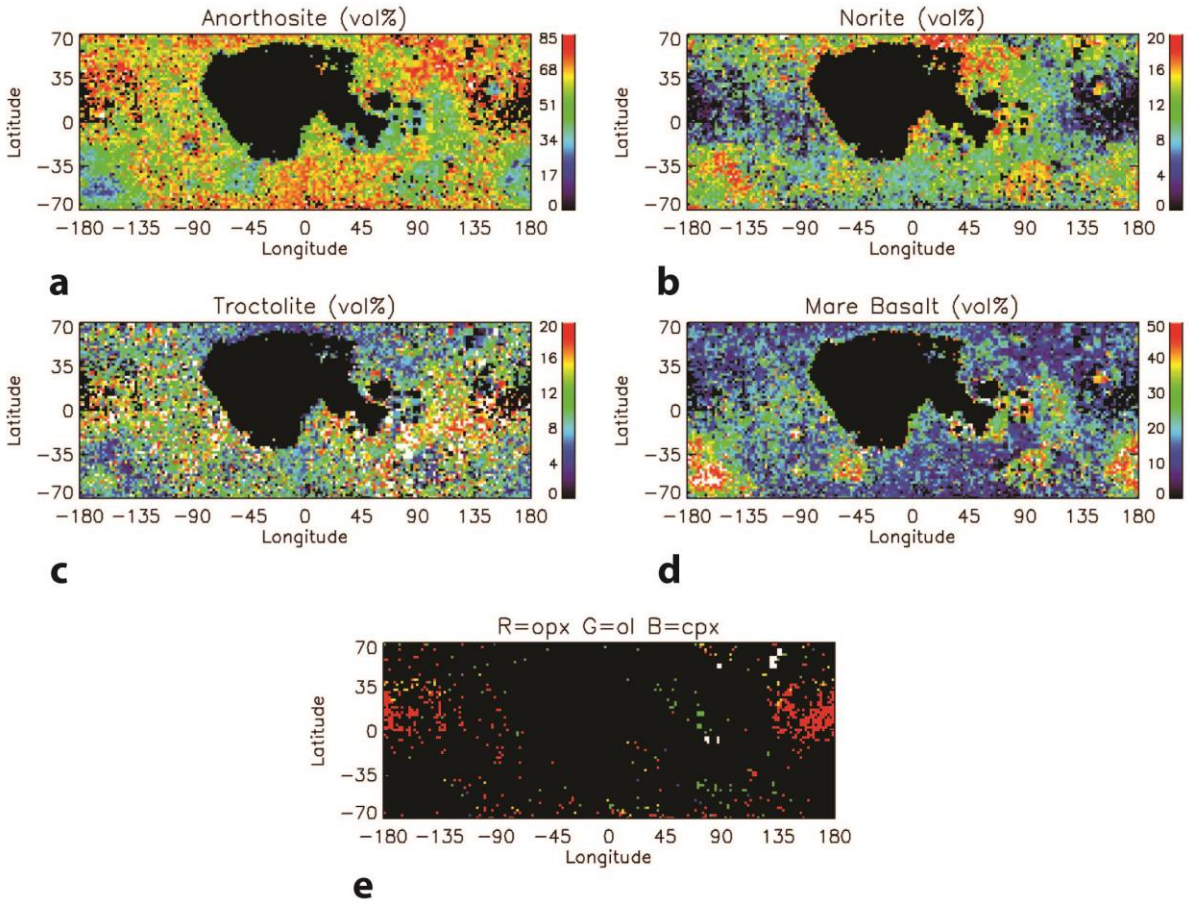

Figure A7. a-d) Rock type abundances calculated assuming PAN (2 vol% mafics) and assigning all excess mafics to post-magma ocean igneous material, with clinopyroxene assumed to be present in the form of mare basalt. e) Map showing the limiting mafic minerals at "no solution" pixels for anorthosites of the assumed mafic abundance and composition.

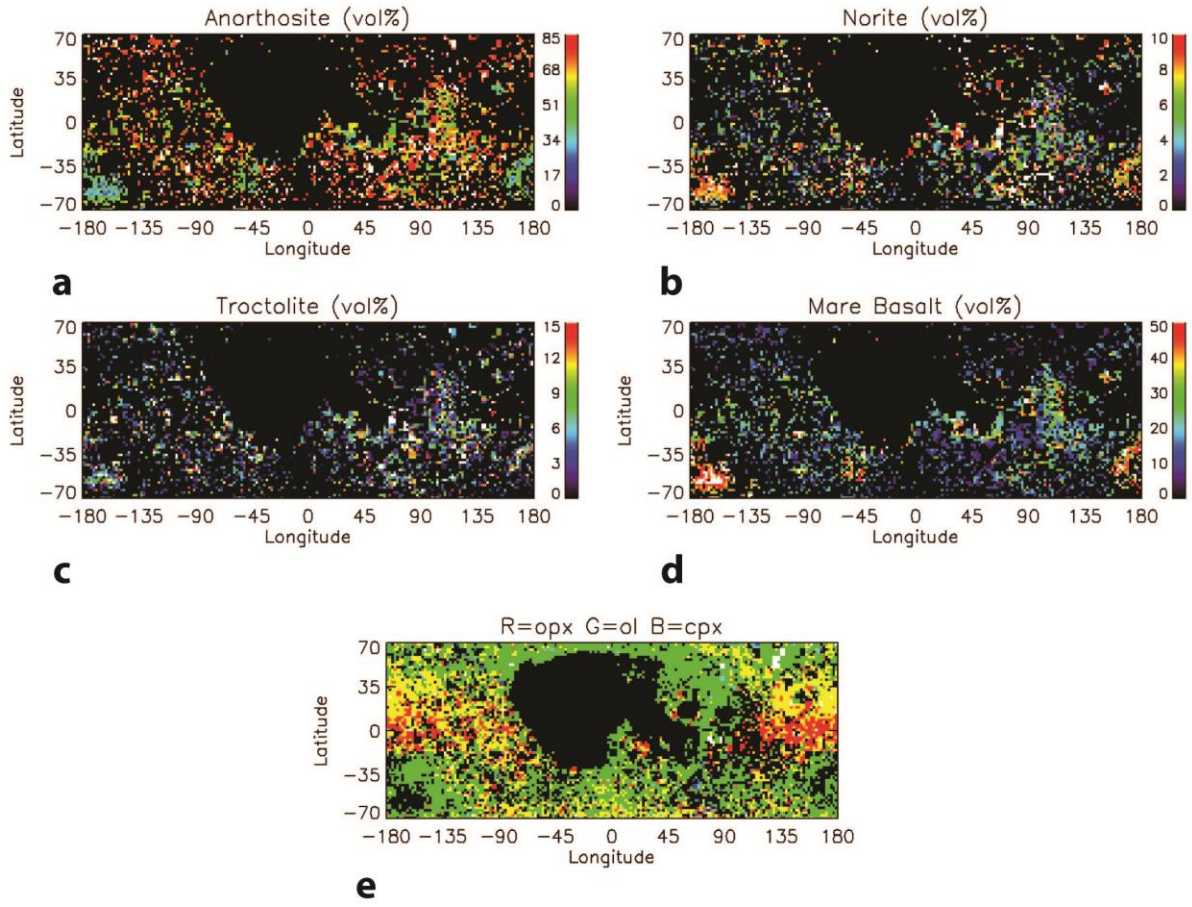

Figure A8. a-d) Rock type abundances calculated assuming 15 vol% mafics and assigning all excess mafics to post-magma ocean igneous material, with clinopyroxene assumed to be present in the form of mare basalt. e) Map showing the limiting mafic minerals at "no solution" pixels for anorthosites of the assumed mafic abundance and composition.

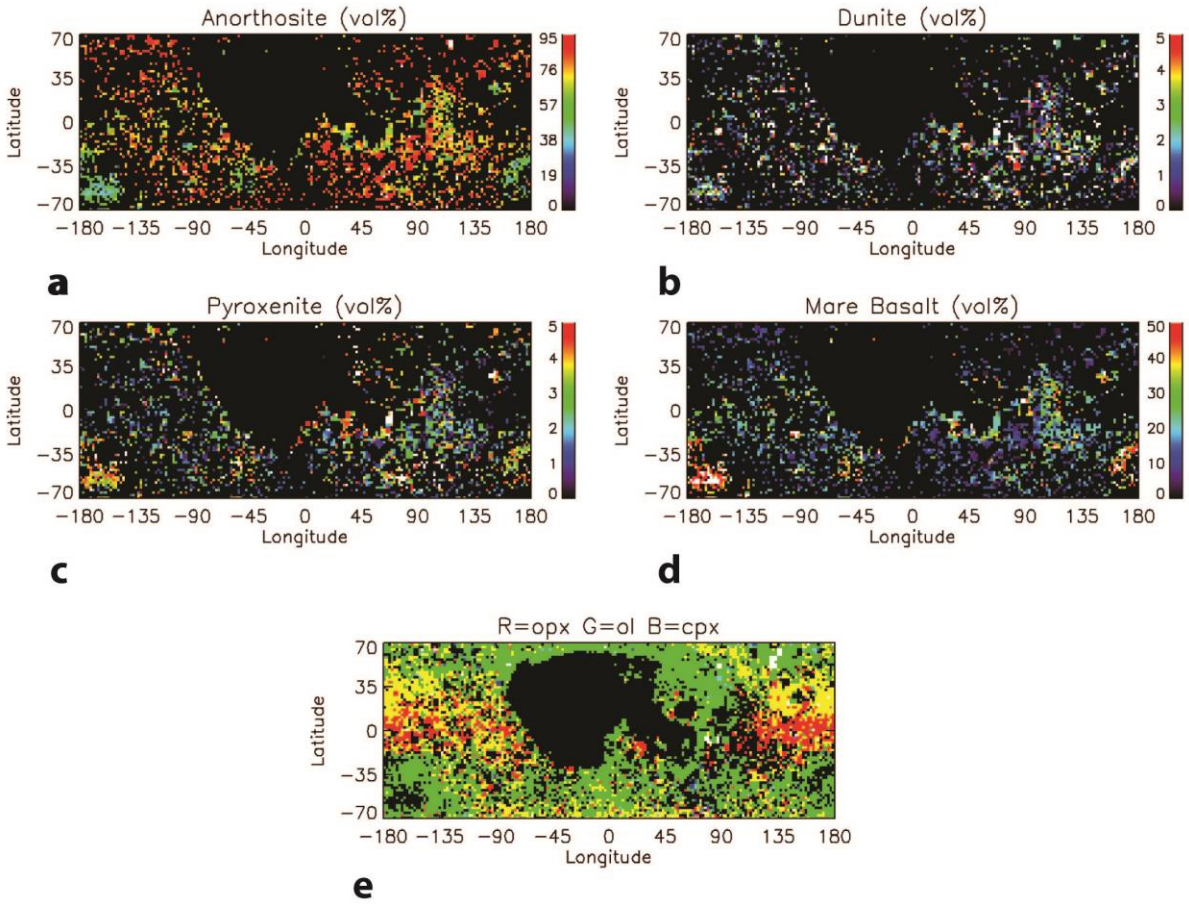

Figure A9. a-d) Rock type abundances calculated assuming 15 vol% mafics and assigning all excess orthopyroxene and olivine to mantle rocks (dunite and pyroxenite). Pixels where both are present are also consistent with peridotite. All clinopyroxene was assigned to mare basalt. e) Map showing the limiting mafic minerals at "no solution" pixels for anorthosites of the assumed mafic abundance and composition.

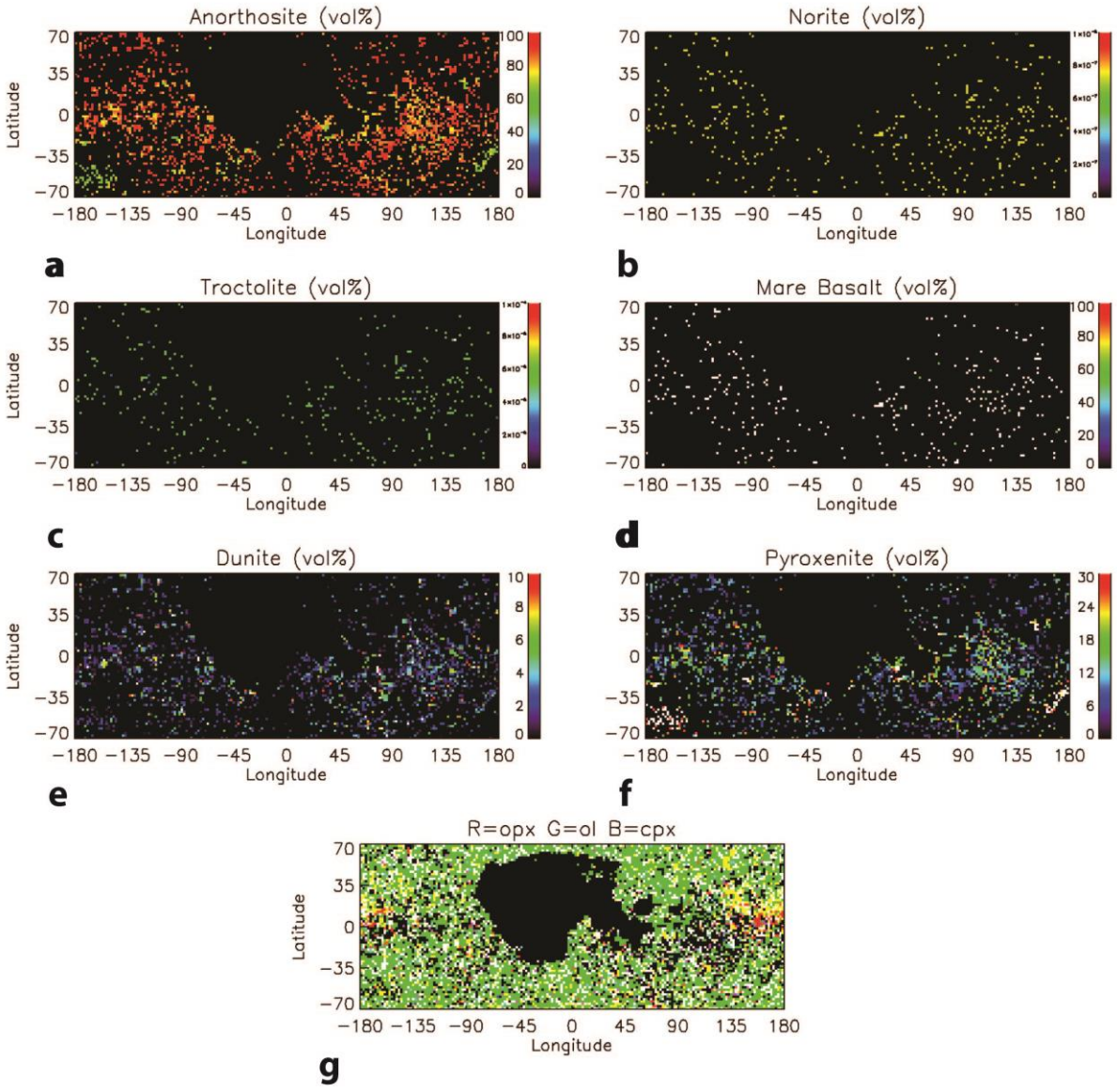

Figure A10. a-f) Rock type abundances calculated assuming 15 vol% mafics and assigning mafics to mantle rocks (dunite and pyroxenite) up to an upper limit of 40 vol%, with mafics above this limit assigned to post-magma ocean igneous products. Pixels where both dunite and pyroxenite are present are also consistent with peridotite. g) Map showing the limiting mafic minerals at "no solution" pixels for anorthosites of the assumed mafic abundance and composition.

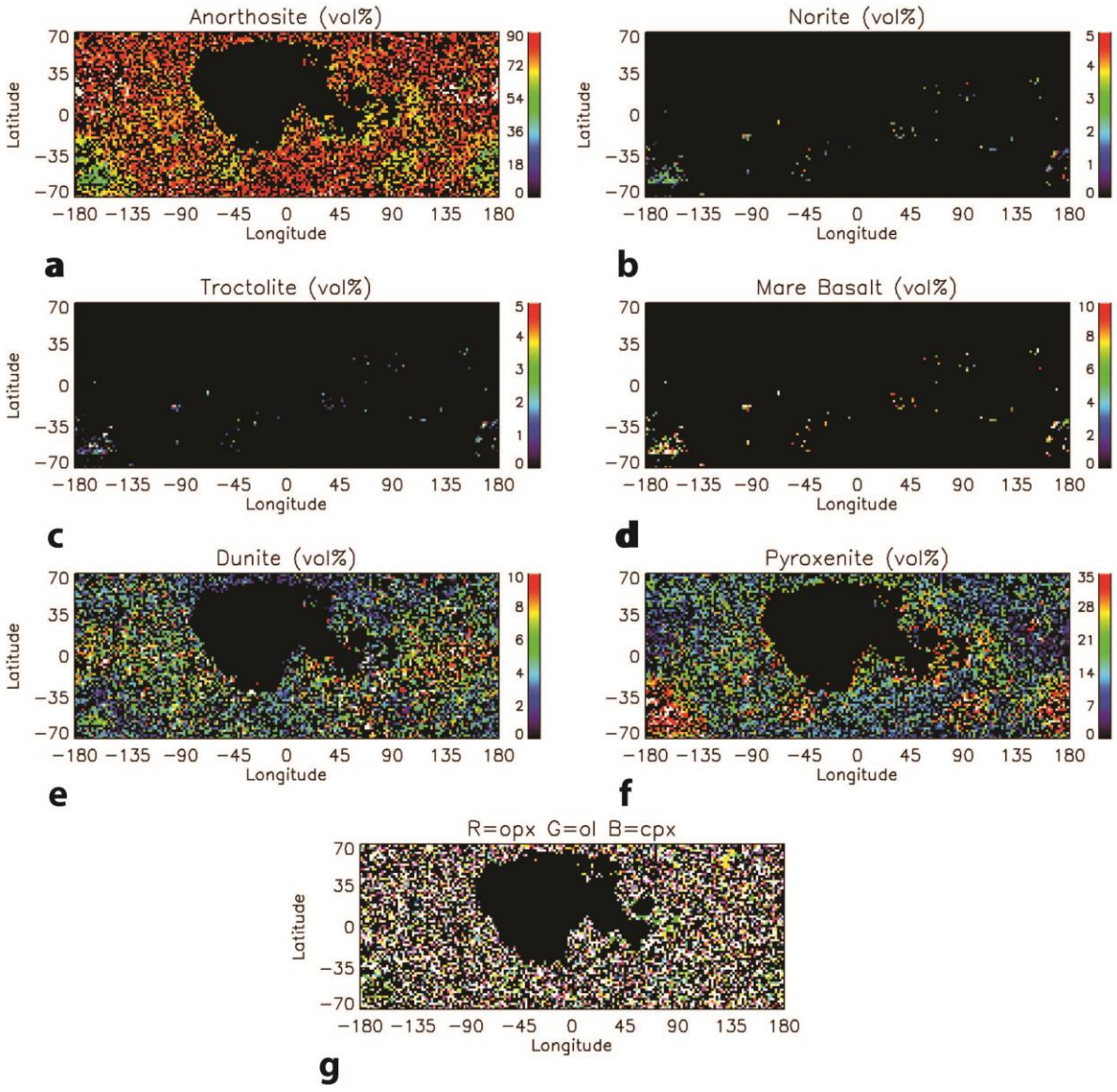

Figure A11. a-f) Rock type abundances calculated assuming PAN (2 vol% mafics) and assigning mafics to mantle rocks (dunite and pyroxenite) up to an upper limit of 40 vol%, with mafics above this limit assigned to post-magma ocean igneous products. Pixels where both dunite and pyroxenite are present are also consistent with peridotite. g) Map showing the limiting mafic minerals at "no solution" pixels for anorthosites of the assumed mafic abundance and composition.

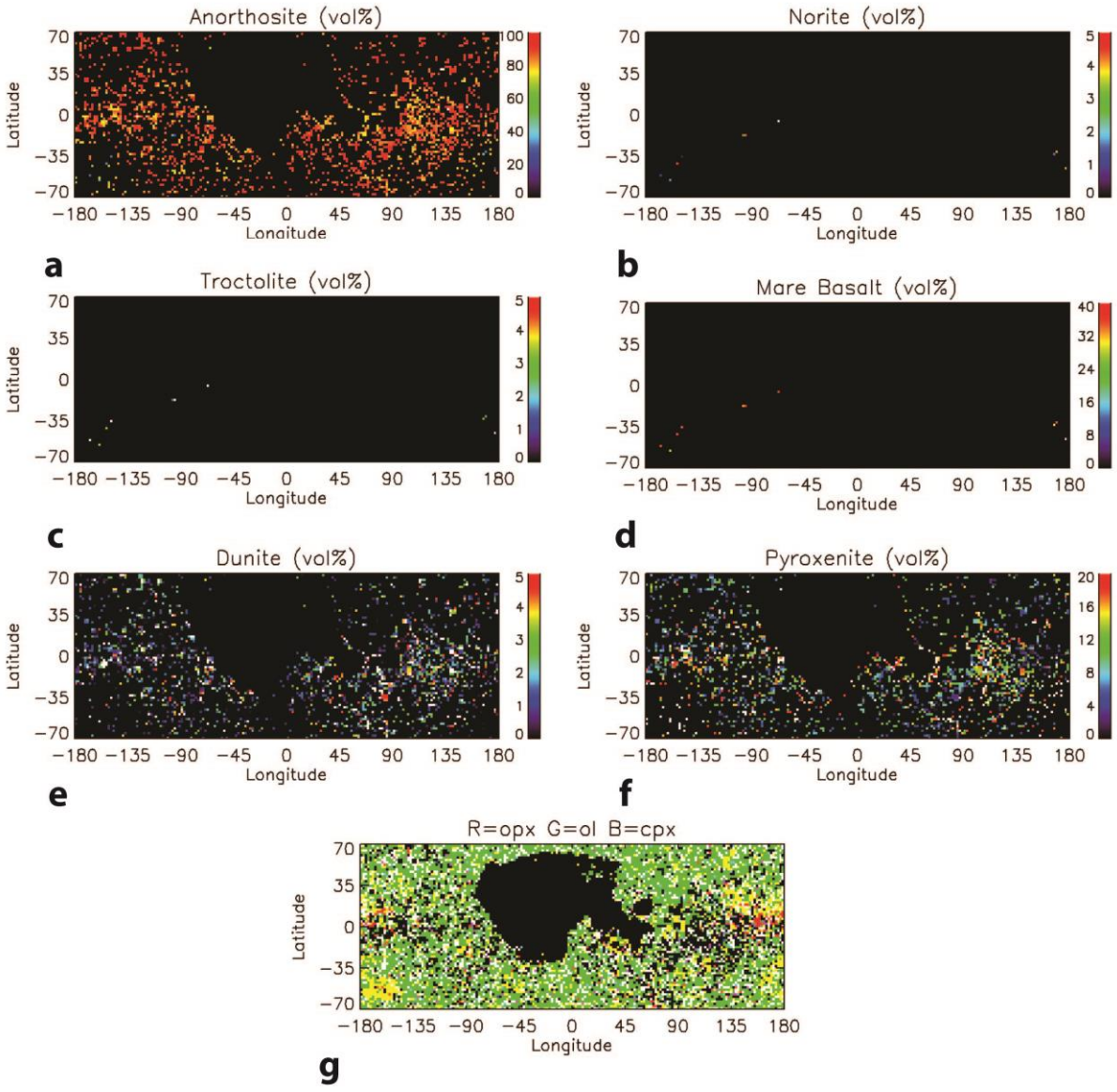

Figure A12. a-f) Rock type abundances calculated assuming 15 vol% mafics and assigning mafics to mantle rocks (dunite and pyroxenite) up to an upper limit of 30 vol%, with mafics above this limit assigned to post-magma ocean igneous products. Pixels where both dunite and pyroxenite are present are also consistent with peridotite. g) Map showing the limiting mafic minerals at "no solution" pixels for anorthosites of the assumed mafic abundance and composition.

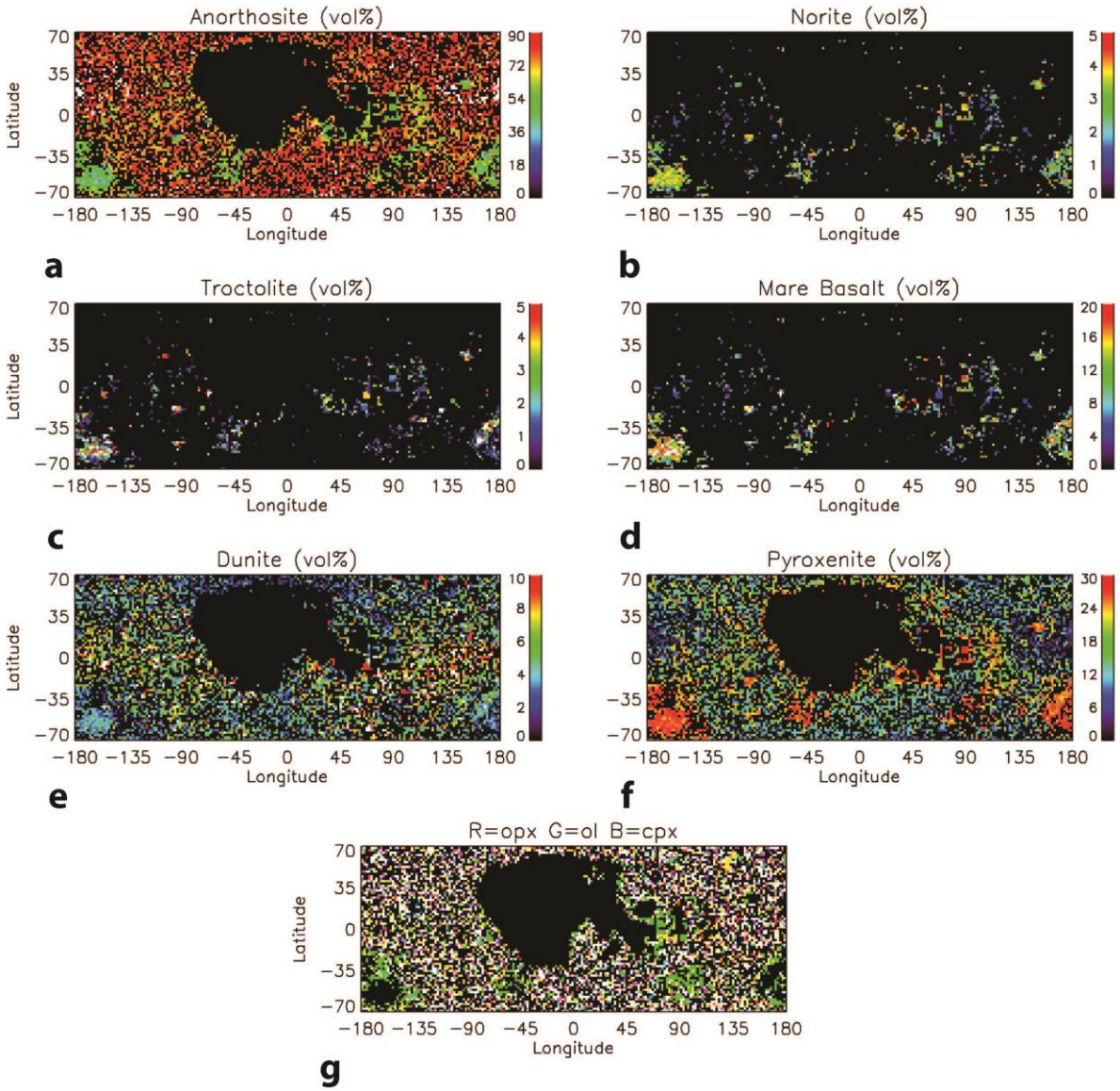

Figure A13. a-f) Rock type abundances calculated assuming PAN (2 vol% mafics) and assigning mafics to mantle rocks (dunite and pyroxenite) up to an upper limit of 30 vol%, with mafics above this limit assigned to post-magma ocean igneous products. Pixels where both dunite and pyroxenite are present are also consistent with peridotite. g) Map showing the limiting mafic minerals at "no solution" pixels for anorthosites of the assumed mafic abundance and composition.

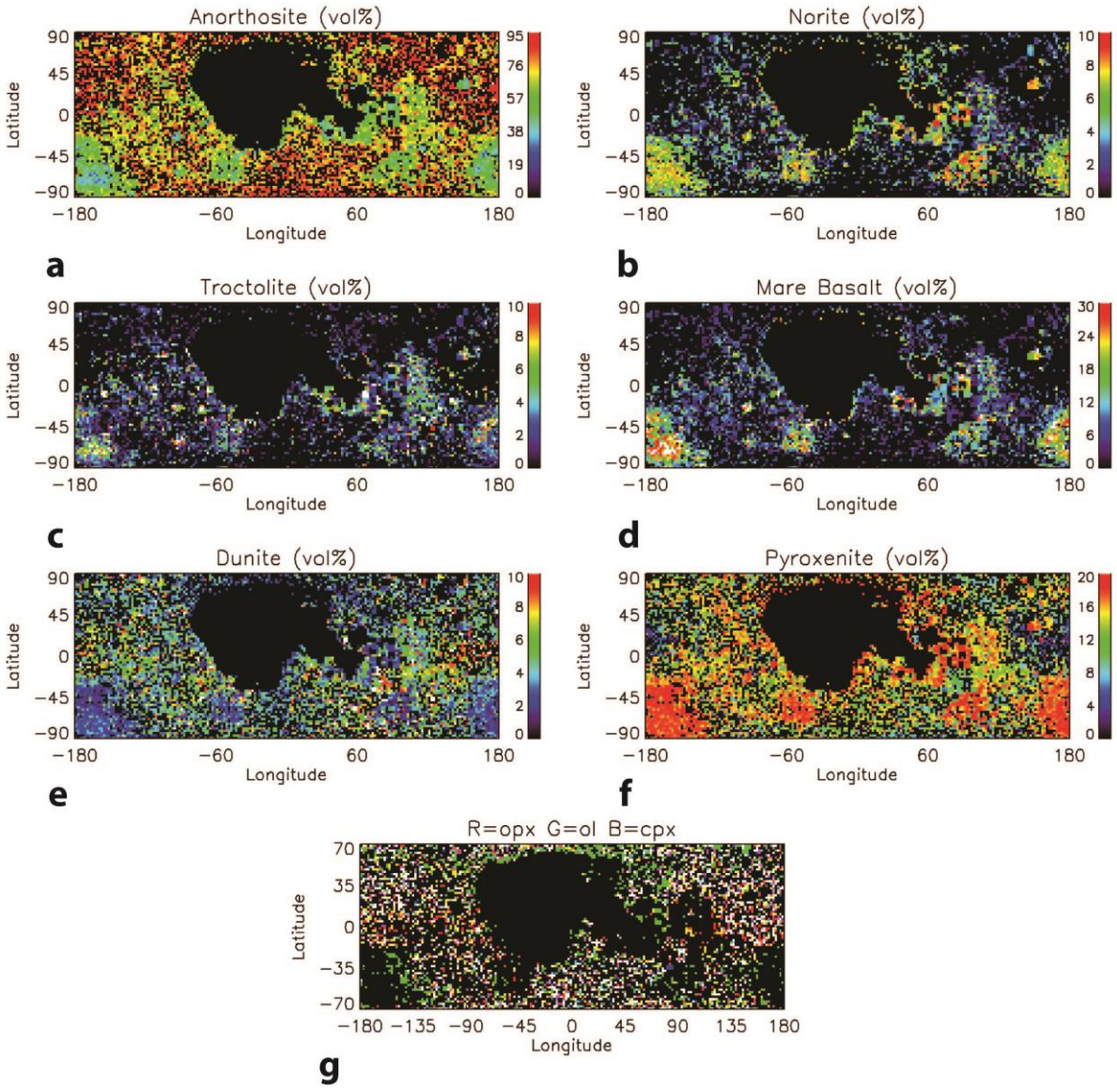

Figure A14. a-f) Rock type abundances calculated assuming PAN (2 vol% mafics) and assigning mafics to mantle rocks (dunite and pyroxenite) up to an upper limit of 20 vol%, with mafics above this limit assigned to post-magma ocean igneous products. Pixels where both dunite and pyroxenite are present are also consistent with peridotite. g) Map showing the limiting mafic minerals at "no solution" pixels for anorthosites of the assumed mafic abundance and composition.

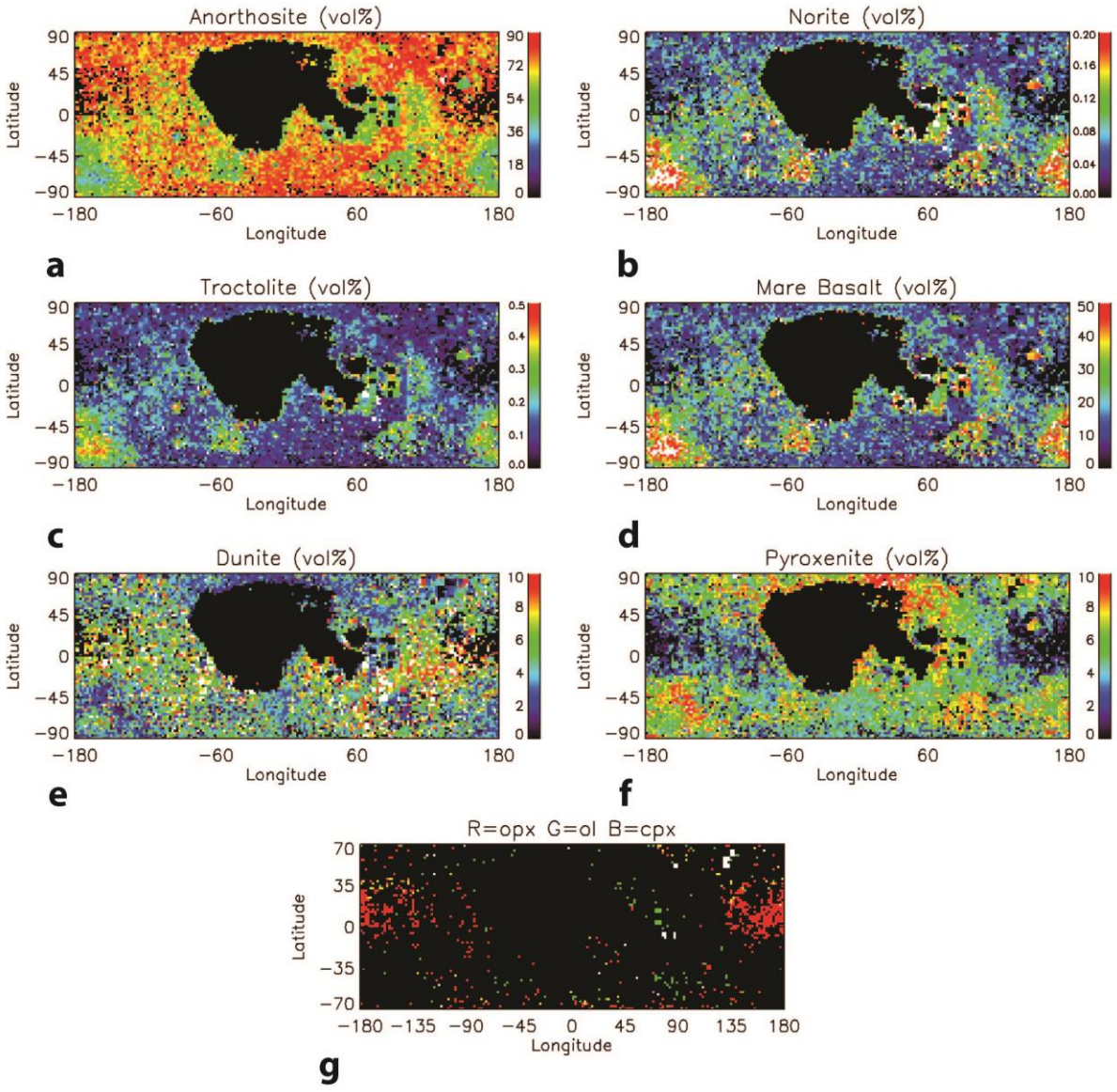

Figure A15. a-f) Rock type abundances calculated assuming PAN (2 vol% mafics) and assigning olivine and orthopyroxene to mantle rocks (dunite and pyroxenite) up to an upper limit of 20 vol%, with mafics above this limit assigned to post-magma ocean igneous products. All clinopyroxene was assumed to be present in the form of mare basalt. Pixels where both dunite and pyroxenite are present are also consistent with peridotite. g) Map showing the limiting mafic minerals at "no solution" pixels for anorthosites of the assumed mafic abundance and composition.

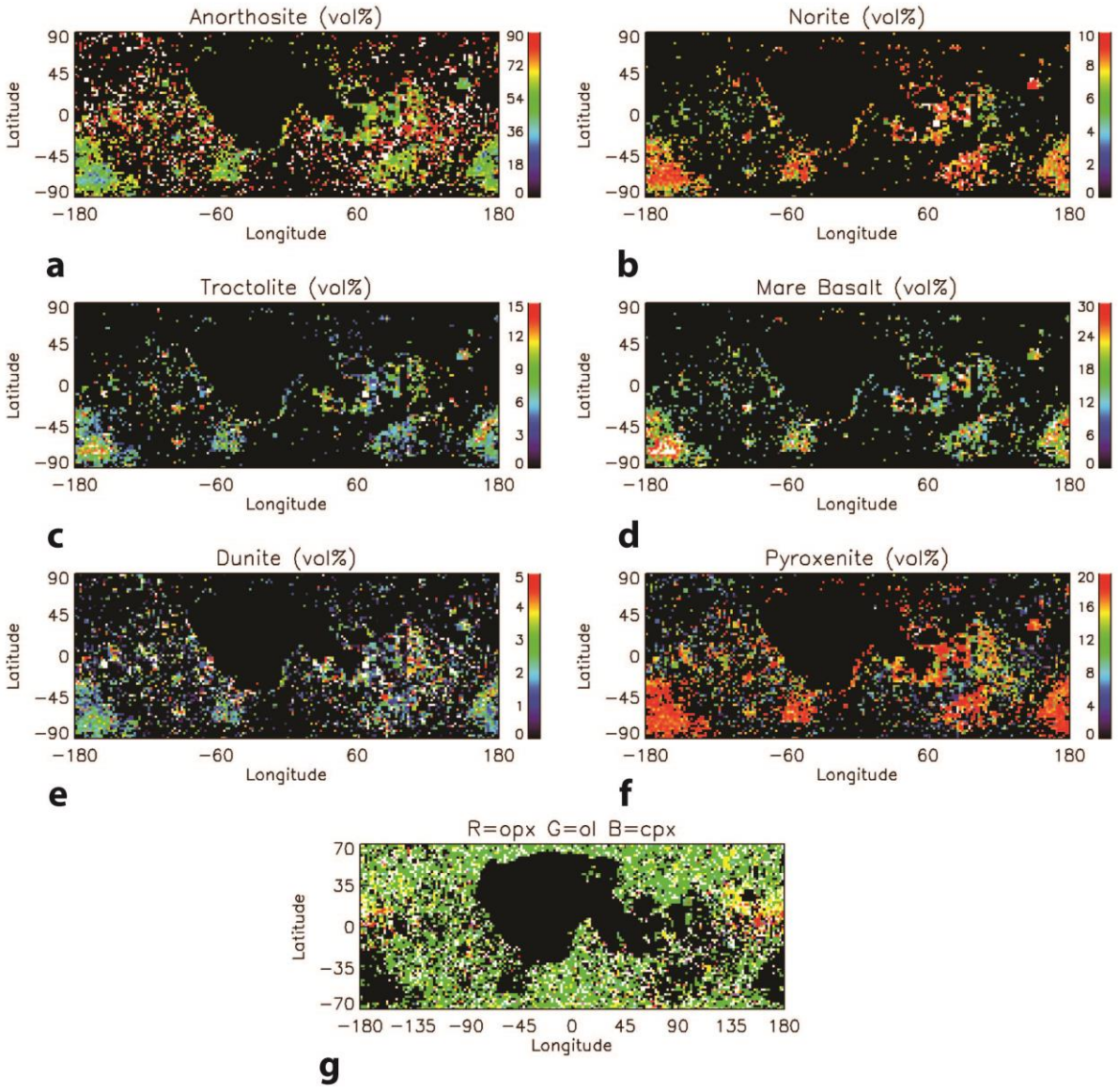

Figure A16. a-f) Rock type abundances calculated assuming 15 vol% mafics and assigning mafics to mantle rocks (dunite and pyroxenite) up to an upper limit of 20 vol%, with mafics above this limit assigned to post-magma ocean igneous products. Pixels where both dunite and pyroxenite are present are also consistent with peridotite. g) Map showing the limiting mafic minerals at "no solution" pixels for anorthosites of the assumed mafic abundance and composition.

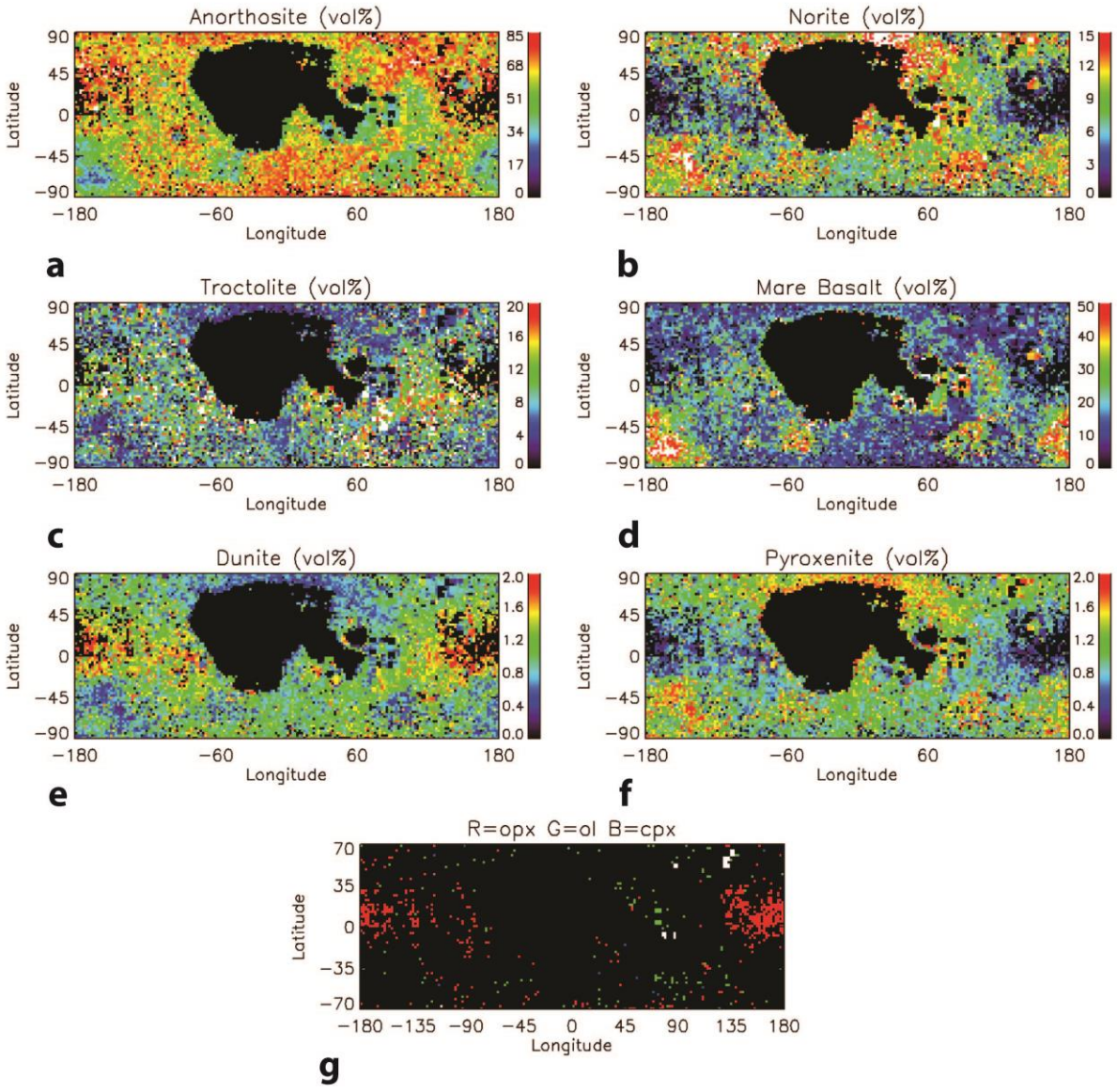

Figure A17. a-f) Rock type abundances calculated assuming PAN (2 vol% mafics) and assigning olivine and orthopyroxene to mantle rocks (dunite and pyroxenite) up to an upper limit of 2 vol%, with mafics above this limit assigned to post-magma ocean igneous products. All clinopyroxene was assumed to be present in the form of mare basalt. Pixels where both dunite and pyroxenite are present are also consistent with peridotite. g) Map showing the limiting mafic minerals at "no solution" pixels for anorthosites of the assumed mafic abundance and composition.

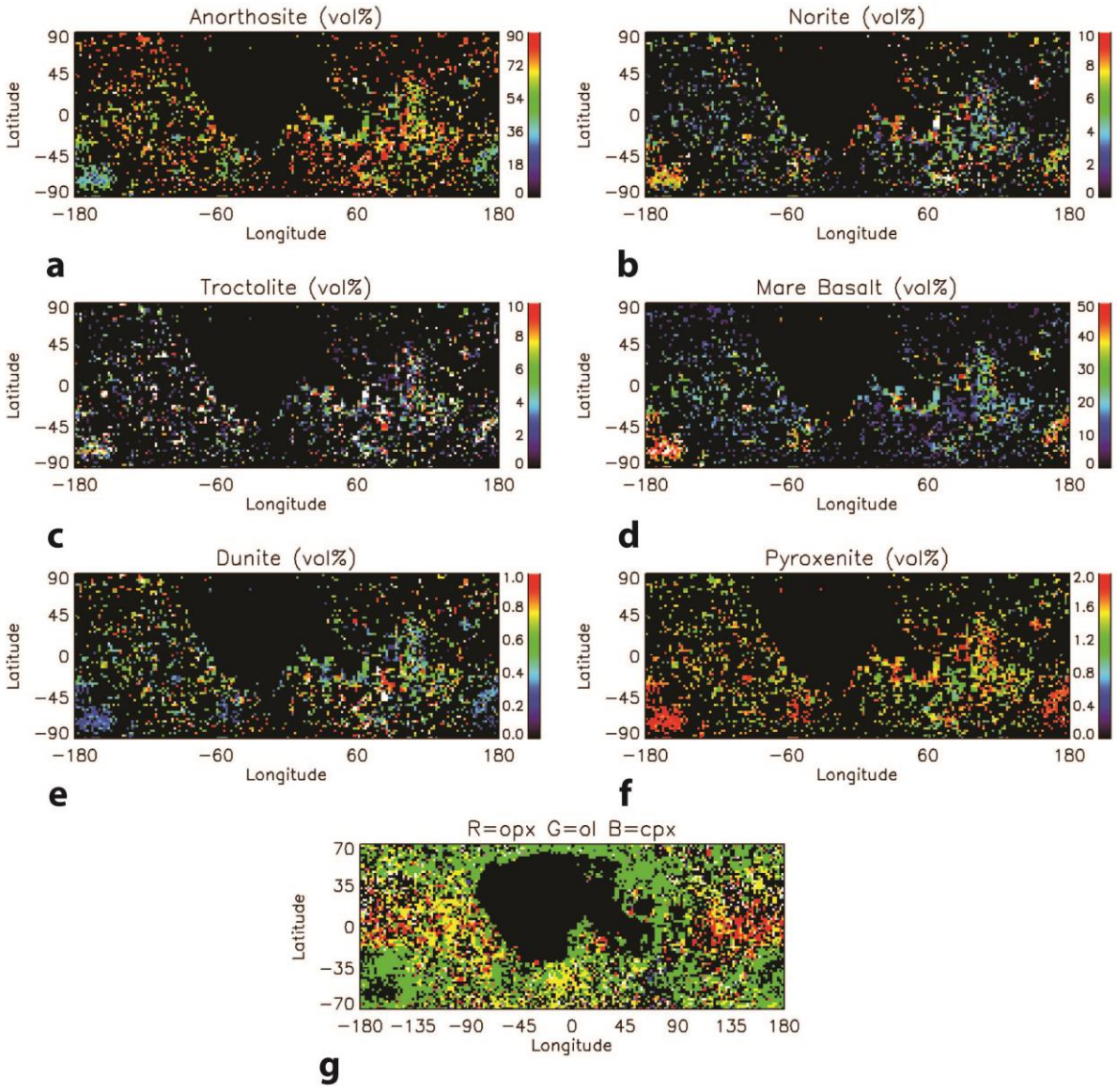

Figure A18. a-f) Rock type abundances calculated assuming 15 vol% mafics and assigning mafics to mantle rocks (dunite and pyroxenite) up to an upper limit of 2 vol%, with mafics above this limit assigned to post-magma ocean igneous products. Pixels where both dunite and pyroxenite are present are also consistent with peridotite. g) Map showing the limiting mafic minerals at "no solution" pixels for anorthosites of the assumed mafic abundance and composition.

APPENDIX B

USE OF THE MCNPX CODE

In order to validate our methods in applying the MCNPX code, we compared the neutron energy spectrum at the lunar surface, a quantity well understood through modeling and measurements (e.g. Feldman et al., 2000; Lawrence et al., 2006; McKinney et al., 2006), from our simulations with existing results in the literature. Figure A1 shows our result for the albedo flux of neutrons over epithermal and thermal energy ranges (solid line) compared with the same quantity from McKinney et al. (2006) (dashed line). We find our results in agreement with literature values with small differences attributable to different assumptions regarding lunar surface composition and source GCR functions.

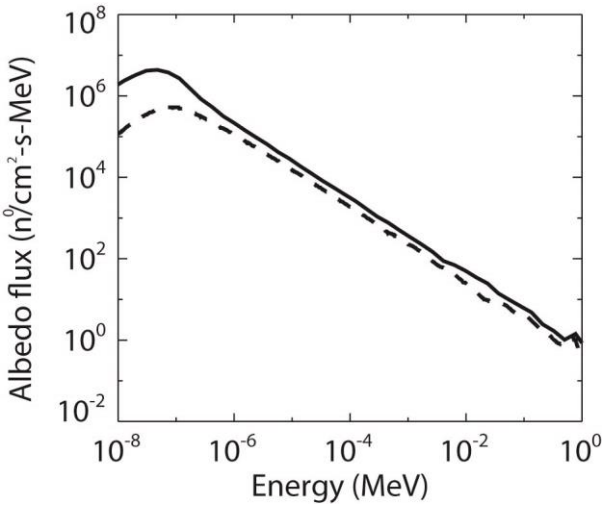

Figure B1: Thermal and epithermal neutron albedo flux from MCNPX calculations run by us (solid line), with thermal and epithermal neutron albedo flux from McKinney et al. (2006) (dashed line). Our results using the GCR input equation of McKinney et al. (2006) agree with those of McKinney with differences resulting from differing GCR source input parameters (this work: ϕ=300; McKinney et al.: ϕ=550) and lunar surface compositions (this work: FAN; McKinney et al.: more detailed Apollo 17 drill core composition).

REFERENCES

Anid, H. Al, Lewis, B.J., Bennett, L.G.I., Takada, M. (2009) Modelling of radiation exposure at high altitudes during solar storms. Radiation Protection Dosimetry, 136, 311-316, doi: 10.1093/rpd/ncp127.

Antonenko, I., Head, J.W., Mustard, J.F., Hawke, B.R. (1995) Criteria for the detection of lunar cryptomaria. Earth Moon Planets, 69, 141-172.

Arnold, J.R. (1979) Ice in the lunar polar regions. Journal of Geophysical Research 84, R10, 5659-5668.

Binder, A.B. (1998) Lunar Prospector: Overview. Science, 281, 1475-1476.

Borg. L., Connelly, J., Boyer, M., and Carlson, R. (2011) The age of lunar ferroan anorthosite 60025 with implications for the interpretation of lunar chronology and the magma ocean model. Proc. 42nd LPSC, abstract #1171.

Borg, L., Norman, M., Nyquist, L., Bogard, D., Snyder, G., Taylor, L., and Lindstrom, M. (1999) Isotopic studies of ferroan anorthosite 62236: A young lunar crustal rock from a light rare-earth-element-depleted source. Geochim. Cosmochim. Acta 63, 2679-2691.

Boynton, W.V., et al. (2004) The Mars Odyssey Gamma-Ray Spectrometer Instrument Suite. Space Science Reviews 110, 37-83.

Cahill, J.T. and Lucey, P.G. (2007) Radiative transfer modeling of lunar highland spectral classes and relationship to lunar samples. Journal of Geophysical Research, 112, E10007.

Castiglioni, G.C., Lal, D. (1980) Solar modulation effects in terrestrial production of carbon-14. Radiocarbon, 22(2), 133-158.

Carlson, R.W. and Lugmair, G.W. (1981) Sm-Nd age of lherzolite 67667: Implications for the processes involved in lunar crustal formation. Earth Planet. Sci. Lett. 52, 227-238.

Chabot N. L., et al. (2012) Areas of permanent shadow in Mercury's south polar region ascertained by MESSENGER orbital imaging. Geophysical Research Letters, 39, L09204, 10.1029/2012GL051526.

Cheek, L.C., Donaldson Hanna, K.L., Pieters, C.M., Head, J.W., and Whitten J.L. (2013) The distribution and purity of anorthosites across the Orientale basin: New perspectives from Moon Mineralogy Mapper data. Journal of Geophysical Research, 118, doi: 10.1002/jgre.20126.

Croft, S.K. (1980) Cratering flow fields: Implications for the excavation and transient expansion stage of crater formation. Proceedings of the 11th Lunar and Planetary Science Conference, p. 2347-2378.

Croft, S.K. (1981) The excavation stage of basin formation: A qualitative model. In Merrill, R.B. and Schultz, P.H., Eds., Proceedings of the Conference on Multi-Ring Basins: Formation and Evolution, pp 207-225, Pergamon, New York.

Colaprete, A., et al. (2010) Detection of water in the LCROSS ejecta plume. Science, 330, 463-468, doi:10.1126/science.1186986.

Dagge, G., Dragovitsch, P., Filges, D., Bruckner, J. (1991) Monte Carlo simulation of Martian gamma-ray spectra induced by galactic cosmic rays. Lunar Planet. Sci., 21, 425-435 (abstract).

Delitsky, M.L., Lane, A.L. (1997) Chemical schemes for surface modification of icy satellites: A road map. Journal of Geophysical Research, 102, E7, 16,385-16,390.

Delitsky, M.L., Lane, A.L. (1998) Ice chemistry on the Galilean satellites. Journal of Geophysical Research, 103, E13, 31,391-31,403.

Delistky, M.L, Thompson, W.R. (1987) Chemical processes in Triton's atmosphere and surface. Icarus, 70, 354-365.

Elphic, R. C., Lawrence, D.J., Feldman, W.C., Barraclough, B.L., Gasnault, O.M., Maurice, S., Lucey, P.G., Blewett, D.T., and Binder, A.B. (2002) Lunar Prospector neutron spectrometer constraints on TiO_2. Journal of Geophysical Research, 107, E4, 5024,8-1—8-8.

Elphic, R. C., Lawrence, D.J., Feldman, W.C., Barraclough, B.L., Maurice, S., Binder, A.B., and Lucey, P.G. (2000) Determination of lunar global rare earth element

abundances using Lunar Prospector neutron spectrometer observations. Journal of Geophysical Research, 105, E8, 20,333– 20,346.

Feldman, W.C., Barraclough, B.L., Fuller, K.R., Lawrence, D.J., Maurice, S., Miller, M.C., Prettyman, T.H., and Binder, A.B. (1999) The Lunar Prospector gamma ray and neutron spectrometers. Nuclear Instruments and Methods in Physics Research A, 422, 562-566.

Feldman, W.C., Boynton, W.V., Drake, D.M. (1993) Planetary neutron spectroscopy from orbit. In: Pieters, C.M., Englert, P., Eds., Remote Geochemical Analysis. Cambridge University Press, New York, pp. 213-234.

Feldman, W. C., Lawrence, D.J., Elphic, R.C., Vaniman, D.T., Thomsen, D.R., Barraclough, B.L., Maurice, S., and Binder, A.B. (2000) The chemical information content of lunar thermal and epithermal neutrons. Journal of Geophysical Research, 105, E8, 20,347– 20,364.

Feldman, W.C., Maurice, S., Binder, A.B., Barraclough, B.L., Elphic, R.C., Lawrence, D.J. (1998) Fluxes of fast and epithermal neutrons from Lunar Prospector: Evidence for water ice at the lunar poles. Science, 281, 1496-1500, doi: 0.1126/science.281.5382.1496.

Fischer, E.M. and Pieters, C.M. (1995) Lunar surface aluminum and iron concentration from Galilio solid state imaging data, and the mixing of mare and highland materials. Journal of Geophysical Research, 100, 23279-23290.

Gasnault, O., Feldman, W.C., Maurice, S., Genetay, I., d'Uston, C., Prettyman, T.H., and Moore, K.R., (2001) Composition from fast neutrons: application to the Moon. Geophysical Research Letters, 28, 19, 3797-3800.

Gault, D.E., Hörz, F., Brownlee, D.E., Hartung, J.B. (1974) Mixing of the lunar regolith. Geochimica et Cosmochimica Acta 3, 2365-2386.

Gerakines, P.A., Moore, M.H., Hudson, R.L. (2001) Energetic processing of laboratory ice analogs: UV photolysis versus ion bombardment. Journal of Geophysical Research, 106, E12, 33,381-33,385.

Gillis, J.J., Jolliff, B.L., and Elphic, R.C. (2003) A revised algorithm for calculating TiO2 from Clementine UVVIS data: A synthesis of rock, soil, and remotely sensed TiO2 concentrations. Journal of Geophysical Research, 108, E2, 5009, doi: 10.1029/2001JE001515.

Gladstone, G.R., et al. (2012) Far-ultraviolet reflectance properties of the Moon's permanently shadowed regions. Journal of Geophysical Research, 117, E00H04, doi: 10.1029/2011JE003913.

Goldsten, J.O., et al. (2007) The MESSENGER Gamma-Ray and Neutron Spectrometer. Space Science Reviews, 131, 339-391, doi: 10.1007/s11214-007-9262-7.

Harmon, J.K., Slade, M.A. (1992) Radar mapping of Mercury: Full-disk images and polar anomalies. Science, 258, 640-643.

Haskin, L. and Warren, P. (1991) Lunar chemistry. In G.H. Heiken, D. T. Vaniman, and B. M. French, Eds., The Lunar Sourcebook, pp 357-449, Cambridge University Press, Cambridge.

Hawke, B.R., and Bell, J.F. (1981) Remote sensing studies of lunar dark-halo impact craters: Preliminary results and implications for early volcanism. In: Proceedings of the 12th Lunar and Planetary Science Conference, pp665-678.

Hawke, B.R., Peterson, C.A., Blewett, D.T., Bussey, D.B.J., Lucey, P.G., Taylor, G.J., and Spudis, P.D. (2003) Distribution and modes of occurrence of lunar anorthosite. Journal of Geophysical Research, 108, E6, 5050, doi: 10.1029/2002JE001890.

Hayatsu, K., Hareyama, M., Kobayashi, S., Yamashita, N., Miyajima, M., Sakurai, K., Hasebe, N. (2008) Radiation doses for human exposed to galactic cosmic rays and their secondary products on the lunar surface. Biological Sciences in Space, 22, 59-66.

Head, J.W., and Wilson, L. (1992) Lunar mare volcanism – Stratigraphy, eruption conditions, and the evolution of secondary crusts. Geochimica et Cosmochimica Acta, 56, 2155-2175.

Hiesinger, H., Head, J.W. III, Wolf, U., Jaumann, R., and Neukum, G. (2011) Ages and stratigraphy of lunar mare basalts: A synthesis. Special Papers of the Geological Society of America, 477 1-51, doi: 10.1130/2011/2477(01).

Hordósy, G. (2005) Neutron and photon shielding benchmark calculations by MCNP on the LR-o experimental facility. Radiat. Prot. Dosimetry, 116, 32-34, doi: 10.1093/rpd/nci209.

Housen, K.R., Schmidt, R.S., and Hoslapple, K.A. (1983) Crater ejecta scaling laws: Fundamental forms based on dimensional analysis. Journal of Geophysical Research, 88, 2485-2499.

Hsieh, H., Jewitt, D. (2006) A population of comets in the main asteroid belt. Science, 312, 561-563, doi: 10.1126/science.1125150.

Hudson, R.L., Moore, M.H. (1995) Far-IR spectral changes accompanying proton irradiation of solids of astrochemical interest. Radiat. Phys. Chem., 45, 5, 779-789.

Hudson, R.L., Moore, M.H. (1999) Laboratory studies of the formation of methanol and other organic molecules by water + carbon monoxide radiolysis: Relevance to comets, icy satellites, and interstellar ices. Icarus, 140, 451-461.

Ingersoll, A.P., Svitek, T., Murray, B.C. (1992) Stability of polar frosts in spherical bowl-shaped craters on the Moon, Mercury, and Mars. Icarus, 100:40-47.

James, M.R., McKinney, G.W., Hendricks, J.S., Moyers, M. (2006) Enhancements in MCNPX: Heavy-ion transport and LAQGSM physics model. Nuclear Instruments and Methods in Physics Research A, 562, 819-822, doi:10.1016/j.nima.2006.02063.

James, O.B. (1980) Rocks of the early lunar crust. Proceedings of the Lunar and Planetary Science Conference 11th, pp 365-393.

James, O.B., and Flohr, M.K. (1983) Subdivision of the Mg-suite noritic rocks into Mg-gabbronorites and Mg-norites. Proceedings of the 13th Lunar and Planetary Science Conference, Part 2, in Journal of Geophysical Research, supplement, 88, A603-A614.

Johnson, R.E. (1989) Effect of irradiation on the surface of Pluto. Geophysical Research Letters, 16, 11, 1233-1236.

Jolliff, B.L. (1998) Large-scale separation of K-frac and REEP-frac in the source regions of Apollo impact-melt breccias, and a revised estimate of the KREEP composition. International Geology Review, 40, 916-935.

Jolliff, B.L., Gillis, J.J., Haskin, L.A., Korotev, R.L., and Wieczorek, M.A. (2000) Major lunar crustal terranes: Surface expressions and crust-mantle origins. Journal of Geophysical Research, 105, E5, 4197-4216.

Korotev, R.L. (2000) The great lunar hot spot and the composition and origin of the Apollo mafic ("LKFM") impact melt breccias. Journal of Geophysical Research, 105, 4317-4346.

Korotev, R.L., Jolliff, B.L., Ziegler, R.A., Gillis, J.J., and Hasken, L.A. (2003) Feldspathic lunar meteorites and their implications for compositional remote sensing of the lunar surface and the composition of the lunar crust. Geochimica et Cosmochimica Acta, 107, 24,4895-24,4923, doi:10.1016/j.gca.2003.08.001.

Korotev, R.L., Ziegler, R.A., and Jolliff, B.L. (2006) Feldspathic lunar meteorites Pecora Escarpment 02007 and Dhofar 489: Contamination of the surface of the lunar highlands by post-basin impacts. Geochimica et Cosmochimica Acta, 70, 5935-5956, doi:10.1016/j.gca.2006.09.016.

Lawrence, D.J., Feldman, W.C., Elphic, R.C., Hagerty, J.J., Maurice, S., McKinney, G.W., Prettyman, T.H. (2006) Improved modeling of Lunar Prospector neutron spectrometer data: Implications for hydrogen deposits at the lunar poles. Journal of Geophysical Research, 111, E08001, doi:10.1029/2005JE002637.

Lawrence, D.J., Feldman, W.C., Goldsten, J.O., Maurice, S., Peplowski, P.N., Anderson, B.J., Bazell, D., Mcnutt, R.L. Jr., Nittler, L.R., Prettyman, T.H., Rodgers, D.J., Solomon, S.C., Weider, S.Z. (2013) Evidence for water ice near Mercury's North Pole from MESSENGER Neutron Spectrometer measurements. Science, 339, 292-296, doi: 10.1126/science.1229953.

Lawrence, D.J., W.C. Feldman, J.O. Goldsten, T.J. McCoy, D.T. Blewett, W.V. Boynton, L.G. Evans, L.R. Nittler, E.A. Rhodes, and S.C. Solomon (2010) Identification and measurement of neutron-absorbing elements on Mercury's surface. Icarus, 209, 195-209.

Lebofsky, L.A., Feierberg, M.A., Tokunaga, A.T., Larson, H.P., Johnson, J.R. (1981) The 1.7- to 4.2-um spectrum of asteroid 1 Ceres: Evidence for structural water in clay minerals. Icarus, 48, 453-459.

Longair, M.S. (1992) High energy astrophysics. 2nd Ed. Cambridge University Press, Cambridge, 399 pp.

Lucey, P.G., (2000) Potential for pre-biotic chemistry at the poles of the Moon. Proceedings of SPIE 4137, 84-88.

Lucey, P.G. (2004) Mineral maps of the moon. Geophysical Research Letters, 31, L08701, doi:10.1029/2003GL019406.

Lucey, P.G., Blewett, D.T., and Jolliff, B.L. (2000a) Lunar iron and titanium abundance algorithms based on final processing Clementing UVVIS images. Journal of Geophysical Research, 105, E8, 20297-20305.

Lucey, P.G., Blewett, D.T., Taylor, G.J., and Hawke, B.R. (2000b) Imaging of lunar surface maturity. Journal of Geophysical Research, 105, E8, 20,377-20,386.

Lucey, P.G., Taylor, G.J., Hawke, B.R., and Spudis, P.D. (1998) FeO and TiO2 concentrations in the South Pole-Aitken basin: Implications for mantle composition and basin formation. Journal of Geophysical Research, 103, 3701-3708.

Lucey, P.G. et al. (2006) Understanding the lunar surface and space-Moon interactions. In Jolliff, B.L., Wieczorek, M.A., Shearer, C.K., and Neal, C.R, Eds., New Views of the Moon, pp 83-219, Mineralogical Society of America.

Masarik, J., Reedy, R.C. (1996) Gamma ray production and transport in Mars. Journal of Geophysical Research 101, 18,891-18,912.

McCord, T.B., et al. (1981) Moon: Near-infrared spectral reflectance, a first good look. Journal of Geophysical Research, 86,10,883-10,892.

McCracken, K.G., Beer, J. (2007) Long-term changes in the cosmic ray intensity at Earth. Journal of Geophysical Research 112, A10101, doi: 10.1029/2006JA012117.

McKinney, G.W., Lawrence, D.J., Prettyman, T.H., Elphic, R.C., Feldman, W.C., Hagerty, J.J. (2006) MCNPX benchmark for cosmic ray interactions with the Moon. Journal of Geophysical Research 111, E06004, doi:10.1029/2006JE002551.

Mitchell, J.K., Carrier, W.D. III, Houston, W.N., Scott, R.F., Bromwell, L.G., Durgunoglu, H.T., Hovland, H.J., Treadwell, D.D., Costes, N.C. (1972) Soil-mechanics experiments. In Apollo 15 Preliminary Science Report, pp. 8-1 to 8-29. NASA SP-315.

Mitrofanov, I.G., et al. (2010) Lunar Exploration Neutron Detector for the NASA Lunar Reconnaissance Orbiter. Space Science Review, 150, 183-207, doi: 10.1007/s11214-009-9608-4.

Mitrofanov, I.G., et al. (2010) Hydrogen mapping of the lunar south pole using the LRO Neutron Detector Experiment LEND. Science, 330, 483-486, doi:10.1126/science.1185696.

Moore, M.H., Donn, B., Khanna, R., A'Hearn, M.F. (1983) Studies of proton-irradiated cometary-type ice mixtures. Icarus, 54, 388-405.

Moore, M.H., Hudson, R.L. (1998) Infrared study of ion-irradiated water-ice mixtures with hydrocarbons relevant to comets. Icarus, 135, 518-527.

Moore, M.H., Hudson, R.L. (2003) Infrared study of ion-irradiated N_2-dominated ices relevant to Triton and Pluto: formation of HCN and HNC. Icarus, 161, 486.500.

Moore, M.H., Hudson, R.L., Gerakines, P.A. (2001) Mid- and far-infrared spectroscopic studies of the influence of temperature, ultraviolet photolysis and ion irradiation on cosmic-type ices. Spectrochimica Acta Part A, 57, 843-858.

Morgan, T.H., Shemansky, D.E. (1991) Limits to the lunar atmosphere. Journal of Geophysical Research, 96, 1351-1367.

National Nuclear Data Center (2010) Evaluated Nuclear Data File (ENDF) Retrieval & Plotting < http://www.nndc.bnl.gov/sigma/>.

Neal, C.R. and Taylor, L.A. (1992) Petrogenesis of mare basalts: A record of lunar volcanism. Geochimica et Cosmochimica Acta, 56, 2177-2211.

Neumann, G.A., Cavanaugh, J.F., Sun, X., Mazarico, E.M., Smith, D.E., Zuber, M.T., Mao, D., Paige, D.A., Solomon, S.C., Ernst, C.M., Barnouin, O.S. (2013) Bright and dark polar deposits on Mercury: Evidence for surface volatiles. Science, 339, 296-300, doi: 10.1126/science.1229764.

Neumann, G. A., M. T. Zuber, D. E. Smith, and F. G. Lemoine (1996) The lunar crust: Global structure and signature of major basins. Journal of Geophysical Research 101, 16,841–16,843.

Newhauser, W., Koch, N., Hummel, S., Ziegler, M., Titt, U. (2005) Monte Carlo simulations of a nozzle for the treatment of ocular tumours with high-energy proton beams. Phys. Med. Biol. 50, 5229-5249, doi: 10.1088/0031-9155/50/22/002.

Nozette, S., et al. (1994) The Clementine Mission to the Moon: Scientific Overview. Science, 266.5192, 1835-1839.

Nozette, S., Lichtenberg, C.L., Spudis, P., Bonner, R., Ort, W., Malaret, E., Robinson, M., Shoemaker, E.M. (1996) The Clementine bistatic radar experiment. Science, 274, 1495-1498, doi: 10.1126/science.274.5292.1495.

Ogawa, Y., et al. (2011) The widespread occurrence of high-calcium pyroxene in bright-ray craters on the Moon and implications for lunar-crust composition. Geophysical Research Letters, 38, L17202, doi: 10.1029/2011GL048569.

Ohtake, M. et al. (2009) The global distribution of pure anorthosite on the Moon. Nature, 461, 236-240.

Ohtake, M., et al. (2012) Primitive farside highland materials detected by Mg number. 43rd Lunar and Planetary Science Conference, Houston, TX, abstract # 1977.

O'Keefe, J.D. and Ahrens, T.J. (1993) Planetary cratering mechanics. Journal of Geophysical Research, 98, 17,011-17,028.

Paige, D.A., et al. (2010) Diviner Lunar Radiometer observations of cold traps in the Moon's South Polar region. Science, 330, 479-482, doi: 10.1126/science.1187726.

Paige, D.A., Siegler, M.A., Harmon, J.K., Neumann, G.A., Mazarico, E.M., Zuber, M.T., Harju, E., Delitsky, M.L., Solomon, S.C. (2013) Thermal stability of volatiles in the North Polar region of Mercury. Science, 339, 300-303, doi: 10.1126/science.1231106.

Papike, J.J., Ryder, G., and Shearer, C.K. (1998) Lunar Samples. In Papike, J.J. Ed., Planetary Materials, Reviews in Mineralogy 36, pp 5-1-5-234, Mineralogical Society of America.

Pelowitz, D.B. (Ed.) (2008) MCNPX user's manual version 2.6.0. Rep. LA-CP-07-1473, Los Alamos Natl. Lab, Los Alamos, N.M.

Petro, N.E. and Pieters, C.M. (2004) Surviving the heavy bombardment: Ancient material at the surface of South Pole-Aitken Basin. Journal of Geophysical Research, 109, E06004, doi: 10.1029/2003JE002182.

Petro, N.E. and Pieters, C.M. (2008) The lunar-wide effects of basin ejecta distribution on the early megaregolith. Meteoritics and Planetary Science, 43, 1517-1529.

Pieters, C.M. (1978) Mare basalt types on the front side of the Moon. Proceedings of the 9th Lunar and Planetary Science Conference, p. 2825-2849.

Pieters, C.M. (1986) Composition of the lunar highland crust from near-infrared spectroscopy. Reviews of Geophysics, 24, 557-578.

Pieters, C.M., Head, J.W., Adams, J.B., McCord, T.B., Zisk, S.H., and Whitford-Stark, J.L. (1980) Late high-titanium basalts of the western maria: Geology of the Flamsteed

region of Oceanus Procellarum. Journal of Geophysical Research, 85, 3913-3938, doi: 10.1029/JB085iB07p03913.

Pieters, C.M. et al., (2009a) Mineralogy of the lunar crust in spatial context: first results from the Moon Mineralogy Mapper (M^3). 40th Lunar and Planetary Science Conference, Houston, TX, Abstract #2052.

Pieters, C.M., et al., (2009b) Character and spatial distribution of OH/H_2O on the surface of the Moon seen by M^3 on Chandrayaan-1. Science, 326, 568-572, doi:10.1126/science.1178658.

Pike, R.J. (1974) Ejecta from large craters on the Moon: Comments on the geometric model of McGetchin et al. Earth and Planetary Science, 23, 265-274.

Prettyman, T.H., et al. (2003) Gamma-ray and neutron spectrometer for the Dawn mission to 1 Ceres and 4 Vesta. IEEE Transactions on Nuclear Science 50, 1190-1197, doi: 10.1109/TNC.2003.815156.

Prettyman, T.H., Hagerty, J.J., Elphic, R.C., Feldman, W.C., Lawrence, D.J., McKinney, G.W., and Vaniman, D.T. (2006) Elemental composition of the lunar surface: Analysis of gamma ray spectroscopy data from Lunar Prospector. Journal of Geophysical Research, 111, E12007, doi:10.1029/2005JR002656.

Ryder,G. (1991) Lunar ferroan anorthosites and mare basalt sources: The mixed connection. Geophysical Research Letters, 18, 11, 2065-2068.

Ryder, G. and Spudis, P. (1980) Volcanic rocks in the lunar highlands. In Papike, J.J. and Merrill, R.B., Eds., Proceedings of the Conference on the Lunar Highlands Crust, p. 353-375, Pergamon Press.

Ryder, G. and Wood, J.A. (1977) Serenitatis and Imbrium impact melts: Implications for large-scale layering in the lunar crust. Proceedings of the Lunar Science Conference 8th, 655-668.

Salvail, J.R., Fanale F.P. (1994) Near-surface ice on Mercury and the Moon: A topographic thermal model. Icarus, 111, 441-455.

Schultz, P.H., Hermalyn, B., Colaprete, A., Ennico, K., Shirley, M., Marshall, W.S. (2010) The LCROSS Cratering Experiment. Science, 330, 468-472, doi: 10.1126/science.1187454.

Schultz, P.H., and Spudis, P.D. (1983) Beginning and end of lunar mare volcanism. Nature, 302, 233-236.

Schwadron, N.A., et al., (2012) Lunar radiation environment and space weathering from the Cosmic Ray Telescope for the Effects of Radiation (CRaTER). Journal of Geophysical Research, 117, E00H13, doi: 10.1029/2011JE003978.

Shikaze, Y., et al., (2007) Measurements of 0.2-20GeV/n cosmic-ray proton and helium spectra from 1997 through 2002 with the BESS spectrometer. Astroparticle Physics, 28, 154-167, doi: 10.1016/j.astropartphys.2007.05.001.

Simpson, J.A. (1983) Elemental and isotopic composition of the galactic cosmic rays. Annu. Rev. Nucl. Particle Sci. 33, 323-381.

Smith, J.V., Anderson, A.T., Newton, R.C., Olsen, E.J., Wyllie, P.J., Crewe, A.V., Isaacson, M.S., and Johnson, D. (1970) Petrologic history of the Moon inferred from petrography, mineralogy, and petrogenesis of Apollo 11 rocks. Proceedings of the Apollo 11 Lunar Science Conference, Pergamon Press, p. 897-925.

Snyder, G.A., Taylor, L.A., and Neal, C.R. (1992) A chemical model for generating the sources of mare basalts: Combined equilibrium and fractional crystallization of the lunar magmasphere. Geochimica et Cosmochimica Acta, 56, 3809-3823, doi: 10.1016/0016-7037(92)90172-F.

Spence, H.E., et al. (2010) CRaTER: The Cosmic Ray Telescope for the Effects of Radiation experiment on the Lunar Reconnaissance Orbiter mission. Space Science Rev. 150, 243-284, doi: 10.1007/s11214-009-9584-8.

Spudis, P.D. (1993) The Geology of Multiringed Basins. 263p, Cambridge University Press, New York.

Spudis, P.D., et al. (2010) Initial results for the north pole of the Moon from Mini-SAR, Chandrayaan-1 mission. Geophysical Research Letters, 37, L06204, doi: 10.1029/2009GL042259.

Staid, M.I. and Pieters, C.M. (2001) The mineralogy of last lunar basalts: Results from Clementine. Journal of Geophysical Research, 106, 27877-27900, doi: 10.1029/2000JE001387.

Staid, M.I., et al. (2011) The mineralogy of late stage lunar volcanism as observed by the Moon Mineralogy Mapper on Chandrayaan-1. Journal of Geophysical Research, 116, E00G10, doi: 10.1029/2010JE003735.

Stöffler, D., Knoll, H.-D., Marvin, U.B., Simonds, C.H., and Warren, P.H. (1980) Recommended classification and nomenclature of lunar highland rock—A committee report. In J.J. Papike and R.B. Merrill, Eds., Proceedings of the Conference on the Lunar Highland Crust, p 51-70, Pergamon Press.

Taylor, S.R., and McLennan, S. (2009) Planetary Crusts: Their Composition, Origin, and Evolution. Cambridge University Press, Cambridge, 378 pp.

Taylor, G.J., Warren, P. Ryder, G., Delano, J., Pieters, C., and Lofgren, G. (1991) Lunar Rocks. In G.H. Heiken, D. T. Vaniman, and B. M. French, Eds., The Lunar Sourcebook, pp 183-261, Cambridge University Press, Cambridge.

Terada, K., Anand, M., Sokol, A.K., Bischoff, A., Sano, Y. (2007) Cryptomare magmatism 4.35 Gyr ago recorded in lunar meteorite Kalahari 009. Nature, 450, 849-852.

Thomas, G.E. (1974) Mercury: Does its atmosphere contain water? Science, 183, 1197-1198.

Tompkins, S. and Pieters, C.M. (1999) Mineralogy of the lunar crust: Results from Clementine. Meteoritics and Planetary Science, 34, 25-41.

Urey, H.C. (1952) The Planets: Their Origin and Development. Yale University Press, New Haven, CT, 245 pp.

Vasavada, A.R., Paige, D.A., Wood, S.E. (1999) Near-surface temperatures on Mercury and the Moon and the stability of polar ices deposits. Icarus, 141, 179-193.

Warren, P.H. (1985) The magma ocean concept and lunar evolution. Annual Review of Earth and Planetary Sciences, 13, 201-240.

Warren, P.H. (1990) Lunar anorthosites and the magma-ocean plagioclase-flotation hypothesis: Importance of FeO enrichment in the parent magma. American Mineralogist, 75, 46-58.

Warren, P.H. and Wasson, J.T. (1977) Pristine nonmare rocks and the nature of the lunar crust. Proceedings of the 8th Lunar Science Conference, p. 2215-2235.

Watson, K., Murray, B.C., Brown, H. (1961) The behavior of volatiles on the lunar surface. Journal of Geophysical Research, 66, 9, 3033-3045.

Wieczorek, M.A. and Phillips, R.J. (1999) Lunar multiring basins and the cratering process. Icarus, 139, 246-259.

Wieczorek et al. (2006) The Constitution and Structure of the Lunar Interior. In Jolliff, B.L., Wieczorek, M.A., Shearer, C.K., and Neal, C.R., Eds., New Views of the Moon, pp221-364, Mineralogical Society of America.

Wieczorek, M.A. et al. (2013) The crust of the Moon as seen by GRAIL. Science, 339, 671-675, doi: 10.1126/science.1231530.

Wilhelms D. E. (1987) The geologic history of the Moon, 1st ed. Washington, D.C., United States Geological Survey. 327 p.

Wood, J.A., Dickey, J.S.J., Marvin, U.B., and Powell, B.N. (1970) Lunar anorthosites and a geophysical model of the moon. Proceedings of the Apollo 11 Lunar Science Conference, pp. 965–988.

Yamamoto, S., Nakamura, R., Ogawa, Y., Ishihara, Y., Morota, T., Hirata, N., Ohtake, M., Hiroi, T., Yokota, Y., and Haruyama, J. (2012) Massive layer of pure anorthosites on the Moon. Geophysical Research Letters, 39, L13201, doi: 10.1029/2012GL052098.

Zhang, J.A., Paige. D.A. (2009) Cold-trapped organic compounds at the poles of the Moon and Mercury: Implications for origins. Geophysical Research Letters, 36, L16203, doi: 10.1029/2009GL038614.

Ziegler, J.F., Biersack, J.P., Littmark, U. (2003) The Stopping and Range of Ions in Solids. Pergamon Press, New York.

Zuber, M.T., Head, J.W., Smith, D.E., Neumann, G.A., Mazarico, E., Torrence, M.H., Aharonson, O., Tye, A.R., Fassett, C.I., Rosenberg, M.A., Melosh, H.J. (2011) Constraints on the volatile distribution within Shackleton crater at the lunar south pole. Nature, 486, 378-382, doi: 10.1038/nature11216.